TECHNISCHE MECHANIK

since 1980

Editor:
Magdeburger Verein für Technische Mechanik e.V.
und Otto-von-Guericke-Universität Magdeburg

Volume 39 Issue 3 (2019)

ISSN 0232-3869 (print)
ISSN 2199-9244 (online)

TECHNISCHE MECHANIK

Wissenschaftliche Zeitschrift für Grundlagen und Anwendungen der Technischen Mechanik
Scientific Journal for Fundamentals and Applications of Engineering Mechanics

The journal **Technische Mechanik** publishes refereed original articles on Engineering Mechanics in its broadest sense. It is intended to provide a forum for a rapid transfer of research results to industry and science. In that sense contributions are encouraged which demonstrate the practical application of new results and scientific findings.

In der **Technischen Mechanik** werden begutachtete Beiträge aus allen Gebieten der Mechanik publiziert. Ein Hauptanliegen besteht in der raschen Verfügbarmachung von Forschungsergebnissen für Industrie und Wissenschaft. In diesem Sinne werden vor allem auch solche Beiträge bevorzugt, die neben neuen Ergebnissen und Erkenntnissen auch deren praktische Anwendung beinhalten.

Redaktion/Editorial Office
W. Lenz (Chefredakteur)

Bezugsmöglichkeiten

Die Zeitschrift Technische Mechanik erscheint ab dem Jahr 2019 ausschließlich in elektronischer Form. Die Zeitschrift Technische Mechanik ist ein Open Access Journal. Alle Artikel können kostenfrei von unserer Webseite herunter geladen werden.
Für Veröffentlichungen fallen für die Autoren keine Kosten an. Alle Artikel werden einem standardmäßigen Begutachtungsprozess unterzogen.

The journal Technische Mechanik is distributed only electronically with the beginning of 2019. The journal Technische Mechanik is an Open Access journal. All papers are available free of charge for download. Publishing of papers is free of any costs for the authors. Each submitted paper runs through a standard peer review process.

Anschrift der Redaktion/Editorial Office
Redaktion Technische Mechanik
Institut für Mechanik
Otto-von-Guericke-Universität
Postfach 4120
D-39016 Magdeburg
Telefon: +49 391 67–52 459
Telefax: +49 391 67–12 439/–12 863
e-mail: Technische.Mechanik@ovgu.de
http://www.ovgu.de/techmech/

Herausgeber/Publisher
Magdeburger Verein für Technische Mechanik e.V.
und Otto-von-Guericke-Universität Magdeburg
Geschäftsführender Herausgeber: D. Juhre
Stellvertr. geschäftsführender Herausgeber: E. Woschke

Inhalt / Contents

ISSN 0232-3869 (print)
ISSN 2199-9244 (online)

TECHNISCHE MECHANIK
an open access journal

journal homepage: www.ovgu.de/techmech

Tech. Mech., Vol. 39, Is. 3, (2019), 241–251

Received: 07.02.2019
Accepted: 11.06.2019
Available online: 01.10.2019

Mathematical modeling and analysis of elastic waves in a thermo piezoelectric multilayered rotating composite rod with LEMV/CFRP interface

R.Selvamani[1]* S.Mahesh[2]

[1] Karunya University,Department of Mathematics,Coimbatore ,TamilNadu, India.
[2] Kathir College of Engineering,Department of Mathematics,Coimbatore ,TamilNadu, India.

Abstract: In this present paper, we form the mathematical model for wave propagation in a thermo piezoelectric multilayered rotating composite rod made of inner and outer piezoelectric layer bonded together by Linear Elastic Materials with voids (LEMV).To uncouple the equation of motion, electric and heat conduction equations, displacement potential functions are introduced. The frequency equations are obtained for longitudinal and flexural modes of vibration and are studied numerically for heat conducting PZT-5A material.The computed non-dimensional frequency is presented in the form of dispersion curves against various physical quantities. Adhesive layer Linear Elastic Materials with Voids (LEMV) is compared with Carbon Fibre Reinforced Polymer (CFRP).We found that the frequency wave characteristics are more stable and realistic in the presence of thermal, electrical and the rotation parameters

Keywords: Piezoelectric cylinder, Thermal cylinders, Rotating rod, Vibration, Stress analysis, LEMV, CFRP, multilayered structures, Composite cylinder.

1 Introduction

Solid state materials in engineering is hovering to provide significant inputs to the areas of constructive design of structural components as well as creating trends of its own. The cross disciplinary fields of mechanical materials and interfacial component are shows potential developments. Further interdisciplinary materials research will likely to continue to acquiesce materials with improved properties for application that is both common place and specialized. piezoelectric polymers allow their use in a massive amount of compositions and geometrical shapes for a huge variety of applications from transducers in acoustics, ultrasonics and hydrophone applications to resonators in band pass filters, power supplies, delay lines, medical scans and some industrial non-destructive testing instruments.The frequency responses of rotating cylindrical structures has numerous applications in a variety of fields of science and technology, specifically, submarine structures, pressure vessel, bore wells, ship building industries and have many other engineering applications.

Honarvar et al. (2007) developed a wave propagation model for a transversely isotropic cylinders and verified their physical characteristics. Thermo-piezoelectric materials are intelligent materials that display individual electro-mechanical coupling.In view of this, Paul and Raman (1991) studied wave propagation in a hollow pyroelectric circular cylinder of crystal class 6.Mindlin (1974)analyzed equations of high frequency vibrations of thermopiezoelectric crystal plates.Also Paul and Raman (1993) discussed wave propagation in a pyroelectric cylinder of arbitrary cross section with a circular cylindrical cavity.Storozhev (2013),investigated propagation of electro elastic waves in multilayer piezoelectric cylinders with a sector notch.Nelson and Karthikeyan (2008a) discussed axisymmetric vibration of pyrocomposite solid cylinder.Nelson and Karthikeyan (2008b)studied axisymmetric vibration of pyrocomposite hollow cylinder.Shulga (2002) observed Propagation of harmonic waves in anisotropic piezoelectric cylinders:Compound waveguides.Hua et al. (2013) observed guided wave propagation and focusing in multi-layer pipe with viscoelastic coating and infinite soil media.Tasdemirci et al. (2004) discussed Stress wave propagation effects in two-and three-layered composite materials.Singh and Saxena (1995) discussed axisymmetric vibration of a circular plate with double linear variable thickness.Presented clear statement for modal shapes and natural frequencies of materials into account the effects of length, shear deformation, and rotary inertia.Abd-Alla and Mahmoud (2010) observed magneto-thermoelastic problem in rotating non homogeneous orthotropic hollow cylindrical under the hyperbolic heat conduction model.El-Naggar et al. (2002) discussed thermal stresses in a rotating non-homogeneous orthotropic hollow cylinder.Abd-Alla et al. (2000) examined thermal stresses in a non-homogeneous orthotropic elastic multilayered cylinder.Abd-All et al. (1999) observed transient thermal stresses in a rotating non-homogeneous cylindrically orthotropic composite tubes. Selvamani (2015) has discussed wave propagation in a rotating disc of polygonal cross-section immersed in an inviscid fluid.Several researches are performedto incorporate the interfacial material in analysis of composite multilayered mechanical structure.Among that, the study of Cowin and Nunziato (1983) with Linear Elastic Materials with Voids as interface bonding materialis noted. However, the rotational effect on the thermo-electro-mechanical vibration responses of multiylarerd cylinder with different bonding material(LEMV/CFRP) not been reported thus far. Therefore, the objective of the present work is to investigate the influence of the thermos piezo elasticity and rotation on the vibrating of

* E-mail address: selvam1729@gmail.com
doi: 10.24352/UB.OVGU-2019-022

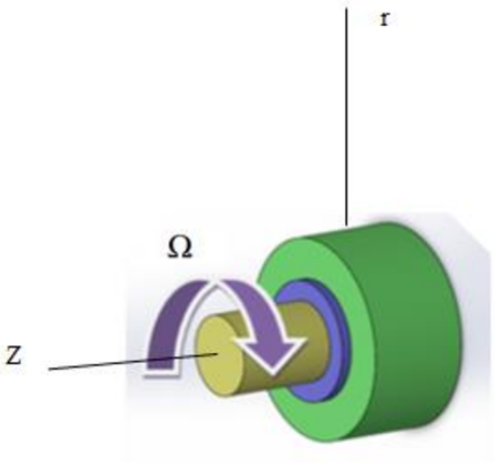

Fig. 1: Geometry which shows the problem

piezoelectric multilayered cylinder with different bonding material.
The present article intended to revise mathematical model for wave propagation in a thermo piezoelectric multilayered rotating composite rod made of inner and outer piezoelectric layer bonded together by linear Elastic materials with voids (LEMV).To uncouple the equation of motion, electric and heat conduction equations, displacement potential functions are introduced. The frequency equations are obtained for longitudinal and flexural modes of vibration and are studied numerically for heat conducting PZT-5A material.The computed non-dimensional frequency is presented in the form of dispersion curves against various physical quantities. Adhesive layer LEMV is compared with Carbon Fibre Reinforced Polymer (CFRP).

2 Formulation of problem

In this section we consider a homogeneous transversely isotropic, thermally and electrically conducting piezoelectric rotating composite rod of infinite length with uniform temperature T_0 in the undistributed state initially. The composite rod is assumed to be rotating with consistent angular velocity $\bar{\Omega}$. In cylindrical coordinates (r, z), the equations of motion in axisymmetric direction and absence of body force and including the Coriolis Effect and centripetal forces are

$$\sigma^l_{rr,r} + \sigma^l_{rz,z} + r^{-1}\sigma^l_{,rr} + \rho(\bar{\Omega} \times (\bar{\Omega} \times \bar{u}) + 2(\bar{\Omega} \times \bar{u}_{,t})) = \rho u_{,tt} \tag{1a}$$

$$\sigma^l_{rz,r} + \sigma^l_{zz,z} + r^{-1}\sigma^l_{,rz} + \rho(\bar{\Omega} \times (\bar{\Omega} \times \bar{u}) + 2(\bar{\Omega} \times \bar{u}_{,t})) = \rho w_{,tt} \tag{1b}$$

The electric displacement equation is given as

$$\frac{1}{r}\frac{\partial}{\partial r}(rD^l_r) + \frac{\partial}{\partial z}(D^l_z) = 0 \tag{1c}$$

The heat conduction equation is defined as

$$K_{11}(T^l_{,rr} + r^{-1}T^l_{,r} + r^{-2}T^l_{,\theta\theta}) + K_{33}T^l_{,zz} - \rho^l c_v T_{,t} = T_0\frac{\partial}{\partial t}[\beta_1(e^l_{,rr} + e^l_{,\theta\theta}) + \beta_3 e^1_{,zz} - p_3\phi_{,z}] \tag{1d}$$

Relation between the stress and strain of mechanical and electrical field is

$$\sigma^l_{rr} = c_{11}e^l_{rr} + c_{12}e^l_{\theta\theta} + c_{13}e^l_{zz} - \beta_1 T^l - e_{31}E^l_z \tag{2a}$$

$$\sigma^l_{zz} = c_{13}e^l_{rr} + c_{13}e^l_{\theta\theta} + c_{33}e^l_{zz} - \beta_3 T^l - e_{33}E^l_z \tag{2b}$$

$$\sigma^l_{rz} = c_{44}e^l rz \tag{2c}$$

$$D_r = e_{15}e^l_{rz} + \varepsilon_{11}E^l_r \tag{2d}$$

$$D_z = e_{31}(e^l_{rr} + e^l_{\theta\theta}) + e_{33}e^l_{zz} + \varepsilon_{33}E^l_z + p_3 T \tag{2e}$$

where $\sigma^l_{rr}, \sigma^l_{r\theta}, \sigma^l_{rz}, \sigma^l_{\theta\theta}, \sigma^l_{zz}, \sigma^l_{z\theta}$ denotes mechanical stress component, $e^l_{\theta\theta}, e^l_{r\theta}, e^l_{z\theta}, e^l_{rz}$ are the strain components, T^l is the temperature change about the equilibrium temperature,$c_{11}, c_{12}, c_{13}, c_{33}, c_{44}, c_{66}$ are the five elastic constants,β_1, β_3 and K_1, K_3 respectively thermal expansion coefficients and thermal conductivities along and perpendicular to the symmetry, ρ is the mass density, c_v is the specific heat capacity,p_3 is the pyroelectric effect.

The strains e_{ij} are related to the displacements given by

$$e^l_{rr} = u^l_{,r} e^l_{\theta\theta} = r^{-1}(u^l + v^l_{,\theta}), e^l_{zz} = w^l_{,rz} \tag{3a}$$

$$e^l_{r\theta} = v^l_r - r^{-1}(v^l - u^l_{,\theta}), \tag{3b}$$

$$e^l_{z\theta} = v^l_{,z} + r^{-1} w^l_{,r\theta} e^l_{rz} = w^l_{,r} + u^l_{,z} \tag{3c}$$

Substitution of the (3) and (2) into (1) results in the following three dimensional equation of motion and heat conduction:

$$c_{11}(u^l_{,rr} + r^{-1}u^l_{,r} - r^{-2}u) + c_{44}u^l_{,zz} + (c_{44} + c_{13})w^l_{rz} + (e_{31} + e_{15})E^l_{rz} - \beta_1 T_{,r} + \rho(\Omega^2 u^l + 2\Omega u_{,t}) = \rho u^l_{,tt} \tag{4a}$$

$$c_{44}(w^l_{rr} + r^{-1}w^l_{,r}) + r^{-1}(c_{44} + c_{13})u^l_{,z} + (c_{44} + c_{13})u^l_{,rz} + c_{33}w^l_{,zz} + e_{33}E_{,zz}(E_{,rr} + r^{-1}E_{,r})$$
$$-\beta_3 T_{,z} + \rho(\Omega^2 w^l + 2\Omega u_{,t}) = \rho w^l_{,tt} \tag{4b}$$

$$e_{15}(w^l_{rr} + r^{-1}w^l_{,r}) + e_{31} + e_{15}(u^l_{,rz} + r^{-1}u^l_{,z}) + e_{33}w^l_{,zz} - \eta_{33}E^l_{,zz} - \eta_{11}(E^l_{,rr} + r^{-1}E^l_{,r}) + p_3 T^l_{,z} = 0 \tag{4c}$$

$$K_{11}(T^l_{,rr} + r^{-1}T^l_{,r} + r^{-2}T^l_{,\theta\theta}) + K_{33}T^l_{,zz} - \rho^l c_v T_{,t} = T_0 \frac{\partial}{\partial t}[\beta_1(u^l_{,r} + r^{-1}v^l_{,\theta} + r^{-1}u^l) + \beta_3 w^l_{,z}] - p_3 E^l_{,z} \tag{4d}$$

Solution of the field Equation

$$u^l(r,z,t) = (\phi^l_{,r}) \exp i(kz + \omega t) \tag{5a}$$

$$w^l(r,z,t) = \frac{i}{a} W^l \exp i(kz + \omega t) \tag{5b}$$

$$E^l(r,z,t) = \frac{ic_{44}}{ae_{33}} V^l \exp i(kz + \omega t) \tag{5c}$$

$$T^l(r,z,t) = \frac{c_{44}}{\beta_3 a^2} T^l \exp i(kz + \omega t) \tag{5d}$$

Here $i = \sqrt{-1}$, k is the wave number,ω is the frequency,$u^l, w^l E^l, T^l$ are all displacement potentials, electric conduction and thermal change. By introducing the dimensionless quantities such as $x = \frac{r}{a}$,$\eta = ka$, $\Omega^2 = \frac{\rho\omega^2 a^2}{c_{44}}$,$\bar{c}_{11} = \frac{c_{11}}{c_{44}}$,
$\bar{c}_{13} = \frac{c_{13}}{c_{44}}$,$\bar{c}_{33} = \frac{c_{33}}{c_{44}}$,$\bar{c}_{66} = \frac{c_{66}}{c_{44}}$,$\bar{\beta} = \frac{\beta_1}{\beta_3}$,$\bar{k}_i = \frac{(\rho c_{44})^{\frac{1}{2}}}{\beta_3^2 T_0 a\Omega}$,$\bar{d} = \frac{\rho c_v c_{44}}{\beta_3^2 T_0}$,$\bar{p}_3 = \frac{p_3 c_{44}}{\beta_3 e_{33}}$
Substituting (5) in (4) we obtain

$$(\bar{c}_{11}\nabla^2 + (\Omega^2 - \zeta^2))\phi^l - \zeta(1 + \bar{c}_{13})W^l - \zeta(\bar{e}_{31} + \bar{e}_{15})E^l - \bar{\beta}T^l = 0 \tag{6a}$$

$$\zeta(1 + \bar{c}_{13})\nabla^2\phi^l + (\nabla^2 + (\Omega^2 - \zeta^2\bar{c}_{33}))W^l + (\bar{e}_{33}\nabla^2 - \zeta^2)E^l - \zeta T^l = 0 \tag{6b}$$

$$\zeta(\bar{e}_{31} + \bar{e}_{15})\nabla^2\phi^l + (\bar{e}_{15}\nabla^2 - \zeta^2)W^l + (\zeta^2\bar{e}_{33} - \bar{\epsilon}\nabla^2)E^l + \zeta\bar{p}_3 T^l = 0 \tag{6c}$$

$$\bar{\beta}\nabla^2\phi^l - \zeta W^l + \zeta\bar{p}_3 E^l + (\bar{d} + i\bar{k}_1\nabla^2 + i\bar{k}_3\zeta^2)T^l = 0 \tag{6d}$$

where $\nabla^2 = \frac{\partial^2}{\partial x^2} + x^{-1}\frac{\partial}{\partial x}$

$$\begin{vmatrix} [\bar{c}_{11}\nabla^2 + (\Omega^2 - \zeta^2)] & -\zeta(1 + \bar{c}_{13}) & \zeta(\bar{e}_{31} + \bar{e}_{15}) & -\bar{\beta} \\ \zeta(1 + \bar{c}_{13})\nabla^2 & [\nabla^2 + (\Omega^2 - \bar{c}_{33}\zeta^2)] & (\bar{e}_{33}\nabla^2 - \zeta^2) & -\zeta \\ \zeta(\bar{e}_{31} + \bar{e}_{15})\nabla^2 & \bar{e}_{15}\nabla^2 - \zeta^2 & (\zeta^2\bar{\epsilon}_{33} - \bar{\epsilon}\nabla^2) & \zeta\bar{p}_3 \\ \bar{\beta}\nabla^2 & -\zeta & \zeta\bar{p}_3 & (\bar{d} + i\bar{k}_1\nabla^2 - i\bar{k}_3\zeta^2) \end{vmatrix} (\phi^l_n, W^l_n, E^l, T^l_n)^T = 0 \tag{7}$$

Evaluating the given in (7), we obtain a partial differential equation of the form

$$(p^l\nabla^8 + q^l\nabla^6 + r^l\nabla^4 + s^l\nabla^2 + t^l)(\phi^l, W^l, E^l, T^l)^T = 0 \tag{8}$$

Factorizing the relation given in (8) into biquadrate equation for $(\alpha_j^2 a)^2, j = 1,2,3,4$ the solutions for the symmetric modes are obtained as

$$\phi^l = \sum_{j=1}^{4}[A^l_j J_n(\alpha^l_j ax)]cosn\theta \tag{9a}$$

$$W^l = \sum_{j=1}^{4}[a^l_j A^l_j J_n(\alpha^l_j ax)]cosn\theta \tag{9b}$$

$$E^l = \sum_{j=1}^{4}[b^l_j A^l_j J_n(\alpha^l_j ax)]cosn\theta \tag{9c}$$

$$T^l = \sum_{j=1}^{4}[c^l_j A^l_j J_n(\alpha^l_j ax)]cosn\theta \tag{9d}$$

Here $(\alpha_j^l ax) > 0,\ for(j = 1, 2, 3, 4)$ are the roots of algebraic equation

$$(p^l(\alpha_j^l ax)^8 + q^l(\alpha_j^l ax)^6 + r^l(\alpha_j^l ax)^4 + s^l(\alpha_j^l ax)^2 + t^l)(\phi^l, W^l, E^l, T^l)^T = 0$$

Here a_j^l, b_j^l, c_j^l are the arbitrary constants and $J_n(\alpha_l^j ax)$ denotes the Bessel functions first kind of order n. The constants a_j^l, b_j^l, c_j^l are calculated using the following relations with $\nabla^2 = \alpha_j^l ax$

$$\begin{aligned}
(\bar{c}_{11}\nabla^2 + (\Omega^2 - \zeta^2)) - \zeta(1 + \bar{c}_{13})a_j^l - \zeta(\bar{e}_{31} + \bar{e}_{15})b_j^l - \bar{\beta}c_j^l = 0\\
\zeta(1 + \bar{c}_{13})\nabla^2 + (\nabla^2 + (\Omega^2 - \zeta^2\bar{c}_{33}))a_j^l + (\bar{e}_{33}\nabla^2 - \zeta^2)b_j^l - \zeta c_j^l = 0\\
\zeta(\bar{e}_{31} + \bar{e}_{15})\nabla^2 + \bar{e}_{15}\nabla^2 - \zeta^2)a_j^l + \zeta\bar{p}_3 b_j^l + (\zeta^2\bar{\epsilon}_{33} - \bar{\epsilon}\nabla^2)c_j^l = 0\\
\bar{\beta}\nabla^2 - \zeta a_j^l + (\bar{d} + i\bar{k}_3\zeta^2)b_j^l + \zeta\bar{p}_3 c_j^l = 0
\end{aligned}$$

3 Solution for linear elastic materials with voids

The displacement equations of motion and equation of equilibrated inertia for an isotropic LEMV are

$$(\lambda + 2\mu)(u_{,rr} + r^{-1}u_{,r} - r^{-2}u) + \mu u_{,zz} + (\lambda + \mu)w_{,zz} + \beta\aleph_{,r} = \rho u_{,tt} \tag{10a}$$

$$(\lambda + \mu)(u_{,rz} + r^{-1}u_{,z}) + \mu(w_{,rr} + r^{-1}w_{,r}) + (\lambda + 2\mu)w_{,zz} + \beta\aleph_{,z} = \rho w_{,tt} \tag{10b}$$

$$-\beta(u_{,r} + r^{-1}u) - \beta w_{,z} + \alpha(\aleph_{,rr} + r^{-1}\aleph_{,r} + \aleph_{,zz}) - \delta k\aleph_{,tt} - \omega\aleph_{,t} - \xi\aleph = 0 \tag{10c}$$

u,v,w represents displacements components along r, θ, and z directions $\alpha, \beta, \xi, \omega$ and k are LEMV material constants characterizing the core in the equilibrated inertial state,ρ is the density and λ, μ are the lame constants and $\aleph$ is the new kinematical variable associated with another material without voids. The stress in the LEMV core materials are

$$\begin{aligned}
\sigma_{,rr} = (\lambda + 2\mu)u_{,r} + \lambda r^{-1}u + \lambda w_{,z} + \beta\aleph\\
\sigma_{,rz} = \mu(u_{,r} + w_{,r})
\end{aligned}$$

The solution of (10) is taken as

$$u = \quad U_{,r}\exp i(kz + wt) \tag{11a}$$

$$w = (\frac{i}{h})W\exp i(kz + wt) \tag{11b}$$

$$\aleph = (\frac{1}{h^2})\aleph\exp i(kz + wt) \tag{11c}$$

Substitution of the (11) into (10) with non-dimensional variables x and ζ, can be reduced as

$$\begin{vmatrix}
(\lambda + 2\mu)\nabla^2 + F_1 & -F_2 & F_3\\
F_2\nabla^2 & \bar{\mu}\nabla^2 + F_4 & F_5\\
-F_3\nabla^2 & F_5 & \alpha\nabla^2 + F_6
\end{vmatrix}(U, W, \aleph)^T = 0 \tag{12}$$

where $\nabla^2 = \frac{\partial^2}{\partial x^2} + \frac{1}{x}\frac{\partial}{\partial x}$ $F_1 = \frac{\rho}{\rho^1}(ch)^2 - \bar{\mu}\zeta^2$ $F_2 = (\bar{\lambda}+\bar{\mu})\zeta$,$F_3 = \bar{\beta}$ $F_4 = \frac{\rho}{\rho^1}(ch)^2 - (\bar{\lambda}+\bar{\mu})\zeta^2$ $F_5 = \bar{\beta}\zeta$ $F_6 = \frac{\rho}{\rho^1}(ch)^2\bar{k} - \bar{\alpha}\zeta^2 - i\bar{\omega}(ch) - \bar{\xi}$ and $\bar{\lambda} = \frac{\lambda}{c_{44}^l}$,$\bar{\mu} = \frac{\mu}{c_{44}^l}$,$\bar{\alpha} = \frac{\alpha}{h^2 c_{44}^l}$,$\bar{\beta} = \frac{\beta}{c_{44}^l}$,$\bar{\xi} = \frac{\xi}{c_{44}^l}$,$\bar{\omega} = \frac{\omega}{h}(c_{44}^l\rho)^{\frac{1}{2}}$,$\bar{K} = \frac{k}{h^2}$. The above (12) can be specified as,

$$(\nabla^6 + P\nabla^4 + Q\nabla^2 + R)(U, W, \aleph) = 0 \tag{13}$$

Thus the solution of (13) can be given as follows,

$$U = \sum_{j=1}^{3}[A_j J_0(\alpha_j ax) + B_j Y_0(\alpha_j x)] \tag{14a}$$

$$W = \sum_{j=1}^{3} d_j[A_j J_0(\alpha_j x) + B_j Y_0(\alpha_j x)], \tag{14b}$$

$$\aleph = \sum_{j=1}^{3} e_j[A_j J_n(\alpha_j x) + B_j Y_n(\alpha_j x)] \tag{14c}$$

$(\alpha_j x)^2$ are the roots of the equation when replacing $\nabla^2 = -(\alpha_j x)^2$. The arbitrary constant d_j and e_j are obtained from

$$\begin{aligned}
F_2\nabla^2 + (\bar{\mu}\nabla^2 + F_4)d_j + F_5 e_j = 0\\
-F_3\nabla^2 + F_5 d_j + (\alpha\nabla^2 + F_6)e_j = 0
\end{aligned}$$

The governing equation for CFRP core material can be obtained from (10) by taking the void volume fraction $\aleph = 0$ and the lames constants as $\lambda = c_{12}, \mu = \frac{(c_{11}-c_{12})}{2}$.

4 Boundary condition and frequency equation

We consider a wave propagation problem of piezo thermo elastic multilayered rotating rod with adhesive as LEMV/CFRP under the effect of the axisymmetric rotation field. The frequency equations of the problem can be obtained using the following boundary conditions.
(i) At the inner and outer surface of solid rod with free traction
$\sigma_{rr}^{l} = \sigma_{rz}^{l} = E^{l} = T^{l} = 0$ With $l = 1, 3$.
(ii) At the solid and adhesive interface
$\sigma_{rr}^{l} = \sigma_{rr}; \sigma_{rz}^{l} = \sigma_{rz};$
(iii)Thermally insulated and Electrically shorted Boundary conditions
$T^{l} = 0$ and $E^{l} = 0;$

Using the values of $\phi^{l}, W^{l}, E^{l}, T^{l}$ and $U, W, \aleph$ from the (9) and (14), the above boundary conditions will give a system of homogeneous algebraic equations for the unknown constants A_1^l, A_2^l, A_3^l, A_4^l, A_1, A_2 and A_3.This set of equations can be written in the following 20×20 vanishing determinant form

$$|(Y_i j)| = 0, (i, j = 1, 2, 3, ..., 20) at x = x_1, where j = 1, 2, 3, 4 \tag{15}$$

At $x = x_1$ where $j = 1, 2, 3, 4$

$$\begin{aligned}
Y_{1j} &= 2c_{66}^{-}n(n-1)J_n(\alpha_j^l a x_1) + (\alpha_j^l a x_1)J_{n+1}(\alpha_j^l a x_1)] - x^2[(\alpha_j a)^2 c_{11}^{-} + \zeta c_{13}^{-} a_j + \zeta b_j + \bar{\beta} c_j]J_n(\alpha_j^l a x_1) \\
Y_{1,j+4} &= -[2\bar{\mu}(\alpha_j x_1)J_n(\alpha_j x_1) + (\bar{\lambda} + \bar{\mu})(\alpha_j)^2 + \bar{\beta} e_j - \bar{\lambda}\zeta \bar{d}_j]J_0(\alpha_j x_1) \\
Y_{2j} &= 2n[(\alpha_j^1 a x_1)J_{n+1}(\alpha_j^l a x_1) - (n-1)J_n(\alpha_j^l a x_1)] \\
Y_{2,j+4} &= -\bar{\mu}(\epsilon + d_j)(\alpha_j)J_1(\alpha_j x_1) \\
Y_{3j} &= (\zeta + a_j + \bar{e}_{15} b_j)[nJ_n(\alpha_j^1 a x_1) - (\alpha_j a x)J_{n+1}(\alpha_j^1 a x_1)] \\
Y_{3,j+4} &= -(\alpha_j)J_1(\alpha_j x_1) \\
Y_{4,j} &= (e_{15}^{-}\zeta a_j - \epsilon_{11}^{-} b_j)[nJ_n(\alpha_j^1 a x_1) - (\alpha_j^1 a x_1)J_{n+1}(\alpha_j^1 a x_1)] \\
Y_{4,j+4} &= -d_j J_0(\alpha_j x_1) \\
Y_{5j} &= e_j^l J_0(\alpha_j^l x_1) \\
Y_{6j} &= x_1 J_0(\alpha_j^l x_1) - (\alpha_j^l)J_1(\alpha_j^l x_1) \\
Y_{7,j+4} &= e_j(\alpha_j)J_1(\alpha_j^l x_1)
\end{aligned}$$

and the other nonzero elements at the interface $x = x_1$ can be obtained on replacing J_0 by J_1 in the above elements. They are Y(i,j+7),(i=1,2,3,4,5,6,7).The components at the interface $x = x_2$ by varying j from 5 to 7 are replaced the subscript x_1 by x_2 and the other nonzero elements at the interface $x = x_2$ are calculated by replacing J_0 in to J_1 in the above elements. They are Y(i,j+3),Y(i,j+10)(i=8,9,10,11),Y(12,j+10),Y(13,+10) and Y(14,j+3). At the outer surface $x = x_3$ the non zero elements by varying j=11,12,13,14 are replaced subscript x_1 by x_3 in the above elements. The other nonzero element at the interface $x = x_3$ can be obtained on replacing J_0 by J_1 in the above elements. They are Y(i,j+4),(i=15, 16, 17, 18).

5 Numerical computation and discussion

The purpose of the present study is demonstrating the various applications of composite materials with different adhesive core materials. The material chosen for the numerical calculation is PZT-5A. The physical data of PZT-5A are taken from Sharma et al. (2004) and are used for the numerical calculation:
$C_{11} = 13.9 \times 10^{10} Nm^{-2}; C_{12} = 7.78 \times 10^{10} Nm^{-2}; C_{13} = 7.43 \times 10^{10} Nm^{-2}; C_{33} = 11.5 \times 10^{10} Nm^{-2}; C_{44} = 2.56 \times 10^{10} Nm^{-2}; C_{66} = 3.06 \times 10^{10} Nm^{-2}; \beta_1 = 1.52 \times 10^{6} NK^{-1}m^{-2}; \beta_3 = 1.53 \times 10^{6} NK^{-1}m^{-2}; T_0 = 298K; C_v = 420 jkg^{-1}K^{-1}; p_3 = -452 \times 10^{-6} CK^{-1}m^{-2}; K_1 = K_3 = 1.5 Wm^{-1}K^{-1}; e_{13} = -6.98 Cm^{-2}; e_{33} = 13.8 Cm^{-2}; e_{15} = 13.4 Cm^{-2}; \epsilon_{11} = 60^{10} CN^{-1}m^{-2}; \epsilon_{33} = 54.7 \times 10^{1}0 CN^{-1}m^{-2}; \rho = 7750 Kgm^{-2};$
The frequency (15) are essentially an implicit transcendental equation of the unknown frequency parameter and wave number for the given boundary conditions. The results of the present investigation are displayed in Figs. 2 – 7. In Figs. 2 and 3 the variations of the non-dimensional frequency of a thermo piezoelectric multilayered solid rod with respect to the parameter ($\Omega = 0, 0.2, 0.4$) have been shown for different values of the wave number to the solid rod. From Fig. 2 it is observed that the non-dimensional frequency of the solid rod shows some dispersion from the linear behavior of frequency with respect to Ω for the increasing wave number parameter k.But in Fig. 3 almost linear variation with respect to Ω for the increasing wave number parameter k without thermal impact. In both cases at small values of the parameter k the values of frequency are almost steady for different values of the rotating parameter Ω,where the higher values of k the frequency starting dispersive only including thermal impact but maintain the same behavior for without thermal impact of the rod.

In Figs. 4 and 5 the variations of the non-dimensional frequency of a thermo piezoelectric multilayered solid rod with respect to the parameter ($\Omega = 0, 0.2, 0.4$) have been shown for different values of the thickness to the solid rod. From Fig. 4 it is observed that the non-dimensional frequency of the solid rod shows almost linear behavior of frequency with respect to Ω for the increasing

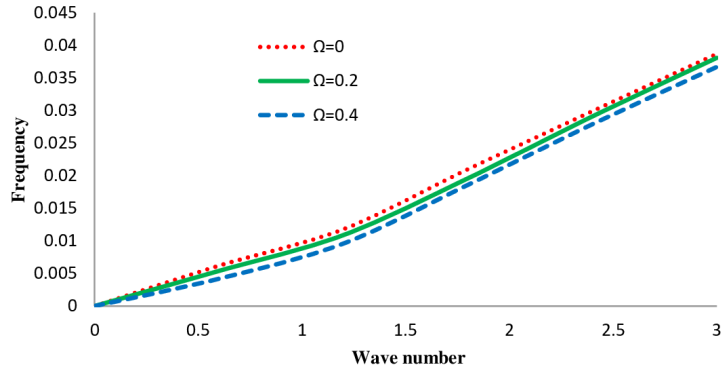

Fig. 2: Variation of dimensionless frequency against wave number at$\beta = 0$ with various rotating speed.

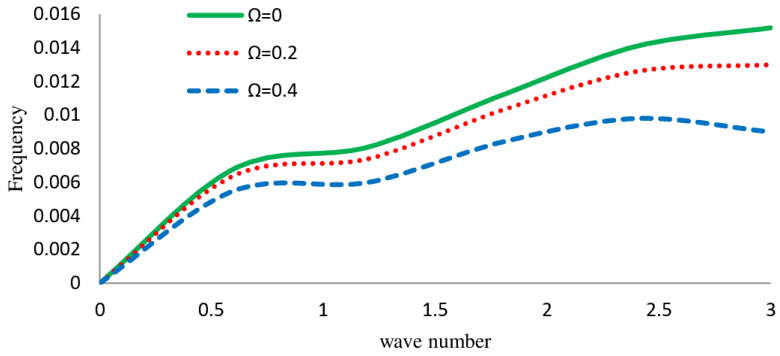

Fig. 3: Variation of dimensionless frequency against wave number at $\beta = 0.5$ with various rotating speed.

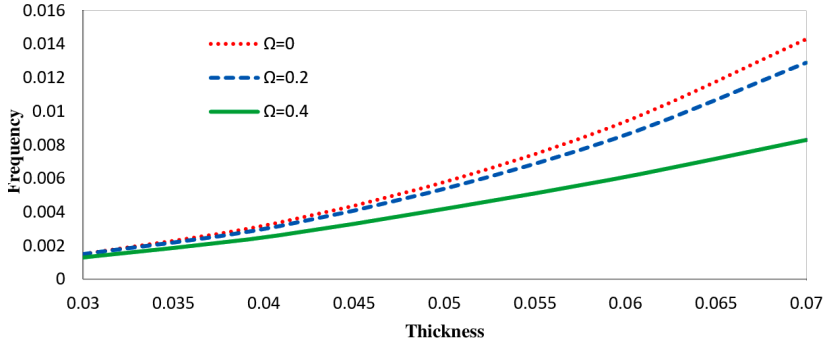

Fig. 4: Variation of dimensionless frequency against wave number at $\beta = 0$ with various rotating speed.

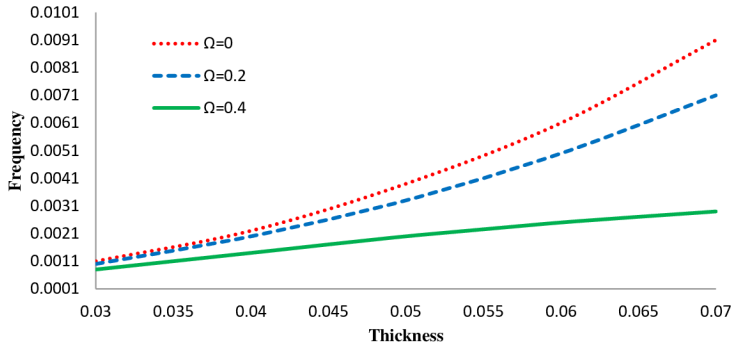

Fig. 5: Variation of dimensionless frequency against thickness at$\beta = 0.5$ with various rotating speed.

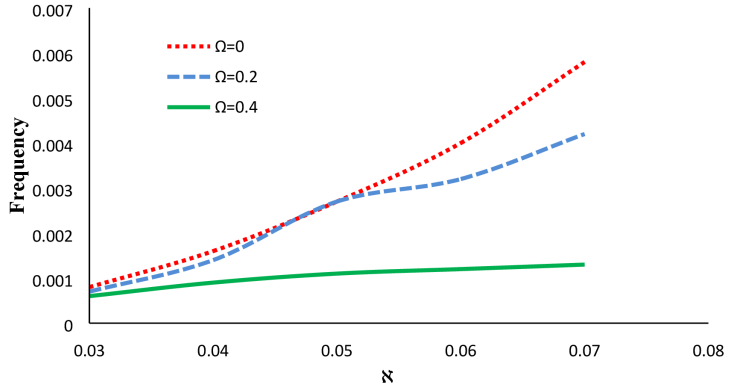

Fig. 6: Variation of dimensionless frequency against volume fraction $\aleph$ at $E = 0$ with various rotating speed.

thickness parameter.Also in Fig. 5 almost linear variation is observed with respect to Ω for the increasing thickness parameter.In both cases different values of the parameter the values of frequency are almost steady for different values of the rotating parameter Ω, further these two results shows the thermal impact of the solid rod is not significant in order increasing of parameters thickness h and rotating speed Ω of the solid rod.

The variation of the non-dimensional frequency with respect to the volume fraction $\aleph$ and different rotating speed for thermo piezoelectric multilayered rotating rod is shown in Figs. 6 and 7 respectively.From Fig 6 almost linear variation observed with respect to Ω for the increasing parameter $\aleph$ without electric impact.But in Fig.7 it is clear the frequency of the rod increases monotonically to attain maximum value in $\aleph = 2$ and slashes down to remaining range of $\aleph$ for different parameter ($\Omega = 0, 0.2, 0.4$) with electric impact. The 3D Figs 8-9 clarifies the variation of non dimensional frequency against wave number for the two different layers LEMV and CFRP of thermos piezo electric composite rod. These figures explain the dependence of the core materials in the frequency. The 3D Figs 10-11 clarifies the variation of non dimensional frequency against thickness for the two different layers LEMV and CFRP of thermopiezoelectric composite rod. These figures explain the dependence of the core materials in the frequency.

The 3D Figs 12-13 clarifies the variation of non dimensional frequency against β for the two different layers LEMV and CFRP of thermopiezoelectric composite rod. These figures explain the dependence of the core materials in the frequency.

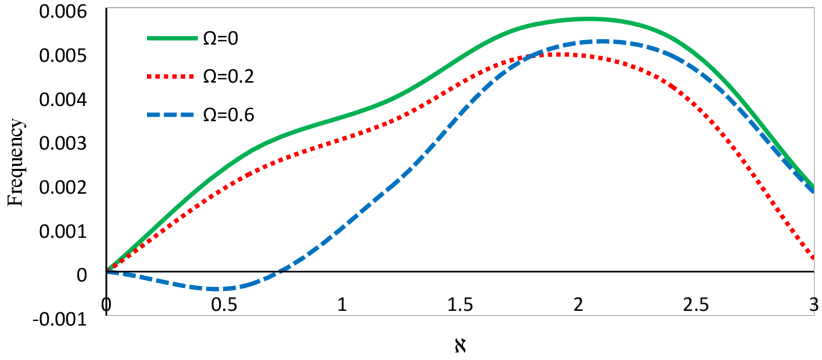

Fig. 7: Variation of dimensionless frequency against volume fraction $\aleph$ at $E = 0.5$ with various rotating speed.

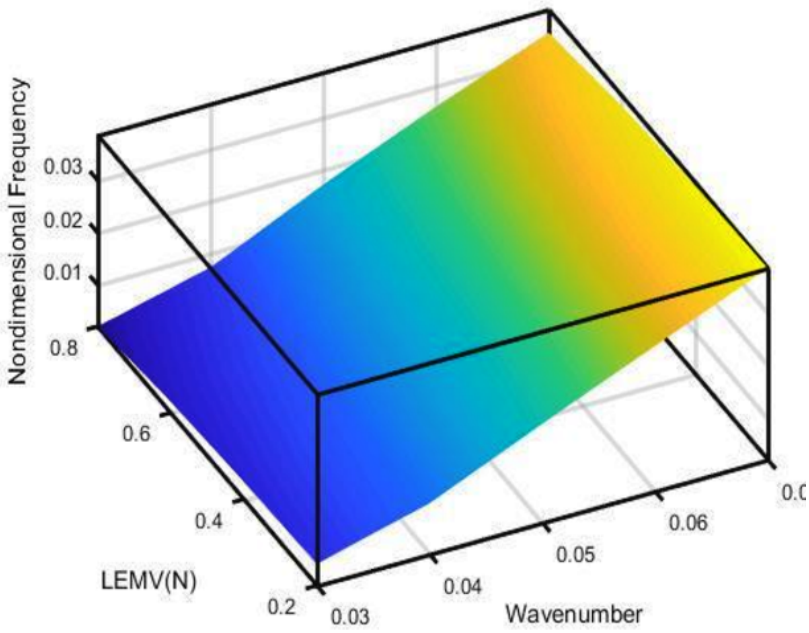

Fig. 8: Variation of dimensionless frequency against wave number and LEMV core in thermo piezoelectric multilayered rod with $\Omega = 0.5$

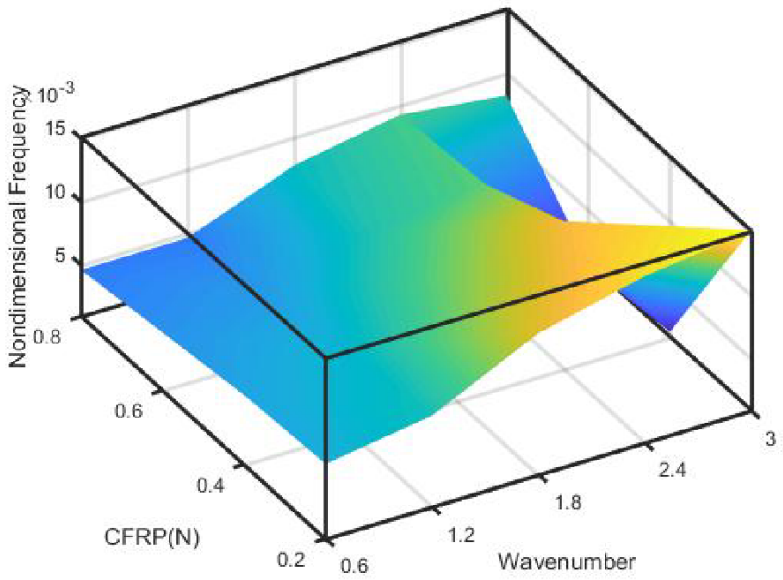

Fig. 9: Variation of dimensionless frequency against wave number and CFRP core in thermo piezoelectric multilayered rod with $\Omega = 0.5$

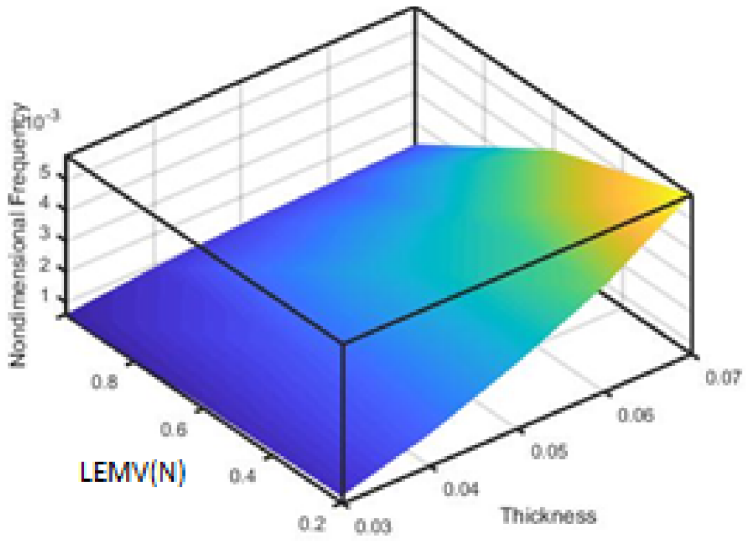

Fig. 10: Variation of dimensionless frequency against thickness and LEMV core in thermo piezoelectric multilayered rod with $\Omega = 0.5$

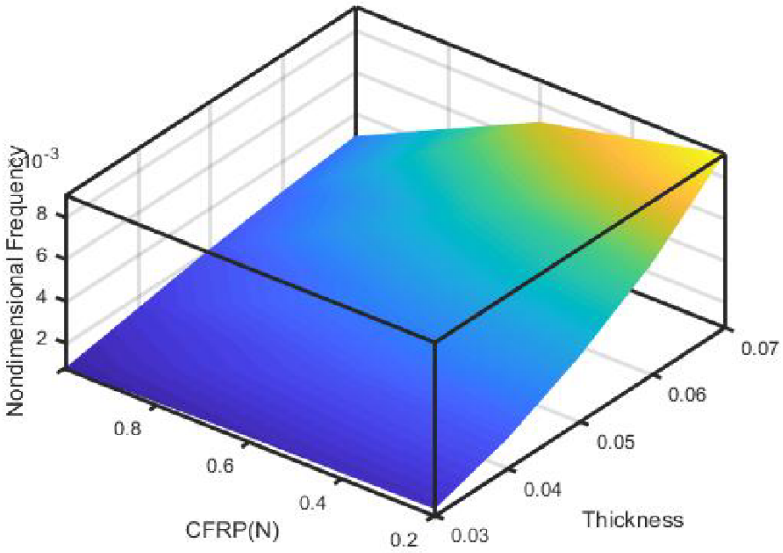

Fig. 11: Variation of dimensionless frequency against thickness and CFRP core in thermo piezoelectric multilayered rod with $\Omega = 0.5$

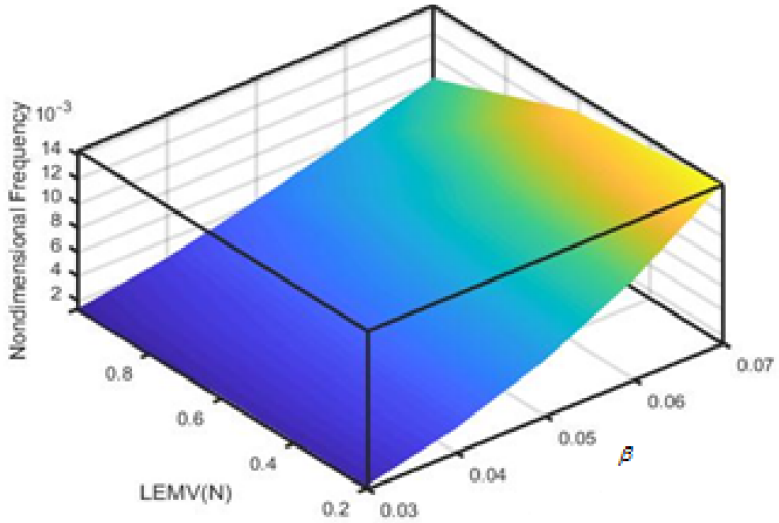

Fig. 12: Variation of dimensionless frequency against β and LEMV core in thermo piezoelectric multilayered rod with $\Omega = 0.5$

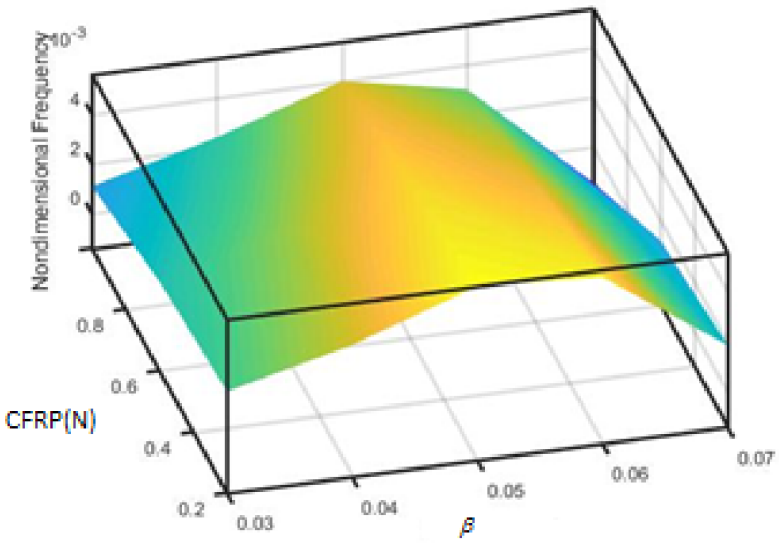

Fig. 13: Variation of dimensionless frequency againstβ and CFRP in thermo piezoelectric multilayered rod with $\Omega = 0.5$

6 Conclusion

The free wave propagation in a multilayered piezothermoelastic rotating rod with LEMV/CFRP interface is discussed using three-dimensional linear theory of elasticity. Three displacement potential functions are introduced to uncouple the equations of motion, electric and heat conduction. The frequency equation of the system consisting of rotating piezothermoelastic rod is developed under the assumption of thermally insulated and electrically shorted free boundary conditions at the surface of the rod. The analytical equations are numerically studied through the MATLAB programming for axisymmetric modes of vibration for PZT-5A material. The computed numerical results are presented as dispersion curves for the variation of frequency against the various physical quantities with thermal and electrical parameters together with rotational speeds. The rotation, thermal and electrical fields have a great role in frequency distribution, since the amplitudes of these frequency modes are varying with the increase of the field values. We concluded that the deformation of a body depends on the nature of the applied forces and rotational effect as well as the type of boundary conditions. The result provides a motivation to investigate the free wave propagation in a multilayered piezothermoelastic rotating rod with LEMV/CFRP core as a new class of applications elastic solids. The methods used in the present article are applicable to a wide range of problems in elasticity

References

Farhang Honarvar, Esmaeil Enjilela, Anthony N Sinclair, and S Abbas Mirnezami. Wave propagation in transversely isotropic cylinders. *International journal of solids and structures*, 44(16):5236–5246, 2007. doi: //org/10.1016/j.ijsolstr.2006.12.029.

HS Paul and GV Raman. Wave propagation in a hollow pyroelectric circular cylinder of crystal class 6. *Acta mechanica*, 87(1-2): 37–46, 1991. doi: //org/10.1007/BF01177170.

RD Mindlin. Equations of high frequency vibrations of thermopiezoelectric crystal plates. *International Journal of Solids and Structures*, 10(6):625–637, 1974. doi: //org/10.1016/0020-7683(74)90047-X.

HS Paul and Ganapathy V Raman. Wave propagation in a pyroelectric cylinder of arbitrary cross section with a circular cylindrical cavity. *The Journal of the Acoustical Society of America*, 93(2):1175–1181, 1993. doi: org/10.1121/1.405512.

VI Storozhev. Propagation of electroelastic waves in multilayer piezoelectric cylinders with a sector notch. *International applied mechanics*, 49(2):194–202, 2013. doi: //org/10.1007/s10778-013-0559-9.

VK Nelson and S Karthikeyan. Axisymmetric vibration of pyrocomposite solid cylinder. *i-Manager's Journal on Future Engineering and Technology*, 4(1):69, 2008a. doi: //org/10.26634/jfet.4.1.583.

VK Nelson and S Karthikeyan. Axisymmetric vibration of pyrocomposite hollow cylinder. *World Academy of Science Engineering and Technology International Journal of Mathematical Computational Physical Electrical and Computer Engineering*, 2008b.

NA Shulga. Propagation of harmonic waves in anisotropic piezoelectric cylinders. compound waveguides. *International applied mechanics*, 38(12):1440–1458, 2002. doi: 10.1023/A:1023205707153.

Jia Hua, Jing Mu, et al. Guided wave propagation and focusing in multi-layer pipe with viscoelastic coating and infinite soil media. *Materials Evaluation*, 71(3), 2013.

A Tasdemirci, Ian W Hall, Bazle A Gama, and M Guden. Stress wave propagation effects in two-and three-layered composite materials. *Journal of Composite Materials*, 38(12):995–1009, 2004. doi: //org/10.1177/0021998304040564.

B Singh and V Saxena. Axisymmetric vibration of a circular plate with double linear variable thickness. *Journal of Sound and Vibration*, 179(5):879–897, 1995. doi: 10.1006/jsvi.1996.0058.

AM Abd-Alla and SR Mahmoud. Magneto-thermoelastic problem in rotating non-homogeneous orthotropic hollow cylinder under the hyperbolic heat conduction model. *Meccanica*, 45(4):451–462, 2010. doi: 0.1007/s11012-009-9261-8.

AM El-Naggar, AM Abd-Alla, MA Fahmy, and SM Ahmed. Thermal stresses in a rotating non-homogeneous orthotropic hollow cylinder. *Heat and Mass Transfer*, 39(1):41–46, 2002. doi: //org/10.1007/s00231-001-0285-4.

AM Abd-Alla, AN Abd-Alla, and NA Zeidan. Thermal stresses in a nonhomogeneous orthotropic elastic multilayered cylinder. *Journal of Thermal Stresses*, 23(5):413–428, 2000. doi: //org/10.1080/014957300403914.

AM Abd-All, AN Abd-Alla, and NA Zeidan. Transient thermal stresses in a rotation non-homogeneous cylindrically orthotropic composite tubes. *Applied mathematics and computation*, 105(2-3):253–269, 1999. doi: 10.1115/1.3176098.

R Selvamani. Wave propagation in a rotating disc of polygonal cross-section immersed in an inviscid fluid. *Cogent Engineering*, 2(1):1002162, 2015. doi: 10.1080/23311916.2014.1002162.

Stephen C Cowin and Jace W Nunziato. Linear elastic materials with voids. *Journal of Elasticity*, 13(2):125–147, 1983. doi: //org/10.1007/BF00041230.

JN Sharma, Mohinder Pal, and Dayal Chand. Three-dimensional vibration analysis of a piezothermoelastic cylindrical panel. *International journal of engineering science*, 42(15-16):1655–1673, 2004.

TECHNISCHE MECHANIK
an open access journal

journal homepage: www.ovgu.de/techmech

Tech. Mech., Vol. 39, Is. 3, (2019), 252–260

Received: 16.04.2019
Accepted: 31.07.2019
Available online: 01.10.2019

The effect of the skin-core structure of injection-molded isotactic polypropylene on the stress distribution in bending tests

R. Glüge[1⋆], N. Mahmood[3], I. Kolesov[2], H. Altenbach[1], M. Beiner[3,4], R. Androsch[2]

[1] Otto von Guericke University Magdeburg, Universitätsplatz 2, D-39106 Magdeburg, Germany
[2] Martin Luther University Halle-Wittenberg, Interdisciplinary Center for Transfer-oriented Research in Natural Sciences (IWE TFN), D-06099 Halle/S., Germany
[3] Martin Luther University Halle-Wittenberg, Faculty for Natural Science II, Institute for Chemistry, Heinrich-Damerow-Str. 4, D-06120 Halle/S., Germany
[4] Fraunhofer IMWS, Walter-Hülse-Str. 1, D-06120 Halle/S., Germany

Abstract: We examine the effect of the skin-core structure of isotactic polypropylene (iPP) in bending tests. The depth-dependent material properties are determined in tensile tests and mapped to a finite element model. This enables the examination of internal stresses during bending numerically. In a bending test, one usually expects a monotonic stress distribution across the thickness, provided that the material is homogeneous and does not strain-soften. We found that the structural gradient of injection-molded iPP easily overcompensates the monotonic stress dependence, such that the maximal equivalent von Mises stress lies well below the surface in the so called shear layer. The latter is a result of the injection molding process.

Keywords: polypropylene, bending, skin-core gradient, microtoming, elastic-plastic

1 Introduction

Polymer parts are usually produced by injection molding, where the polymer melt is injected into a cavity. Injection molding can produce both simple and intricate parts with high production output and high efficiency. During the process, the semicrystalline microstructure of the polymer forms under shear and thermal gradients, which cause variable morphologies between the skin and core of the molded sample. The resulting, often stratified microstructure affects the structural mechanical properties of the product. As a net result of the effects of shear, pressure, and thermal fields during injection molding, skin-core morphologies that exhibit a layer-like or gradient structure, where the orientation of macromolecules and crystals, the crystallinity and the crystalline-amorphous superstructure depend on the distance from the surface (Housmans et al. (2009); Katti and Schultz (1982); Russell and Beaumont (1980); Drummer and Meister (2014)).
Therefore, polymeric gradient materials are produced naturally upon injection molding, even when the cooling or the shear flow is not controlled explicitly. The skin-core microstructure was studied, e.g. in Fujiyama et al. (1988); Wen et al. (2004); Housmans et al. (2009); van der Meer (2003), among many others. Extended accounts to the structure formation in solidifying polymers and injection molding technology can be found in Kamal et al. (2009); Zheng et al. (2011). Here, the focus is on the mechanical skin layer effects in elasticity and at small plastic deformations.
A typical load case for thin-walled plastic components is bending, hence bending tests are commonly used to characterize polymer properties, see, e.g. Bledzki et al. (2015). In bending, stresses are usually highest at the surface, since the strains grow monotonically from the mid-plane. For the same reason, the mechanical properties of the surface affect the effective flexural properties disproportionately. Bending tests offer some advantages: Bending samples can neither neck (like in tensile tests) or buckle (like in compression tests), hence they are a versatile tool to characterize the mechanical properties beyond what can be obtained from uniaxial tests. However, unlike tensile tests, the structural properties (like force-displacement curves) cannot be mapped directly to material properties due to the inhomogeneous deformation. Only with simplifying assumptions, like material homogeneity and small strains, one can identify the material properties from measuring forces and displacements. Both presumptions are shaky for injection-molded iPP parts, which makes it difficult to obtain material parameters for materials with a depth-gradient in the material properties.
Furthermore, it raises questions regarding the stress distribution. One might expect the surface to be the most critical region for crack nucleation in bending, as it combines inhomogeneities (e.g. scratches) with the highest stresses. We were unable to find an examination of the stress distribution across the thickness which takes into account both the bending state and the material property gradient. We approach this gap by characterizing the material properties layer-wise and mapping the depth-dependent material data to a finite element (FE) model of a bending test. We find that the softer skin layer may well overcompensate this monotonic stress increase, leading the stress maximum approximately 0.5 mm to 0.7 mm *below* the surface in bending samples of 4 mm thickness. Near the surface, a drop of the equivalent von Mises stress of approximately 20 % is observed.

⋆ E-mail address: gluege@ovgu.de
doi: 10.24352/UB.OVGU-2019-023

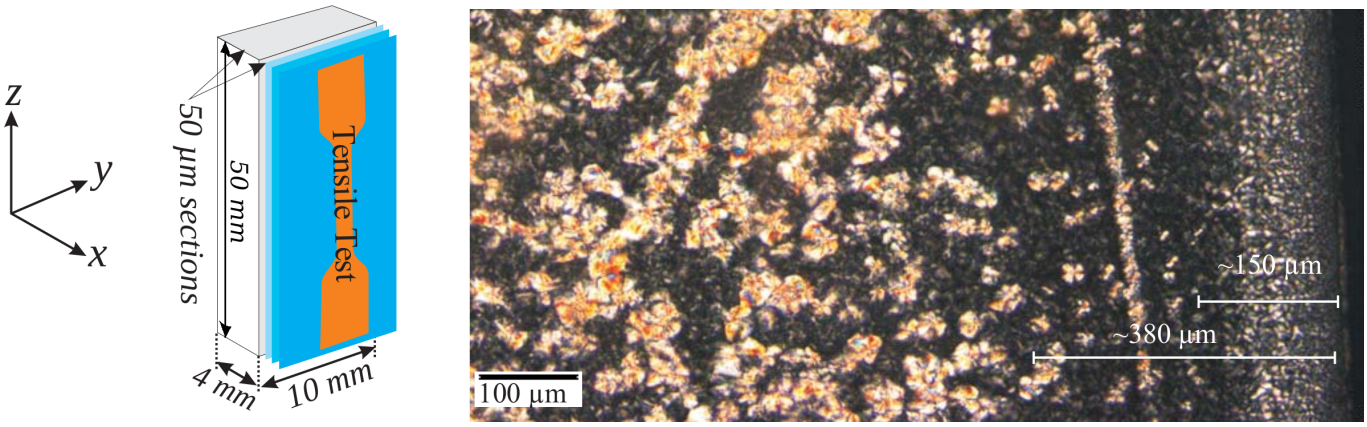

Figure 1: Left: Geometry of an injection-molded iPP sample for bending tests, the injection nozzle is at the center of the bottom plane. Right: micrograph inside the $x-z$-plane showing skin (right) and core (left) structure of a typical injection molded iPP sample.

2 Sample preparation and material characterization

2.1 Injection molding of the iPP samples

We manufactured bars of commercial iPP (Borealis HJ120UB) of dimensions 45 mm × 10 mm × 4 mm (see Fig. 1), using a BOY XS injection molding machine. The iPP was heated up to 200 °C. The mold temperature was 40 °C. The injection pressure was 350 bar. With these parameters, the filling time was about 1 to 2 seconds. After filling, a subsequent holding phase with a duration of 20 s and a holding pressure of 60 bar was applied. Subsequent cooling to room temperature under ambient pressure lastet about 4 minutes.

2.2 Skin-core structure

The micrograph in Fig. 1 gives an impression of the skin-core structure. It was examined thoroughly in a similar setup for different iPP materials and a sample width of 2 mm in Housmans et al. (2009). They distinguish four layers, namely the skin layer, the transition layer, the shear layer and the isotropic core. These layers have different main characteristics:

- The skin layer is cooled fastest, and has therefore the lowest crystallinity.
- The transition layer gets cooled down rapidly and sheared at the same time, which causes the polymer chains to orient collectively.
- The shear layer forms due to the interaction of the solidified skin layer and the flowing melt in the core during the injection. The shear layer has a higher crystal fraction, since it solidifies from the regular chain orientation from the transition layer. When the shear rate exceeds a critical value, the formation of crystal nuclei, as well as formation of β-crystals is observed.
- Regarding the isotropic core, the layers act as insulators, hence the core cools much slower without much shear flow, leading to an isotropic spherulitic structure.

The thickest layer is often the shear layer. Its thickness depends on the injection speed and ranges from 0.2 mm at high speeds to 1 mm at low speeds. It has a strong anisotropy and the highest β crystal fraction near the isotropic core (see Figs. 3, 4, 9 and 14 in Housmans et al. (2009)). Here, we join the very thin skin layer and the transition layer, which ranges from the surface to a depth of approximately 150 µm. The adjacent shear layer ranges to approximately 500 µm, where the isotropic core begins. These layer boundaries can be estimated by inspecting the polarized light image (Fig. 1). We also observed simultaneous changes of the depth-dependent material parameters at these depths. Nevertheless, since the transition is smooth, there is some vagueness in giving definite layer boundaries. We found that the fracture toughness that has been determined in tensile tests on thin slices is a good indicator, which shows a sudden drop between a depth of 400 µm and 500 µm. These results are collected in an upcoming article (Mahmood et al., N.D.).

2.3 Tensile testing of bulk specimen

The polymer block was clamped directly into a universal testing machine (Zwick/Roell Z010). The gauge length was assumed to be the clamping distance. The test speed was 27 mm/minute at a clamping distance of 27 mm, such that the nominal strain rate was $1/60\ \mathrm{s}^{-1} \approx 0.0176\mathrm{s}^{-1}$.

2.4 Tensile testing of thin films

The injection molded bars were cut in the y-z-plane into slices of 50 µm by stepwise microtoming from the surface to the core via a Leica SM2500E sectioning system. The toming direction was the z-direction. Tensile specimens (shouldered test bars) were punched out from these layers using a cutting-die unit according to ISO 527-2 Typ 5B. The positioning of the stencil was carefully adjusted to always cut out the shouldered test strip at the same position. The specimen size was $6 \times 35\ \mathrm{mm}^3$, with a specimen

gauge length of 12 mm. The tensile testing for the stress vs strain behavior was carried out on on a Zwick universal testing machine (Z010, Zwick/Roell) at room temperature and a testing speed of 12 mm/min. The testing speeds were adjusted in proportion to the gauge length, such that the nominal strain rate was the same ($1/60\ \mathrm{s}^{-1} \approx 0.0176\mathrm{s}^{-1}$) for all tests.
A total of 40 slices was examined, from a depth of 25 µm (mid-plane) to 1975 µm in steps of 50 µm. For each depth we averaged the results of at least 3 tests. For the largest sample set (7 slices) the standard deviation was less than 5% for Young's modulus. Some characteristic stress-strain curves are presented in Fig. 2 along with the fitted material model as detailed in the Sec. 2.5.

2.5 Material model

We did not examine the strain rate dependence in more detail. The material properties depend on the depth. We found the deformation plasticity theory using the Ramberg-Osgood-relationship (Ramberg and Osgood (1943)) to suit the stress-strain behaviour up to approximately 10 % of strain quite well at all depths, see Fig. 2 for some representative stress-strain curves. The Ramberg-Osgood-law gives the strains as an explicit function of the stresses

$$\varepsilon = \frac{1}{E}\left(\sigma + \frac{\sigma^n}{\sigma_\mathrm{y}^n}\right) \tag{1}$$

with three material parameters, where E is Young's modulus, σ_y the yield stress and n the hardening exponent. The Ramberg-Osgood-model does not introduce plastic strains but is a nonlinear elasticity which mimics an elastic-plastic behavior, similar to the deformation theory of plasticity by Hencky (1924) and Ilyushin (1947). Therefore, it cannot be applied if unloading or strain path changes occur.

Yield limit As can be seen in Fig. 2, a pronounced yield point is not visible. In such cases, the yield point is defined according to some rule, the well known 0.2 % residual strain rule is one example. For the Ramberg-Osgood law, the residual strain at σ_y is $1/E$. For our measurements of $E \approx 600$ MPa . . . 1200 MPa, this corresponds to a residual strain between $0.08\overline{3}$ % and $0.1\overline{6}$ %, i.e., a reasonable yield point definition.

Hardening Note that larger values of n imply less hardening, hence the inverse hardening exponent $1/n$ actually quantifies the hardening. $1/n$ is the slope of the stress-strain-curve beyond the yield point in a double logarithmic plot.

Fitting the parameters E, σ_y and n to the experimental data The three parameters were fitted by the least squares method to the experimental data in the strain interval from 0 to 10 %, which is just before necking occurs in most of the tests. This was done for all layers between 25 µm (mid-plane) and 1975 µm in steps of 50 µm. The adopted material parameters are plotted over the depth in Fig. 3. One can see that on the surface, stiffness, yield strength and hardening have a local minimum, which makes the surface the mechanically weakest part. Conversely, approximately 300 µm below the surface, Young's modulus and the inverse hardening exponent have a local maximum, while the yield stress remains roughly the same. At approximately 700 µm below the surface, Young's modulus has a local minimum, the yield stress a local maximum and the inverse hardening exponent drops to approximately 0.08. Since the core material is more brittle, there is an increased scattering of the results. In this depth range, the experimental data was replaced by a trend line, see Fig. 3.

3 Layer properties vs bulk properties

One may have noticed that the layer-wise stiffnesses and yield limits are somewhat lower than the bulk properties of iPP. Young's modulus lies usually between 1300 MPa and 1800 MPa, the yield stress lies mostly between 25 MPa and 35 MPa. Here, the average Young modulus of the layers is approximately 920 MPa, while the bulk's Young modulus is approximately 1320 MPa. Hence, the elastic properties are underestimated by a factor of approximately 0.7, see Fig. 2. At first glance, this is unexpected, since one might expect that the bulk Young modulus is close to the average of the layer-wise moduli. This systematic discrepancy is a result of the loss of scale separation. The layers exhibit, in proportion to the volume, a large surface with zero stresses, i.e. homogeneous stress boundary conditions. It is well known from homogenization theory that such samples underestimate the effective stiffness (see, e.g. Glüge et al. (2012)). Therefore, a fine discretization of the slices across the thickness is opposed by a loss of the scale separation. This is a fundamental dichotomy.
From a descriptive point of view, the layer's Young moduli are lower because of a lack of load distribution which is present in the bulk. Due to the inhomogeneity of the material, the local stresses deviate from the imposed uniaxial tensile state. Near the surface, the stresses confined to a plane stress state. This plays no big role in the bulk tensile tests, where the plane stress confinement makes up only a small portion. But in the layer-wise tests, the stresses are forced to be plane practically everywhere. This robs the slices of one dimension for the load distribution, as sketched in Fig. 4.
The loss of scale separation is larger in the core, since the core contains spherulites, the diameters of which are almost as large as the slice thickness of 50 µm (see Fig. 1). Near the surface, a finer microstructure prevails. This explains the increased scattering in the core Figs. 3.
Note that these observations apply to the effective elastic and plastic properties, although the effect appears less pronounced for the plasticity. For our fitting procedure, we found the bulk sample to have a yield limit of only 16 MPa, but in conjunction with an exceptionally high inverse hardening exponent of 0.18, such that the bulk is effectively stronger than most layers, see Fig. 2. Since for our bending tests the plastic properties are more relevant, we take the values as they were measured, keeping in mind that the overall stress levels, stiffness and strength of the bending sample are rather underestimated.

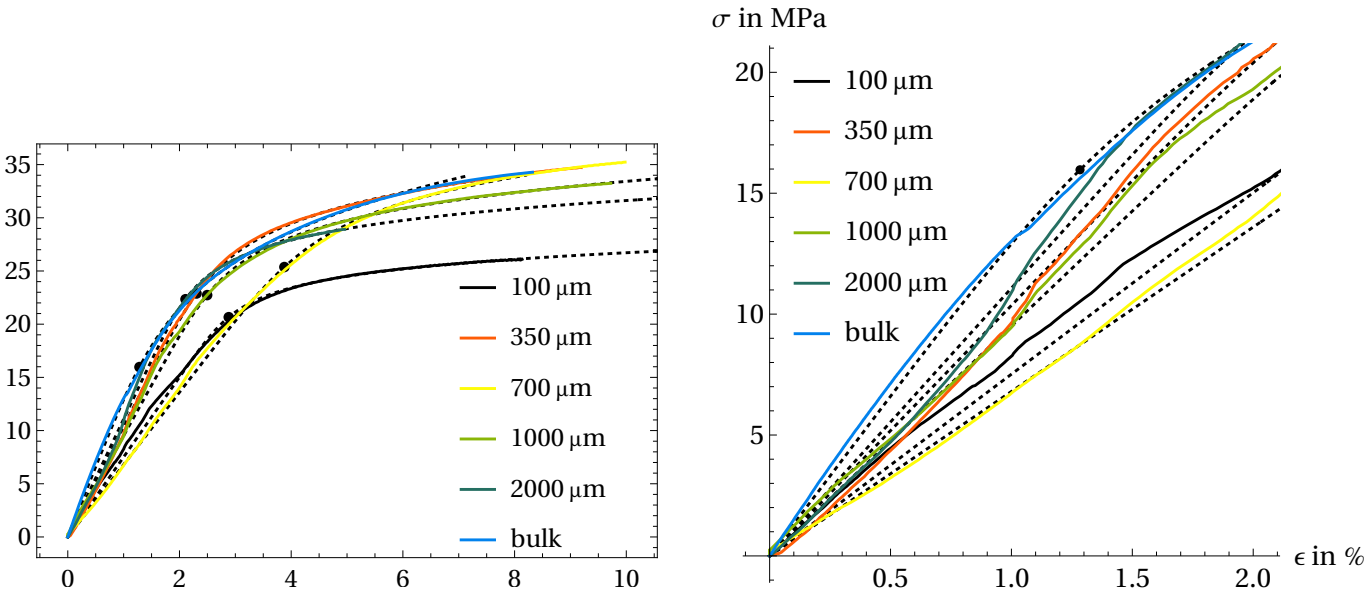

Figure 2: Left: True stress over engineering strain curves obtained on thin sections at different depths, where the number indicates the starting depth of the layer (e.g., ”100 µm” indicates the third layer, spanning the depth from 100 µm to 150 µm). The coloured solid lines correspond to the tensile test data, the black dotted lines represent the fitted material model (eq. 1). The black dots indicate the yield point as obtained from fitting the Ramberg-Osgood material parameters. The bulk stress strain curve shows a higher stiffness and strength than most layers. Only at a depth of 350 µm, the bulk stress is exceeded in a small interval. Right: Zoom on the elastic portion. The bulk's Young modulus is considerably larger than any of the Young moduli of the slices.

4 Bending tests

To examine the effect of the surface layer, bending tests were simulated numerically.

4.1 Test setup

The samples described in Sec. 2.1 were subjected to a three point bending test. Both bars ends jut out 10 % of the sample length of 45 mm, which leaves a load span of 36 mm. The loading head and the supporting points are freely rotating cylinders with a diameter of 8 mm. A sketch drawn to scale is given in Fig. 5.

4.2 Simulations

To examine the stress distribution, finite element (FE) simulations were devised.

4.2.1 Finite element setup

A finite element model of the bending test was created, for which we used the FE system Abaqus. We compared three different material property distributions, namely homogeneous core material (as found at a depth of 2 mm), homogeneous skin layer material (as found at the surface) and depth-dependent according to the material data as presented in Sec. 2.5. Due to the symmetry, only one half of the sample was modelled. The simple geometry of the sample calls for a structured mesh with hexahedral elements, with a mesh refinement near the surface and the contact points. An impression of the meshing is given in Fig. 6. To avoid shear locking, we used quadratic shape functions. The bending load head and the support points were modelled as rigid surfaces, since the steel barrels are much stiffer than the iPP. The barrels are in frictionless contact to account for the pivoted mounting. Since large deformations occur, a geometric nonlinear framework is used.

4.2.2 Simulation results

The most interesting result, namely the reduced surface stress due to the softer skin layer is depicted in Fig. 6 (FE model) and Figs. 8 to 9 (stress accross thickness).

Force displacement curves The force-displacement curves are depicted in Fig. 7. One can see that the pure skin material sample is much softer, compared to the pure core and the inhomogeneous samples. The latter do not differ significantly.

Stress distribution over depth The stress distribution is depicted along a line through the cross section in the center of the sample (see Fig. 6). One can see the typical compressive and tensile normal stresses as expected in a bending test in Fig. 8. It is also visible that the equivalent von Mises stress drops about 20 % near the surface, from approximately 30 MPa at a depth of

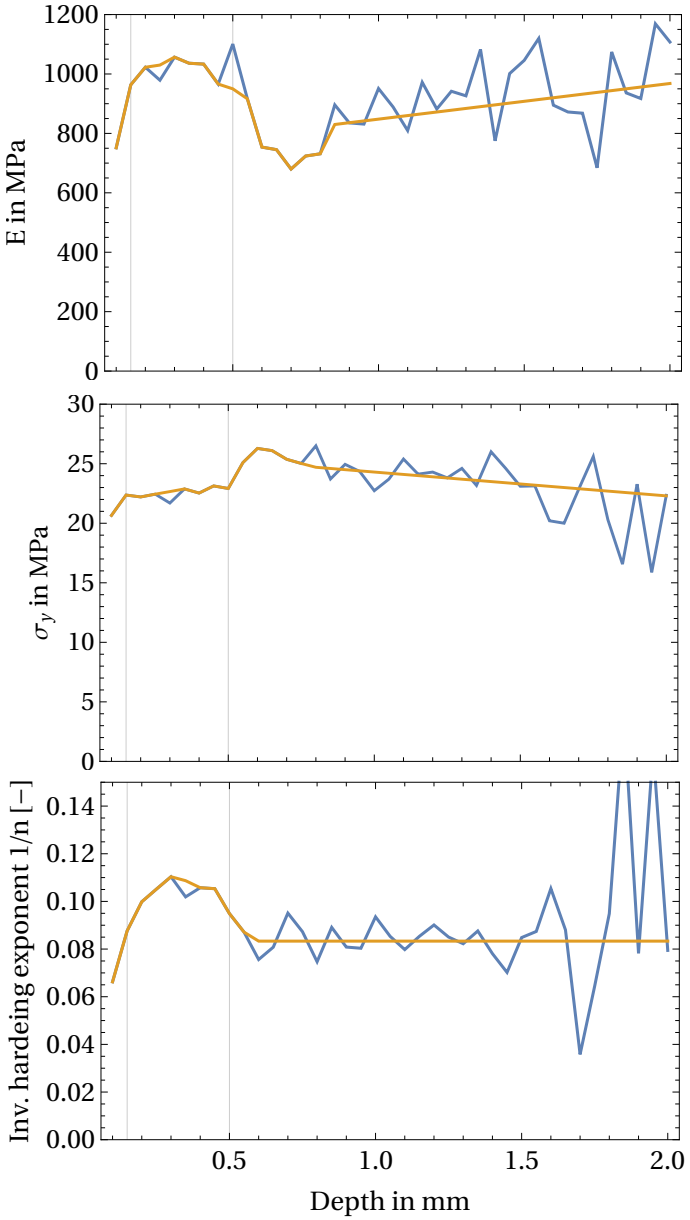

Figure 3: Young's modulus E, the yield stress σ_y and the inverse hardening exponent $1/n$ over the depth in mm as fitted to the tensile test data (blue) and after removal of the scattering via a trend line (yellow). One can see that stiffness, yield strength and hardening rate have a minimum at the surface. The vertical lines indicate the layer transitions.

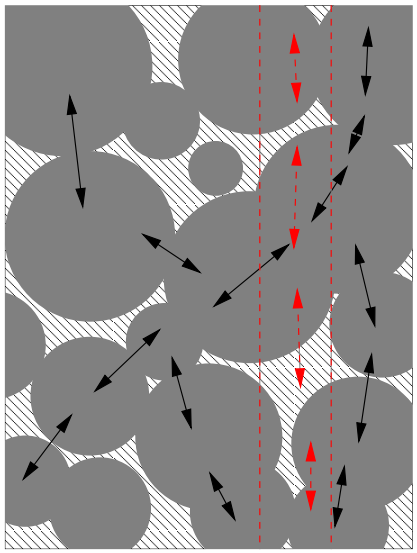

Figure 4: The semi-crystalline spherulites are much stiffer than the amorphous matrix. Under effective tension in the vertical direction, the load distribution runs mostly through adjacent spherulites. If the bulk is sliced, the load distribution is locally forced to run through the softer matrix, making the slices appear softer. Note that this is just a rough description of the load redistribution, it does not take into account more intricate effects that may take place at the phase boundaries.

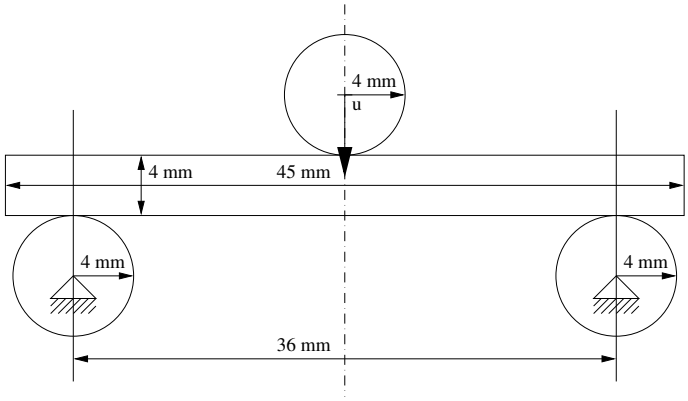

Figure 5: Bending setup drawn to scale.

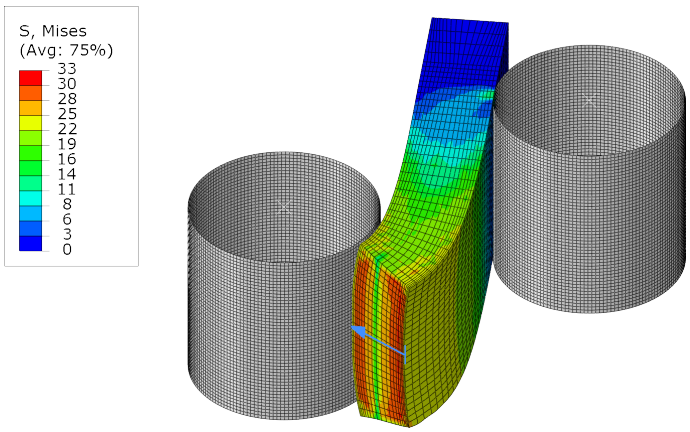

Figure 6: Equivalent von Mises stress distribution at a displacement of approximately 9 mm. One can see a considerable decrease of the equivalent von Mises stress in the skin layer. The stress distribution along the arrow is depicted in Fig. 9.

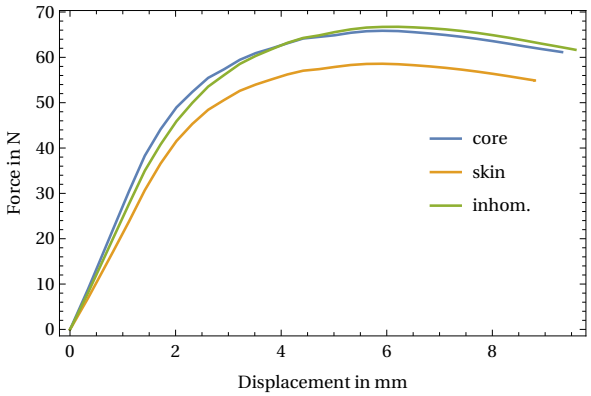

Figure 7: Force-displacement curves for the three cases (pure core material, pure skin material, inhomogeneous).

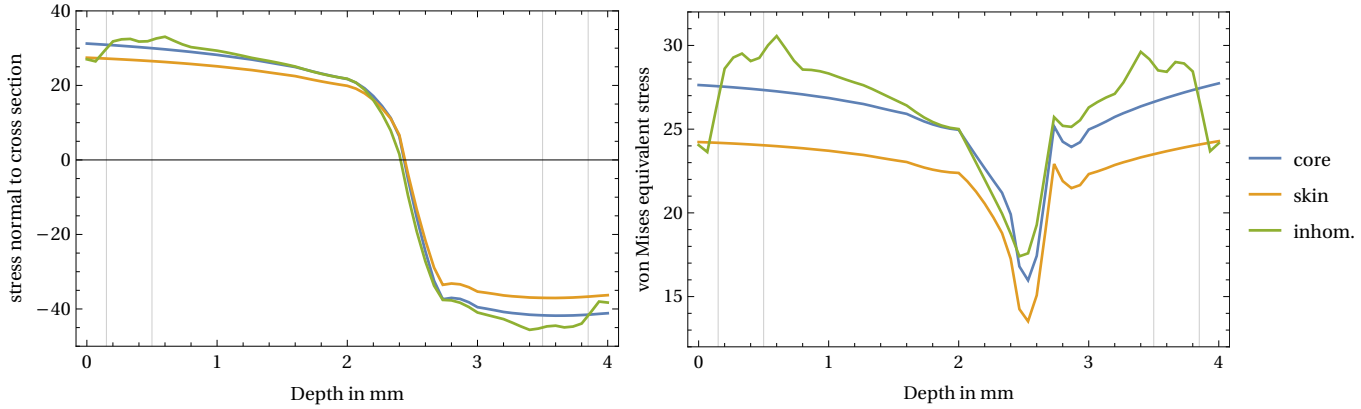

Figure 8: Left: Normal stress distribution through the bending sample near the bending load head for the three cases at the load maximum at a displacement u of approximately 9 mm. Note the slight shift of the neutral axis due to the large deflection and the compressive loading at the bending load head at a depth of 4 mm. The vertical lines indicate the layer boundaries between the skin- shear- and core layer. Right: Equivalent von Mises stress distributions for the three cases at different load head displacements. In the inhomogeneous case, a considerable stress drop near the surface is observed. The vertical lines indicate the layer boundaries between the skin- shear- and core layer.

approximately 500 µm to approximately 24 MPa at the surface. This effect is observed from the very beginning, but it is more pronounced the larger the strains become (see Fig. 9 top). This is in a sense counter-intuitive, as the outermost layers are subject to the largest strains in bending tests. We clearly see that the influence of the material property gradient is stronger than the approximately linear strain increase inside the cross section due to the bending.

5 Summary

We sliced a bulk iPP sample into layers of 50 µm thickness, the material properties of which were characterized in a tensile test. The material parameters were mapped to a finite element model of a bending test, of which the stress distribution across the thickness was analyzed. Our results can be summarized as follows:

- In the strain range up to 10 % and in the low strain rate limit, the tensile stress-strain behavior of iPP can be modeled well using the Ramberg-Osgood material law with only three parameters, namely Young's modulus, the yield stress and the inverse hardening exponent.
- Unfortunately, the layer-wise properties that were measured cannot be correlated directly with the bulk properties due to a loss of scale-separation. Either the discretization is coarse, or the layers are too thin to be representative. Specifically, the confinement to a plane stress state excludes a local load distribution mechanism in the microstructure, which makes the layers appear softer than the bulk. This affects the elastic properties, which are underestimated on average by a factor of approximately 0.7, more than the plastic properties.

  Since the spherulite size is larger in the core, the loss of scale separation is bigger in the core. This implies that the tensile tests underestimate the core stiffness more than the skin stiffness, which means that the unbiased material property gradient may be even stronger.
- The depth profile of these material parameters is rather complex, see Fig. 3. Going from the skin to the core, we find directly at the beginning of the skin/transition layer that all three parameters exhibit a local minimum ($E \approx 750$ MPa, $\sigma_y \approx 20$ MPa, $1/n \approx 0.06$), making the outermost layer softest and weakest. The adjacent shear layer from approximately 150 µm to ≈ 500 µm is stiffest and strongest, having a global maximum of Young's modulus of ≈ 1050 MPa and the inverse hardening exponent of ≈ 0.11 at a depth of ≈ 300 µm. In the shear zone, the yield stress increases monotonically. Near the start of

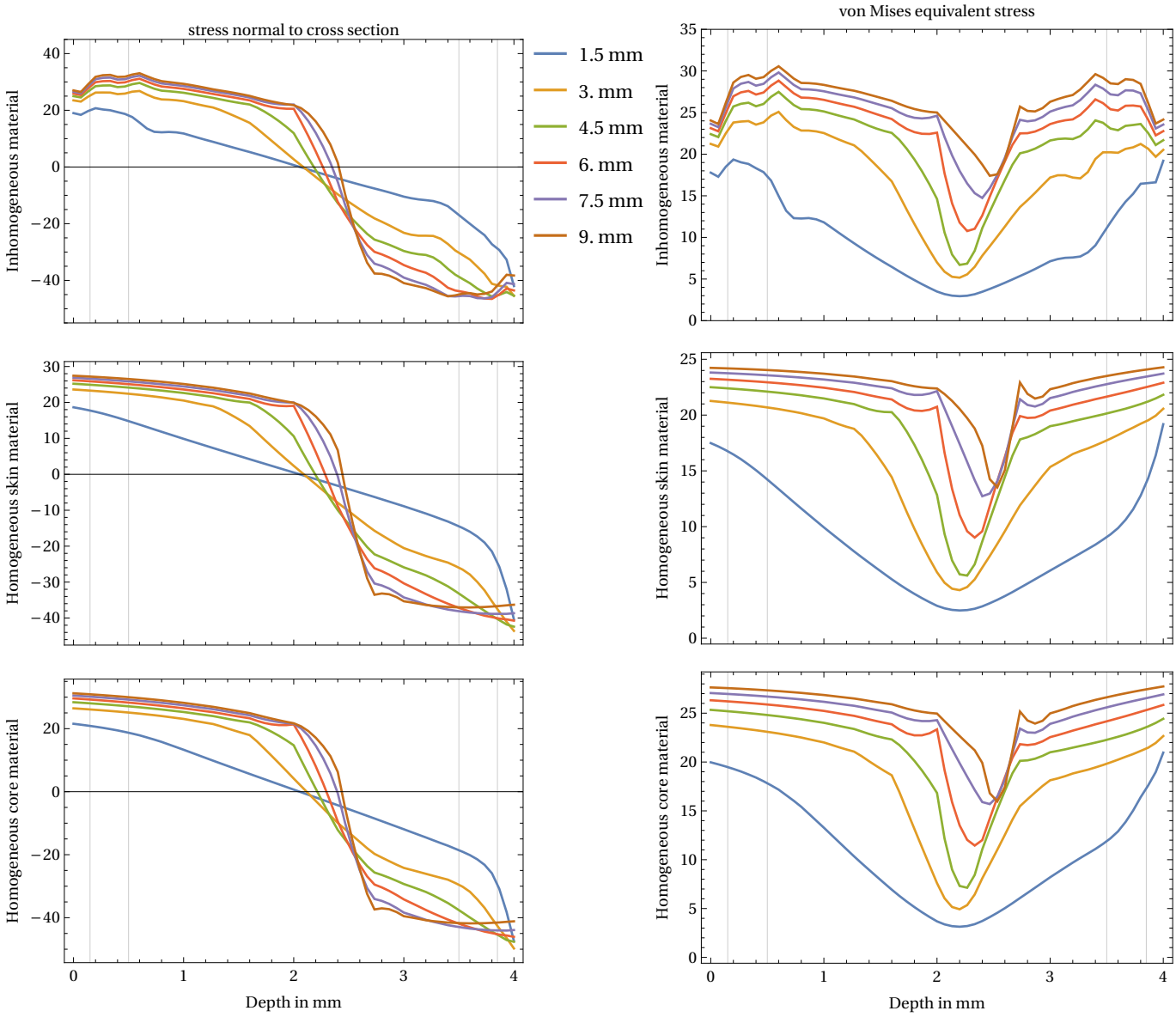

Figure 9: Left: Normal stress distribution (left column) and equivalent von Mises stress distribution (right column) through the bending sample near the bending load head at different load head displacements, shown for the inhomogeneous material (top row), the pure skin material (middle row). The vertical lines indicate the layer boundaries between the skin- shear- and core layer. Note the slight shift of the neutral axis due to the large deflection and the compressive loading at the bending load head at a depth of 4 mm. Most important, the upper right plot shows a significant drop of the equivalent von Mises stress near the skin.

the core, the yield stress has a global maximum of ≈ 26 MPa at ≈ 600 µm, while Young's modulus has a local minimum of ≈ 700 MPa at a depth of ≈ 0.7 µm, before a homogeneous property profile with average material parameters starts at ≈ 900 µm.

- The gradient of the material properties along the depth is rather strong. It easily overcompensates the linear strain-increase due to the bending deformation. Naturally, the effect is strongest after plastic deformations, where it can produce an equivalent von Mises stress drop from 30 MPa to 24 MPa in a depth from 0.5 mm to 0 mm, but it appears already in the elastic range. Young's modulus drops from ≈ 1000 MPa to ≈ 750 MPa at the surface over a thickness of only 0.1 mm. This is a strong gradient, which easily overcompensates the linear strain growth in the bending deformation.

References

A.K. Bledzki, P. Franciszczak, and A. Meljon. High performance hybrid pp and pla biocomposites reinforced with short man-made cellulose fibres and softwood flour. *Composites Part A: Applied Science and Manufacturing*, 74:132–139, 2015.

D. Drummer and S. Meister. Correlation of processing, inner structure, and part properties of injection moulded thin-wall parts on example of polyamide 66. *International Journal of Polymer Science*, 2014, 2014.

M. Fujiyama, T. Wakino, and Y. Kawasaki. Structure of skin layer in injection-molded polypropylene. *Journal of Applied Polymer Science*, 35(1):29–49, 1988.

R. Glüge, M. Weber, and A. Bertram. Comparison of spherical and cubical statistical volume elements with respect to convergence, anisotropy, and localization behavior. *Computational Material Science*, 63:91–104, 2012.

H. Hencky. Zur Theorie plastischer Deformationen und der hierdurch im Material hervorgerufenen Nachspannungen. *Zeitschrift für angewandte Mathematik und Mechanik*, 4:323–334, 1924.

J.-W. Housmans, M. Gahleitner, G.W.M. Peters, and H.E.H. Meijer. Structure-property relations in molded, nucleated isotactic polypropylene. *Polymer*, 50(10):2304–2319, 2009.

A. A. Ilyushin. Theory of plasticity at simple loading of the bodies exhibiting plastic hardening. *Rossíiskaya Akademiya Nauk (Prikl. Mat. Mekh.)*, 11:291, 1947.

M.R. Kamal, A.I. Isayev, and S.J. Liu. *Injection Molding: Technology and Fundamentals*. Polymer Processing Society, Progress in Polymer Processing. Hanser, 2009. ISBN 9783446416857.

S.S. Katti and M. Schultz. The microstructure of injection-molded semicrystalline polymers: A review. *Polymer Engineering & Science*, 22(16):1001–1017, 1982.

N. Mahmood, I. Kolesov, R. Glüge, H. Altenbach, R. Androsch, and M. Beiner. Influence of structure gradients in injection moldings of isotactic polypropylene on their mechanical properties. *Submitted for publication*, N.D.

W. Ramberg and W.R. Osgood. Description of stress-strain curves by three parameters. *Technical Note No. 902*, pages 1–28, 1943.

D.P. Russell and P.W.R. Beaumont. Structure and properties of injection-moulded nylon-6. *Journal of Materials Science*, 15(1): 197–207, Jan 1980.

D.W. van der Meer. Structure-property relationships in isotactic polypropylene, 6 2003.

Bianying Wen, Gang Wu, and Jian Yu. A flat polymeric gradient material: preparation, structure and property. *Polymer*, 45(10): 3359–3365, 2004.

R. Zheng, R.I. Tanner, and X.J. Fan. *Injection Molding: Integration of Theory and Modeling Methods*. Springer Berlin Heidelberg, 2011. ISBN 9783642212635.

TECHNISCHE MECHANIK
an open access journal

journal homepage: www.ovgu.de/techmech

Tech. Mech., Vol. 39, Is. 3, (2019), 261–281

Received: July 5, 2019
Accepted: September 18, 2019
Available online: October 1, 2019

Numerical Analysis of a Steam Turbine Rotor subjected to Thermo-Mechanical Cyclic Loads

J. Eisenträger[1]*, K. Naumenko[1], and H. Altenbach[1]

[1]Otto-von-Guericke-Universität, Institut für Mechanik, Universitätsplatz 2, 39106 Magdeburg, Germany

Abstract: The contribution at hand discusses the thermo-mechanical analysis of a steam turbine rotor, made of a heat-resistant steel. Thereby, the analysis accounts for the complicated geometry of a real steam turbine rotor, subjected to practical and complex thermo-mechanical boundary conditions. Various thermo-mechanical loading cycles are taken into account, including different starting procedures (cold and warm starts). Within the thermal analysis using the FE code ABAQUS, instationary steam temperatures as well as heat transfer coefficients are prescribed, and the resulting temperature field serves as input for the subsequent structural analysis. In order to describe the mechanical behavior of the heat-resistant steel, which exhibits significant rate-dependent inelasticity combined with hardening and softening phenomena, a robust nonlinear constitutive approach, the binary mixture model, is employed and implemented in ABAQUS in two different ways, i.e. using explicit as well as implicit methods for the time integration of the governing evolution equations. The numerical performance, the required computational effort, and the obtained accuracy of both integration methods are examined with reference to the thermo-mechanical analysis of a steam turbine rotor, as a typical practical example for the numerical analysis of a complex component. In addition, the obtained temperature, stress, and strain fields in the steam turbine rotor are discussed in detail, and the influence of the different starting procedures is examined closely.

Keywords: steam turbine rotor, mixture model, creep, numerical time integration, nonlinear constitutive modeling

1 Introduction

The current paper presents details on the thermo-mechanical analysis of a steam turbine rotor considering complex boundary conditions as well as the complicated geometry of this power plant component. In power plants, high temperatures prevail (around 873 K) such that the components operate under creep conditions, cf. Straub (1995); Fournier et al. (2011b); Pétry and Lindet (2009); Naumenko et al. (2011b); Götz (2004). Furthermore, the components are subjected to cyclic loads because of frequent start-ups and shut-downs of power plants, cf. Fournier et al. (2011a, 2005, 2009b, 2010); Röttger (1997). To withstand these conditions, heat-resistant steels with high chromium content offer excellent properties, e.g. high creep strength and good corrosion resistance, cf. Pétry and Lindet (2009); Götz (2004); Fournier et al. (2005); Berns and Theisen (2008); Giroux et al. (2010); Wang et al. (2013); Alsagabi et al. (2014); Kostenko et al. (2013), such that these alloys are commonly used for power plant components. Nevertheless, these steels tend to soften under creep-fatigue loads, which is based on microstructural processes such as the coarsening of subgrains and precipitates, cf. Straub (1995); Fournier et al. (2011b,a, 2009b, 2010); Röttger (1997); Giroux et al. (2010); Chilukuru et al. (2009); Agamennone et al. (2006); Orlová et al. (1998); Fournier et al. (2009a).

To the present, various constitutive models have been developed to simulate the mechanical behavior of high-chromium heat-resistant steels. Since a detailed survey of these approaches goes beyond the scope of this paper, we only provide a brief overview in the following. Overall, the constitutive models can be classified either as unified or non-unified approaches. The notion of unified model was introduced by Chaboche and Rousselier (1983). Thereby, only one time-dependent inelastic strain is taken into account. In contrast, non-unified models introduce separate variables to describe the instantaneous plastic strains and time-dependent inelastic deformation. Among the non-unified models, Wang et al. (2015) and Velay et al. (2006) present approaches for high-chromium heat-resistant steels. First, in Velay et al. (2006), the authors make use of internal variables to account for the cyclic behavior of a heat-resistant steel. In addition, Wang et al. (2015) adopt the Chaboche model, cf. Chaboche (1989), with three backstresses including both isotropic and kinematic hardening as well as a damage variable to simulate creep-fatigue behavior.

Moreover, the Chaboche model is frequently employed also in combination with unified constitutive models, cf. for example Saad (2012); Barrett et al. (2013); Zhang and Xuan (2017). All three chosen unified constitutive models are used to simulate the thermo-mechanical behavior of high-chromium heat-resistant steels, and 10 or even more temperature-dependent parameters are involved. Note that the actual number of parameters is at least twice as much since a minimum of two parameters is required to determine the (in the simplest case – linear) dependence on the temperature of each parameter. The large numbers of parameters frequently result from the introduction of several backstresses in order to account for nonlinear kinematic hardening. Consequently, the calibration effort increases and providing a physical background for all introduced parameters becomes a challenging task. For these reasons, we refrain from using the Chaboche model with several backstresses, and a unified mixture model is used to describe the thermo-mechanical behavior of the alloy X20CrMoV12-1, which is a typical heat-resistant steel with high chromium

* E-mail address: johanna.eisentraeger@ovgu.de
doi: 10.24352/UB.OVGU-2019-024

content.

Originally, the mixture model is based on materials science. Inelasticity combined with hardening and softening phenomena is simulated by applying an iso-strain concept to a binary mixture with a soft and hard constituent, cf. Straub (1995); Polcik (1998). The alloy under consideration is made of soft subgrains, which are separated by harder boundaries. Furthermore, the volume fraction of the hard constituent is closely related to the microstructure, for example the mean subgrain size. In order to model softening, we assume that the volume fraction of the hard constituent reduces during deformation until a saturation value is attained, cf. Naumenko et al. (2011a). Following the original formulation in materials science, the mixture models can be calibrated based on micrography, cf. e.g. Straub (1995); Polcik (1998); Barkar and Ågren (2005). However, if one would like to use results from macroscopic material tests for the calibration, the micromechanical mixture model must be transformed into a macroscopic approach. For this purpose, Naumenko et al. (2011a) introduce a backstress and a softening variable as internal variables. This macroscopic mixture model is calibrated in Eisenträger et al. (2018a) based on results from high temperature tensile tests and creep tests published in Eisenträger et al. (2017). After all, the mixture model describes the thermo-mechanical behavior of the considered heat-resistant steel over wide ranges of stresses and temperature ($100\,\mathrm{MPa} \leq \sigma \leq 700\,\mathrm{MPa}$, $673\,\mathrm{K} \leq T \leq 923\,\mathrm{K}$ with the Cauchy stress σ and the temperature T), while only 16 temperature-independent material parameters are involved, cf. Eisenträger (2018). To sum up, the mixture model features three main improvements in comparison to alternative approaches. Firstly, the number of material parameters is kept to a minimum since only two internal variables, i.e. a backstress and a softening variable, are taken into account. Secondly, it is possible to calibrate the model using only simple macroscopic tests, such that time-consuming microscopic observations are not necessary to identify all parameters. On top of that, one can apply the model to wide ranges of stresses and temperatures.

The current contribution aims at analyzing a steam turbine rotor with the calibrated mixture model. Note that the results of a similar analysis are presented in Eisenträger (2018). However, the analysis in Eisenträger (2018) focuses on a rotor with idealized geometry and simplified boundary conditions. To conduct this finite element analysis, the mixture model has been implemented into the FE code ABAQUS based on the implicit Euler method for time integration, cf. Eisenträger et al. (2018b). As a next step based on the previous publications, the contribution at hand demonstrates the applicability of the mixture model to a real power plant component with complicated geometry subjected to complex boundary conditions in step with actual practice. Note that several papers on finite element analysis of turbine rotors have already been published, cf. for example Jing et al. (2001, 2003); Nayebi et al. (2012); Sun et al. (2013); Wang et al. (2016); Zhu et al. (2017); Benaarbia et al. (2018); Wang and Liu (2018). Whereas the papers Nayebi et al. (2012); Benaarbia et al. (2018) refer to gas turbine rotors, the majority of publications focuses on steam turbine rotors. Furthermore, most authors make use of the Chaboche model to describe the multiaxial stress-strain behavior of the rotors. Axisymmetric FE models are frequently applied, and in many cases a preceding thermal analysis is conducted, which provides the temperature field as input for the subsequent structural analysis. Although these studies provide detailed insight into the stress and strain fields in rotors subjected to creep-fatigue loads, the influence of different starting procedures, such as varying initial temperatures in the rotor, has not been analyzed yet. Furthermore, in many cases, the given information on the applied boundary conditions could go more into detail. Consequently, the contribution at hand will address these problems by analyzing the influence of different starting procedures on the rotor as well as providing extensive and precise information on the applied boundary conditions. On top of that, we present a new implementation of the mixture model into the finite element method (FEM) based on explicit time integration of the evolution equations. This allows for a comparison of two different time integration methods (implicit and explicit Euler methods) with respect to their numerical performance, the involved computational effort, and the obtained accuracy. Although both time integration methods are well-known, most evaluations in literature focus on simple numerical examples, cf. Manzari and Prachathananukit (2001); Hu and Liu (2014). In contrast, the contribution at hand applies both methods to a complex problem taken from practice, whereby it is of particular interest to minimize computational times.

The current paper is composed of five sections, including this first introductory section. In Sect. 2, the governing equations of the binary mixture model are derived, and two internal variables, i.e. a backstress and a softening variable, are introduced. Section 3 focuses on the implementation of the mixture model into the FE code ABAQUS, based both on explicit and implicit time integration. The stress update algorithms as well as the consistent tangent operators are described for the two different time integration methods. Afterwards, details on the finite element analysis of the steam turbine rotor are given in Sect. 4. The section starts with a detailed description of the FE model, the meshes, as well as the boundary conditions. Subsequently, we examine the numerical performance of implicit and explicit time integration. We conclude the section by discussing the obtained temperature, stress, and strain fields in the rotor in detail. Finally, Sect. 5 gives a brief summary of the findings and identifies areas for further research.

Note that we make use both of direct tensor notation as well as matrix notation in this papers. While scalars are represented by italic letters, e.g. a, italic lowercase bold letters are used for vectors, e.g. $\boldsymbol{a} = a_i\,\boldsymbol{e}_i$. We symbolize tensors of second order by italic uppercase bold letters, e.g. $\boldsymbol{A} = A_{jk}\,\boldsymbol{e}_j \otimes \boldsymbol{e}_k$, and represent fourth-order tensors by upright uppercase double struck letters, for example $\mathbb{A} = A_{pqrs}\,\boldsymbol{e}_p \otimes \boldsymbol{e}_q \otimes \boldsymbol{e}_r \otimes \boldsymbol{e}_s$. Throughout the paper, Einstein's summation convention is applied, while Latin indices (e.g. i, j) take the values 1, 2, 3. Considering Cartesian coordinate systems with orthonormal bases, e.g. $\{\boldsymbol{e}_i\}$, we introduce the dyadic product:

$$\boldsymbol{a} \otimes \boldsymbol{b} = a_i\, b_j\, \boldsymbol{e}_i \otimes \boldsymbol{e}_j\,, \tag{1}$$

as well as the double scalar product between two tensors of second order and the analogous formulation for a fourth and a second-order tensor:

$$\boldsymbol{A} : \boldsymbol{B} = \left(A_{jk}\,\boldsymbol{e}_j \otimes \boldsymbol{e}_k\right) : \left(B_{no}\,\boldsymbol{e}_n \otimes \boldsymbol{e}_o\right) = A_{jk} B_{kj}\,, \tag{2}$$

$$\mathbb{A} : \boldsymbol{B} = \left(A_{jklm}\,\boldsymbol{e}_j \otimes \boldsymbol{e}_k \otimes \boldsymbol{e}_l \otimes \boldsymbol{e}_m\right) : \left(B_{no}\,\boldsymbol{e}_n \otimes \boldsymbol{e}_o\right) = A_{jklm} B_{ml} \boldsymbol{e}_j \otimes \boldsymbol{e}_k\,. \tag{3}$$

Here, it is worth noting that frequently, the double scalar product between two second-order tensors or a fourth and a second-order tensor is formulated in a different way in literature, cf. e.g. Itskov (2019). Switching to a vector-matrix notation, we represent vectors by upright lowercase sans serif bold letters, such as **a**. Matrices are symbolized by upright uppercase sans serif bold letters, e.g. **A**.

2 Constitutive Model

2.1 Binary Mixture Formulation

In the following, the governing equations of the binary mixture model are presented, based on the papers Naumenko et al. (2011a,b); Naumenko and Altenbach (2016); Eisenträger et al. (2018b). Since it is a *binary* mixture model, two constituents are taken into account: a "soft" and a "hard" part. While the soft constituent is related to regions with a low dislocation density, such as the interior of subgrains, the hard phase comprises the areas with a high dislocation density, i.e. the subgrain boundaries. Let us introduce the index $\square_k \forall\, k = \{\mathrm{s}, \mathrm{h}\}$ to distinguish the variables related to the different constituents.
Since the constitutive model will be utilized to simulate the thermo-mechanical behavior of practical components in power plants, the mixture model is formulated with respect to geometrically linear processes. Furthermore, due to this restriction, the involved computational effort decreases significantly. As already pointed out in Eisenträger et al. (2018b), in the case of applications involving high strains, various similar constitutive models for rate-dependent inelasticity under large deformations incorporating softening and hardening processes have been formulated, cf. Zhu et al. (2014); Shutov and Kreißig (2008). Because only geometrically linear processes are considered, we introduce the linear strain tensor $\boldsymbol{\varepsilon}$. The iso-strain assumption represents an important part of the mixture model, such that the strains in the two constituents are assumed to be equal:

$$\boldsymbol{\varepsilon} = \boldsymbol{\varepsilon}_\mathrm{h} = \boldsymbol{\varepsilon}_\mathrm{s}. \tag{4}$$

The iso-strain concept, which is also often referred to as "Voigt model" in literature, provides a robust and straightforward description of the material behavior. Nevertheless, one should point out that more sophisticated approaches are available as well in case if the constitutive model should be refined. For instance, one could use the continuum theory of mixtures, cf. Atkin and Craine (1976), to account for the interaction of the phases in the mixture. Furthermore, alternative models have been developed, which are neither founded upon the Voigt model nor the iso-stress (Reuss) concept. Instead, these approaches provide results that lie between the Voigt-Reuss bounds, for example the multiphase creep model presented in Raj et al. (1996).
The current constitutive model belongs to the group of unified material models, as introduced in Chaboche and Rousselier (1983). Here, the total inelastic strain $\boldsymbol{\varepsilon}_k^{\mathrm{in}}$ describes instantaneous plastic strains as well as creep strains, which are time-dependent. Note that the strains in both constituents are split additively into their elastic and inelastic portions, denoted by the superscripts $\square^{\mathrm{el}}$ and $\square^{\mathrm{in}}$, respectively:

$$\boldsymbol{\varepsilon} = \boldsymbol{\varepsilon}_k^{\mathrm{el}} + \boldsymbol{\varepsilon}_k^{\mathrm{in}}. \tag{5}$$

In addition, we make use of Hooke's law to describe the linear elastic behavior of isotropic materials:

$$\boldsymbol{\varepsilon}_k^{\mathrm{el}} = \frac{\sigma_{\mathrm{m}_k}}{3K}\boldsymbol{I} + \frac{\boldsymbol{\sigma}_k'}{2G} \tag{6}$$

or:

$$\boldsymbol{\sigma}_k = K\varepsilon_{\mathrm{V}_k}^{\mathrm{el}}\boldsymbol{I} + 2G\boldsymbol{\varepsilon}_k^{\mathrm{el}'}, \tag{7}$$

whereas the parameters G and K denote the shear and bulk modulus, respectively. Furthermore, we have introduced the Cauchy stress tensor $\boldsymbol{\sigma}$, the mean stress $\sigma_\mathrm{m} = \frac{1}{3}\mathrm{tr}\,(\boldsymbol{\sigma})$, and the volumetric strain $\varepsilon_\mathrm{V} = \mathrm{tr}\,(\boldsymbol{\varepsilon})$, which are computed based on the stress and strain tensors, applying the trace operator $\mathrm{tr}\,(\square)$. The deviatoric part of a second-order tensor is marked by the prime $\square' = \square - \frac{1}{3}\mathrm{tr}\,(\square)\,\boldsymbol{I}$, and the identity tensor of second order is represented by $\boldsymbol{I} = \boldsymbol{e}_i \otimes \boldsymbol{e}_i$. It is worth mentioning that the mixture model presumes an identical elastic behavior in both constituents, such that the same elastic material parameters are introduced for both constituents in Eqs. (6) and (7).
As a common choice to compute the total stress in a mixture model, a mixture rule based on the volume fractions η_k of the constituents is applied:

$$\boldsymbol{\sigma} = \eta_\mathrm{s}\boldsymbol{\sigma}_\mathrm{s} + \eta_\mathrm{h}\boldsymbol{\sigma}_\mathrm{h}, \tag{8}$$

while the following condition holds for the volume fractions due to conservation of mass:

$$\eta_\mathrm{s} + \eta_\mathrm{h} = 1 \qquad \forall \quad 0 \leq \eta_k \leq 1. \tag{9}$$

In order to simplify the constitutive model, let us only consider the volumetric parts of the stress and strain tensors in the following and apply the trace operator to Eqs. (4)–(6):

$$\varepsilon_\mathrm{V} = \varepsilon_{\mathrm{V}_\mathrm{h}} = \varepsilon_{\mathrm{V}_\mathrm{s}}, \tag{10}$$

$$\varepsilon_\mathrm{V} = \varepsilon_{\mathrm{V}_k}^{\mathrm{el}} + \varepsilon_{\mathrm{V}_k}^{\mathrm{in}}, \tag{11}$$

$$\varepsilon_{\mathrm{V}_k}^{\mathrm{el}} = \frac{\sigma_{\mathrm{m}_k}}{K}. \tag{12}$$

Within the classical theory of plastic deformations, it is commonly accepted to assume that the inelastic strains are not affected by the spherical part of the stresses, i.e. $\varepsilon_{\mathrm{V}_k}^{\mathrm{in}} = 0 \Rightarrow \boldsymbol{\varepsilon}_k^{\mathrm{in}} = \boldsymbol{\varepsilon}_k^{\mathrm{in}'}$. Considering this assumption and inserting Eqs. (11) and (12) into Eq. (10) yield:

$$\sigma_{\mathrm{m}} = \sigma_{\mathrm{m_h}} = \sigma_{\mathrm{m_s}} = K\varepsilon_{\mathrm{V}}. \tag{13}$$

Due to the equal bulk moduli in both constituents, Eq. (13) reveals that the mean stresses are equal in the entire mixture. Thus, one can restrict Eqs. (4) and (8) to the deviatoric parts of the stress and strain tensors:

$$\boldsymbol{\varepsilon}' = \boldsymbol{\varepsilon}_{\mathrm{h}}' = \boldsymbol{\varepsilon}_{\mathrm{s}}', \tag{14}$$

$$\boldsymbol{\sigma}' = \eta_{\mathrm{s}}\boldsymbol{\sigma}_{\mathrm{s}}' + \eta_{\mathrm{h}}\boldsymbol{\sigma}_{\mathrm{h}}'. \tag{15}$$

Next, we determine the stress deviators $\boldsymbol{\sigma}_k'$ for both constituents based on Eq. (6). The obtained expressions for the deviatoric stresses are inserted into Eq. (15), which yields the constitutive law for the elastic behavior of the entire mixture:

$$\boldsymbol{\varepsilon} = \frac{\sigma_{\mathrm{m}}}{3K}\boldsymbol{I} + \frac{\boldsymbol{\sigma}'}{2G} + \boldsymbol{\varepsilon}^{\mathrm{in}}, \tag{16}$$

while $\boldsymbol{\varepsilon}^{\mathrm{in}}$ represents the inelastic strain of the mixture:

$$\boldsymbol{\varepsilon}^{\mathrm{in}} \equiv (1-\eta_{\mathrm{h}})\,\boldsymbol{\varepsilon}_{\mathrm{s}}^{\mathrm{in}} + \eta_{\mathrm{h}}\boldsymbol{\varepsilon}_{\mathrm{h}}^{\mathrm{in}}. \tag{17}$$

In addition, evolution equations for the inelastic strains $\dot{\boldsymbol{\varepsilon}}_k^{\mathrm{in}}$ are formulated, following Naumenko et al. (2011a); Naumenko and Altenbach (2016):

$$\dot{\boldsymbol{\varepsilon}}_{\mathrm{s}}^{\mathrm{in}} = \frac{3}{2}\dot{\varepsilon}_{\mathrm{vM_s}}^{\mathrm{in}}\frac{\boldsymbol{\sigma}_{\mathrm{s}}'}{\sigma_{\mathrm{vM_s}}}, \tag{18}$$

$$\dot{\boldsymbol{\varepsilon}}_{\mathrm{h}}^{\mathrm{in}} = \frac{3}{2}\dot{\varepsilon}_{\mathrm{vM}}^{\mathrm{in}}\frac{\boldsymbol{\sigma}_{\mathrm{h}}' - \boldsymbol{\sigma}'}{\sigma_{\mathrm{vM}_\star}}. \tag{19}$$

Note that we have introduced the von Mises equivalent inelastic strain rates $\dot{\varepsilon}_{\mathrm{vM_s}}^{\mathrm{in}}$ and $\dot{\varepsilon}_{\mathrm{vM}}^{\mathrm{in}}$ for the soft part and with respect to the entire mixture, respectively. Furthermore, the variable $\sigma_{\mathrm{vM_s}}$ denotes the von Mises equivalent stress in the soft constituent, and $\sigma_{\mathrm{vM}_\star}$ is the von Mises equivalent saturation stress:

$$\dot{\varepsilon}_{\mathrm{vM_s}}^{\mathrm{in}} = \sqrt{\frac{2}{3}\dot{\boldsymbol{\varepsilon}}_{\mathrm{s}}^{\mathrm{in}} : \dot{\boldsymbol{\varepsilon}}_{\mathrm{s}}^{\mathrm{in}}}, \tag{20}$$

$$\dot{\varepsilon}_{\mathrm{vM}}^{\mathrm{in}} = \sqrt{\frac{2}{3}\dot{\boldsymbol{\varepsilon}}^{\mathrm{in}} : \dot{\boldsymbol{\varepsilon}}^{\mathrm{in}}}, \tag{21}$$

$$\sigma_{\mathrm{vM_s}} = \sqrt{\frac{3}{2}\boldsymbol{\sigma}_{\mathrm{s}}' : \boldsymbol{\sigma}_{\mathrm{s}}'}, \tag{22}$$

$$\sigma_{\mathrm{vM}_\star} = \sqrt{\frac{3}{2}\left(\boldsymbol{\sigma}_{\mathrm{h}_\star}' - \boldsymbol{\sigma}'\right) : \left(\boldsymbol{\sigma}_{\mathrm{h}_\star}' - \boldsymbol{\sigma}'\right)}. \tag{23}$$

In above expressions, the term $\boldsymbol{\sigma}_{\mathrm{h}_\star}'$ stands for the saturation stress in the hard constituent. Additionally, the subsequent evolution equation is utilized for the equivalent inelastic strain rate in the soft constituent $\dot{\varepsilon}_{\mathrm{vM_s}}^{\mathrm{in}}$:

$$\dot{\varepsilon}_{\mathrm{vM_s}}^{\mathrm{in}} = f_\sigma\left(\sigma_{\mathrm{vM_s}}\right) f_T\left(T\right). \tag{24}$$

Moreover, we formulate an evolution equation for the volume fraction of the hard constituent:

$$\dot{\eta}_{\mathrm{h}} = f_\eta\left(\boldsymbol{\sigma}_{\mathrm{h}}, \dot{\boldsymbol{\varepsilon}}_{\mathrm{h}}^{\mathrm{in}}, T\right). \tag{25}$$

Note that the volume fraction of the soft constituent can be computed by combining Eqs. (9) and (25). The one-dimensional mixture model is visualized with rheological elements in Fig. 1, while we presume constant volume fractions in both constituents.

2.2 Formulation with Internal Variables

Since the mixture model has been described in the previous section in close reference to the microstructure, detailed microstructural observations would be required for the calibration of the model. Though, for the discussed application and the considered heat-resistant steel, we frequently only have access to the results of macroscopic material tests, such as high temperature tensile tests or creep tests. Therefore, we introduce two internal variables, i.e. a backstress tensor $\boldsymbol{\beta}$ and a dimensionless scalar softening

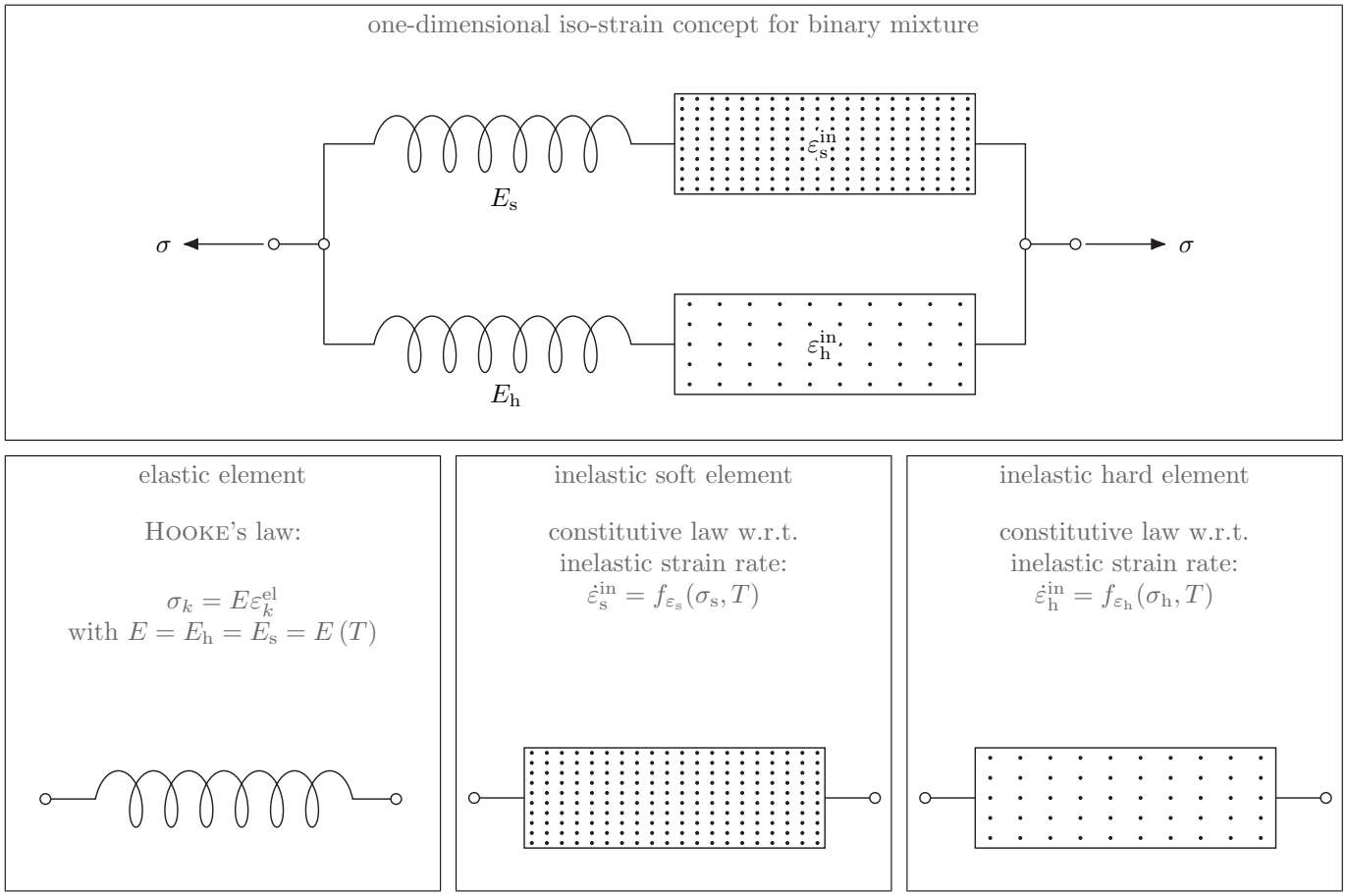

Fig. 1: Iso-strain concept for a binary mixture with constant volume fractions of constituents, cf. Eisenträger et al. (2017)

variable Γ. The backstress is employed to describe kinematic hardening. The tensorial variable as well as the corresponding equivalent von Mises variable β_vM are computed according to the following equations:

$$\boldsymbol{\beta} = \frac{\eta_{\mathrm{h}_0}}{1-\eta_{\mathrm{h}_0}}\left(\boldsymbol{\sigma}'_\mathrm{h} - \boldsymbol{\sigma}'\right) \qquad \forall \quad 0 < \eta_{\mathrm{h}_0} < 1, \tag{26}$$

$$\beta_\mathrm{vM} = \sqrt{\frac{3}{2}\boldsymbol{\beta}:\boldsymbol{\beta}} \qquad \forall \quad 0 \leq \beta_\mathrm{vM} \leq \beta_{\mathrm{vM}_\star}, \tag{27}$$

whereas the corresponding saturation values are marked with an asterisk:

$$\boldsymbol{\beta}_\star = \frac{\eta_{\mathrm{h}_0}}{1-\eta_{\mathrm{h}_0}}\left(\boldsymbol{\sigma}'_{\mathrm{h}_\star} - \boldsymbol{\sigma}'\right), \tag{28}$$

$$\beta_{\mathrm{vM}_\star} = \sqrt{\frac{3}{2}\boldsymbol{\beta}_\star:\boldsymbol{\beta}_\star}. \tag{29}$$

In Eqs. (26) and (28), we make use of the parameter η_{h_0}, denoting the volume fraction of the hard constituent in the initial state: $\eta_{\mathrm{h}_0} = \eta_\mathrm{h}\,(t=0)$. Moreover, it is demonstrated in Naumenko et al. (2011a) that the tensor $\boldsymbol{\beta}$ can be interpreted as a backstress similar to the well-known Armstrong-Frederick-type backstress, cf. Armstrong and Frederick (1966). To describe softening processes, the scalar variable Γ with the corresponding saturation value $\Gamma_\star$ is introduced in the following:

$$\Gamma = \frac{\eta_\mathrm{h}}{1-\eta_\mathrm{h}}\frac{1-\eta_{\mathrm{h}_0}}{\eta_{\mathrm{h}_0}} \qquad \forall \quad \Gamma_\star \leq \Gamma \leq 1, \tag{30}$$

$$\Gamma_\star = \frac{\eta_{\mathrm{h}\star}}{1-\eta_{\mathrm{h}\star}}\frac{1-\eta_{\mathrm{h}_0}}{\eta_{\mathrm{h}_0}} \qquad \forall \quad 0 < \eta_{\mathrm{h}\star} < 1. \tag{31}$$

Note that the new variable $\eta_{\mathrm{h}\star}$ represents the saturation value for the volume fraction with respect to the hard constituent. In the next step, we compute the stresses and inelastic strain rates of the individual constituents based on the new internal variables by deploying the definitions in Eqs. (26)–(31) as well as the Eqs. (15), (18), (19), and (24):

$$\boldsymbol{\sigma}'_\mathrm{h} = \boldsymbol{\sigma}' + \frac{1-\eta_{\mathrm{h}_0}}{\eta_{\mathrm{h}_0}}\boldsymbol{\beta}, \tag{32}$$

$$\boldsymbol{\sigma}'_\mathrm{s} = \tilde{\boldsymbol{\sigma}}', \tag{33}$$

$$\dot{\boldsymbol{\varepsilon}}_{\mathrm{h}}^{\mathrm{in}} = \frac{3}{2}\dot{\varepsilon}_{\mathrm{vM}}^{\mathrm{in}}\frac{\boldsymbol{\beta}}{\beta_{\mathrm{vM}_\star}}, \tag{34}$$

$$\dot{\boldsymbol{\varepsilon}}_{\mathrm{s}}^{\mathrm{in}} = \frac{3}{2}f_\sigma\left(\tilde{\sigma}_{\mathrm{vM}}\right)f_T\left(T\right)\frac{\tilde{\boldsymbol{\sigma}}'}{\tilde{\sigma}_{\mathrm{vM}}}, \tag{35}$$

while the effective stress $\tilde{\boldsymbol{\sigma}}'$ and the corresponding von Mises variable $\tilde{\sigma}_{\mathrm{vM}}$ have been introduced:

$$\tilde{\boldsymbol{\sigma}}' = \boldsymbol{\sigma}' - \Gamma\boldsymbol{\beta}, \tag{36}$$

$$\tilde{\sigma}_{\mathrm{vM}} = \sqrt{\frac{3}{2}\tilde{\boldsymbol{\sigma}}' : \tilde{\boldsymbol{\sigma}}'}. \tag{37}$$

Afterwards, Eq. (16) is differentiated with respect to the time t:

$$\dot{\boldsymbol{\varepsilon}}^{\mathrm{in}} = \dot{\boldsymbol{\varepsilon}} - \frac{\partial}{\partial t}\left(\frac{\sigma_{\mathrm{m}}}{3K}\boldsymbol{I} + \frac{\boldsymbol{\sigma}'}{2G}\right). \tag{38}$$

By taking into account Eq. (6), we transform Eq. (5) with respect to the individual constituents in a similar way:

$$\dot{\boldsymbol{\varepsilon}} = \frac{\partial}{\partial t}\left(\frac{\sigma_{\mathrm{m}}}{3K}\boldsymbol{I} + \frac{\boldsymbol{\sigma}_k'}{2G}\right) + \dot{\boldsymbol{\varepsilon}}_k^{\mathrm{in}}. \tag{39}$$

Finally, above equation is referred to the soft constituent and inserted into Eq. (38). In addition, one replaces the stress deviator $\boldsymbol{\sigma}_{\mathrm{s}}'$ and the inelastic strain rate tensor $\dot{\boldsymbol{\varepsilon}}_{\mathrm{s}}^{\mathrm{in}}$ by deploying Eqs. (33) and (35). Then, the equations are transformed until we obtain an evolution equation for the inelastic strain $\boldsymbol{\varepsilon}^{\mathrm{in}}$ in the mixture:

$$\dot{\boldsymbol{\varepsilon}}^{\mathrm{in}} = \frac{3}{2}f_\sigma\left(\tilde{\sigma}_{\mathrm{vM}}\right)f_T\left(T\right)\frac{\tilde{\boldsymbol{\sigma}}'}{\tilde{\sigma}_{\mathrm{vM}}} - \frac{\partial}{\partial t}\left(\frac{\Gamma\boldsymbol{\beta}}{2G}\right). \tag{40}$$

Note that the last term exerts only a slight influence on the inelastic strain rate at the beginning of inelastic deformation such that it is neglected in the remainder, as also already done in Naumenko et al. (2011a); Eisenträger et al. (2017). Thus, Eq. (40) is simplified as follows:

$$\dot{\boldsymbol{\varepsilon}}^{\mathrm{in}} = \frac{3}{2}f_\sigma\left(\tilde{\sigma}_{\mathrm{vM}}\right)f_T\left(T\right)\frac{\tilde{\boldsymbol{\sigma}}'}{\tilde{\sigma}_{\mathrm{vM}}}. \tag{41}$$

Finally, the equations for the hard constituent are transformed in an analogous way: First, we evaluate Eq. (39) with respect to the hard constituent and insert the resulting terms into Eq. (38). Thereby, the deviatoric stress $\boldsymbol{\sigma}_{\mathrm{h}}'$ and the inelastic strain rate $\dot{\boldsymbol{\varepsilon}}_{\mathrm{h}}^{\mathrm{in}}$ are substituted using Eqs. (32) and (34), which results in an evolution equation for the backstress $\boldsymbol{\beta}$:

$$\dot{\boldsymbol{\beta}} = \frac{1}{G}\frac{\partial G}{\partial T}\dot{T}\boldsymbol{\beta} + 2G\frac{\eta_{\mathrm{h}_0}}{1-\eta_{\mathrm{h}_0}}\left(\dot{\boldsymbol{\varepsilon}}^{\mathrm{in}} - \frac{3}{2}\dot{\varepsilon}_{\mathrm{vM}}^{\mathrm{in}}\frac{\boldsymbol{\beta}}{\beta_{\mathrm{vM}_\star}}\right). \tag{42}$$

Furthermore, we adopt the evolution equation for the softening variable from Naumenko et al. (2011a):

$$\dot{\Gamma} = C\left[\Gamma_\star\left(\sigma_{\mathrm{vM}}\right) - \Gamma\right]\dot{\varepsilon}_{\mathrm{vM}}^{\mathrm{in}}. \tag{43}$$

Since the volume fraction of the hard constituent is replaced by Γ, see also Eq. (30), Eq. (43) expresses the continuous decline of the softening variable towards its saturation value $\Gamma_\star$ as the inelastic deformation increases. In this way, we can describe the macroscopic softening of heat-resistant steels, which is based predominantly on the growth of subgrains. Note that this evolution equation is restricted to proportional loading, and in case of non-proportional loading, one should resort to refined approaches, as the model proposed in Silbermann et al. (2014).

The presented mixture model has been calibrated in Eisenträger et al. (2018a); Eisenträger (2018) based on the results of macroscopic material tests on the heat-resistant steel X20CrMoV12-1, as presented in Eisenträger et al. (2017). The following stress and temperature response functions have been found to describe the mechanical behavior of the heat-resistant alloy in a robust way:

$$E\left(T\right) = C_1 + C_2T^3, \tag{44}$$

$$G\left(T\right) = C_3 + C_4T^3, \tag{45}$$

$$f_T\left(T\right) = \exp\left(-\frac{Q}{\mathrm{R}T}\right), \tag{46}$$

$$f_\sigma\left(\tilde{\sigma}_{\mathrm{vM}}\right) = a_\sigma\sinh\left(\frac{\tilde{\sigma}_{\mathrm{vM}}}{b_\sigma}\right)\left[1 + \left(\frac{\tilde{\sigma}_{\mathrm{vM}}}{c_\sigma}\right)^{m_\sigma}\right], \tag{47}$$

$$\beta_{\mathrm{vM}_\star}\left(\sigma_{\mathrm{vM}}\right) = \frac{2a_\beta}{1+\exp\left(-b_\beta\sigma_{\mathrm{vM}}\right)} - a_\beta, \tag{48}$$

Tab. 1: Used constants and identified material parameters in the unified mixture model, cf. Eisenträger (2018)

variable	value	unit	meaning	equation
C_1	2.23×10^5	MPa	parameters in the temperature response function for YOUNG's modulus	(44)
C_2	-1.64×10^{-4}	MPa K^{-3}		
C_3	82.6×10^3	MPa	parameters in the temperature response function for shear modulus	(45)
C_4	-2.87×10^{-5}	MPa K^{-3}		
Q	540.6×10^3	J mol^{-1}	activation energy in the temperature response functions for the inelastic strain rate	(46)
R	8.317	J (mol K)$^{-1}$	universal gas constant in the temperature response functions for the inelastic strain rate	(46)
a_σ	1.54×10^{24}	s^{-1}	parameters in the stress response function for the inelastic strain rate	(47)
b_σ	25.8	MPa		
c_σ	483.6	MPa		
m_σ	35.7	–		
η_{h_0}	0.17	–	reference value for the volume fraction of the hard constituent	(42)
a_β	80.0	MPa	maximum value for the saturation backstress	(48)
b_β	2.70×10^{-2}	MPa^{-1}	parameter in the evolution function for the saturation backstress	(48)
C	5.0	–	parameter in the evolution equation for the softening variable	(43)
a_Γ	1.0	–	parameters in the stress response function for the saturation softening variable	(49)
b_Γ	1.30×10^{-2}	MPa^{-1}		
c_Γ	520.0	MPa		

$$\Gamma_\star\left(\sigma_{\mathrm{vM}}\right) = \frac{a_\Gamma}{1 + \exp\left[-b_\Gamma\left(\sigma_{\mathrm{vM}} - c_\Gamma\right)\right]}. \tag{49}$$

Note that a temperature response function for the YOUNG's modulus has been formulated since this material parameter is straightforward to determine based on high temperature tensile tests. The bulk modulus K is obtained based on the YOUNG's and shear modulus as follows:

$$K = \frac{GE}{3\left(3G - E\right)}. \tag{50}$$

Table 1 provides an overview of all constants and identified parameters. After all, the mixture model involves a total of 16 temperature-independent parameters, which is a relatively low number if we consider the remarkably wide ranges of applicability with respect to temperatures ($673\,\mathrm{K} \leq T \leq 923\,\mathrm{K}$) and stresses ($100\,\mathrm{MPa} \leq \sigma_{\mathrm{vM}} \leq 700\,\mathrm{MPa}$), as discussed in Eisenträger (2018). To provide a basis for the derivations in the following sections, let us recall the governing equations of the mixture model:

- HOOKE's law for the linear elastic behavior of the mixture, assuming isotropy

$$\boldsymbol{\sigma} = K\varepsilon_{\mathrm{V}}^{\mathrm{el}}\boldsymbol{I} + 2G\boldsymbol{\varepsilon}^{\mathrm{el}'}, \tag{51}$$

- the split of strains into the elastic and inelastic parts

$$\boldsymbol{\varepsilon} = \boldsymbol{\varepsilon}^{\mathrm{el}} + \boldsymbol{\varepsilon}^{\mathrm{in}}, \tag{52}$$

- the evolution equation for the inelastic strain, cf. Eq. (41),
- the evolution equation for the backstress, cf. Eq. (42),
- the evolution equation for the softening variable, cf. Eq. (43).

In addition, initial conditions (ICs) must be taken into account. In order to simulate the behavior of an undeformed material, we assume the following ICs:

$$\boldsymbol{\sigma}\left(t=0\right) = \mathbf{0}, \qquad \boldsymbol{\beta}\left(t=0\right) = \mathbf{0}, \qquad \Gamma\left(t=0\right) = 1. \tag{53}$$

Since the presented mixture model will be used in partly coupled thermo-mechanical analyses, it is of particular importance to check for thermodynamical consistency. In Eisenträger (2018), a proof for the thermodynamical consistency of the mixture model in the present form is given based on the CLAUSIUS-PLANCK inequality. Note that the proof of thermodynamical consistency is based on the assumption of stationary temperatures, which is deemed adequate considering the major applications, i.e. during the start-ups and shut-downs of power plants, temperatures change relatively slowly. The interested reader is referred to Eisenträger (2018), where further details on the derivation can be found.

3 Numerical Implementation

The analysis of a real steam turbine rotor featuring complex geometry and boundary conditions represents the overall aim of this contribution. Due to the complexity of the problem, the finite element method (FEM) is utilized as an established and versatile computational approach. Therefore, the current section provides details on the integration of the calibrated mixture model into the FEM.

In the previous section, it has been shown that the mixture model results in a system of five governing equations, i.e. Eqs. (51) and (52) as well as three evolution equations with respect to the inelastic strain $\boldsymbol{\varepsilon}^{\mathrm{in}}$, the backstress $\boldsymbol{\beta}$, and the softening variable Γ, cf. Eqs. (41)–(43). Note that displacement increments are usually prescribed in finite element calculations. The strains are straightforward to compute using the first derivatives of the displacement, while the stresses and internal variables are obtained based on the constitutive model — a process which is frequently referred to as stress update algorithm, cf. Belytschko et al. (2000). For this purpose, an evolution equation for the stress tensor $\boldsymbol{\sigma}$ is derived in the following by differentiating Eq. (16) with respect to time:

$$\dot{\boldsymbol{\sigma}} = K\dot{\varepsilon}_{\mathrm{V}}\boldsymbol{I} + 2G\left(\dot{\boldsymbol{\varepsilon}} - \dot{\boldsymbol{\varepsilon}}^{\mathrm{in}}\right) + \left(\frac{\partial K}{\partial T} + \frac{2}{3}\frac{\partial G}{\partial T}\right)\dot{T}\frac{\sigma_{\mathrm{m}}}{K}\boldsymbol{I} + \frac{1}{G}\frac{\partial G}{\partial T}\dot{T}\boldsymbol{\sigma}', \tag{54}$$

whereby the inelastic strain rate $\dot{\boldsymbol{\varepsilon}}^{\mathrm{in}}$ is computed by Eq. (41), involving the two internal variables. Next, we have to integrate the obtained system of evolution equations, i.e. Eqs. (42), (43), and (54), with respect to time, while displacement or strain increments are prescribed. To realize the time integration numerically, we can resort to two general classes of computational models for time integration: explicit and implicit approaches. In order to predict an unknown equilibrium state with respect to the time step t_{n+1}, explicit methods only require quantities from the previous time step t_n, cf. Wriggers (2008), which simplifies the implementation of explicit methods significantly. However, this type of time integration method exhibits only conditional stability, such that the stability is dependent on the selected time step size, cf. Luccioni et al. (2001).

Alternatively, implicit time integration methods can be used. Here, the variables for the new equilibrium state at the time step t_{n+1} are estimated by using not only the previous time steps, but taking into account the current and future time steps as well. This procedure usually results in the solution of a nonlinear system of equations at every time step, cf. Wriggers (2008), which increases the involved computational effort. Furthermore, the application of implicit time integration methods to nonlinear material models can be cumbersome. However, implicit methods feature unconditional stability, i.e. the stability is independent from the increment size, which represents a major advantage in comparison to explicit methods.

Since the previous considerations clearly show that both explicit and implicit methods feature different benefits and drawbacks, the contribution at hand discusses the implementation of the mixture model into the FEM based on both types of time integration methods. Note that Sect. 4.2 provides a detailed discussion of the accuracy and computational costs of both integration methods with respect to the finite element analysis of the steam turbine rotor. As a well-known approach both for implicit and explicit methods, we will make use of the backward and forward Euler methods for the numerical integration of the evolution equations. Due to their straightforward formulation, these methods are frequently employed to implement nonlinear constitutive models, cf. Hartmann and Haupt (1993); Hartmann et al. (1997); Kobayashi et al. (2003); Benaarbia et al. (2018).

In order to illustrate the general difference in explicit and implicit time integration, suppose that we would like to find a solution for the ordinary differential equation $\dot{\boldsymbol{Z}} = \boldsymbol{F}(\boldsymbol{Z}, t)$ with respect to the unknown variable $\boldsymbol{Z}$. The time increment Δt is prescribed, and the variable $\boldsymbol{Z}_n$ at the time step t_n is known. As a typical implicit time integration approach, the backward Euler method provides the solution at the time step $t_{n+1} = t_n + \Delta t$ as follows, cf. Simo and Hughes (1998); Belytschko et al. (2000); Zienkiewicz and Taylor (2005); Wriggers (2008):

$$\boldsymbol{Z}_{n+1} = \boldsymbol{Z}_n + \Delta t\, \boldsymbol{F}(\boldsymbol{Z}_{n+1}, t_{n+1})\,. \tag{55}$$

In contrast, if we apply the forward Euler method as an explicit method to the same problem, the solution requires only variables from the previous time step t_n, cf. Simo and Hughes (1998); Belytschko et al. (2000); Zienkiewicz and Taylor (2005); Wriggers (2008):

$$\boldsymbol{Z}_{n+1} = \boldsymbol{Z}_n + \Delta t\, \boldsymbol{F}(\boldsymbol{Z}_n, t_n)\,. \tag{56}$$

In the following, both methods are applied to the mixture model. The implicit time integration, including the stress update algorithm and the consistent tangent operator, is presented in Sect. 3.1, while Sect. 3.2 focuses on the explicit time integration. Whereas the derivations in Sect. 3.1 are based on Eisenträger et al. (2018b), the implementation of the mixture model using an explicit integration method has not been presented in literature yet.

3.1 Implicit Time Integration

3.1.1 Stress Update Algorithm

To update the stresses and internal variables based on the implicit Euler method, let us apply Eq. (55) to the governing equations of the mixture model. Using the backward Euler method, the strains, the temperature, the stress, and the internal variables are updated as follows, cf. Belytschko et al. (2000):

$$\square_{n+1} = \square_n + \Delta\, \square_{n+1} \qquad \forall \quad \square = \left\{\boldsymbol{\varepsilon}, \boldsymbol{\varepsilon}^{\mathrm{in}}, T, \boldsymbol{\sigma}, \boldsymbol{\beta}, \Gamma\right\}. \tag{57}$$

Note that in the remainder of this section all entities refer to the time step t_{n+1}, if it is not stated otherwise. Additionally, the evolution equations, cf. Eqs. (41)–(43), are transformed based on the backward Euler method:

$$\Delta\boldsymbol{\varepsilon}^{\mathrm{in}}_{n+1} = \frac{3}{2}\Delta t\, f_\sigma\left(\tilde{\sigma}_{\mathrm{vM}}\right) f_T\left(T\right) \frac{\tilde{\boldsymbol{\sigma}}'}{\tilde{\sigma}_{\mathrm{vM}}}, \tag{58}$$

$$\Delta\boldsymbol{\beta}_{n+1} = \frac{1}{G}\frac{\mathrm{d}G}{\mathrm{d}T}\Delta T\boldsymbol{\beta} + 2G\frac{\eta_{\mathrm{h}_0}}{1-\eta_{\mathrm{h}_0}}\left(\Delta\boldsymbol{\varepsilon}^{\mathrm{in}} - \frac{3}{2}\Delta\varepsilon^{\mathrm{in}}_{\mathrm{vM}}\frac{\boldsymbol{\beta}}{\beta_{\mathrm{vM}_\star}}\right), \tag{59}$$

$$\Delta\Gamma_{n+1} = C_\Gamma\left[\Gamma_\star\left(\sigma_{\mathrm{vM}}\right) - \Gamma\right]\Delta\varepsilon^{\mathrm{in}}_{\mathrm{vM}}. \tag{60}$$

Furthermore, we deploy Hooke's law by reformulating Eq. (51):

$$\boldsymbol{\sigma}_{n+1} = \mathbb{C}_{n+1} : \boldsymbol{\varepsilon}^{\mathrm{el}}_{n+1}, \tag{61}$$

whereby the elastic stiffness tensor $\mathbb{C}$ and the fourth-order identity tensor $\mathbb{I}$ are introduced:

$$\mathbb{C} = \frac{1}{3}\left(3K - 2G\right)\boldsymbol{I}\otimes\boldsymbol{I} + 2G\mathbb{I}, \tag{62}$$

$$\mathbb{I} = \frac{1}{2}\left(\boldsymbol{e}_i\otimes\boldsymbol{e}_j\otimes\boldsymbol{e}_j\otimes\boldsymbol{e}_i + \boldsymbol{e}_i\otimes\boldsymbol{e}_j\otimes\boldsymbol{e}_i\otimes\boldsymbol{e}_j\right). \tag{63}$$

Next, we substitute the elastic strain in Eq. (61) by making use of the additive split of strains, cf. Eq. (52), under consideration of Eq. (57):

$$\boldsymbol{\sigma}_{n+1} = \mathbb{C}_{n+1} : \left(\boldsymbol{\varepsilon}_n + \Delta\boldsymbol{\varepsilon}_{n+1} - \boldsymbol{\varepsilon}^{\mathrm{in}}_n - \Delta\boldsymbol{\varepsilon}^{\mathrm{in}}_{n+1}\right). \tag{64}$$

Now, a nonlinear system of equations, comprising Eqs. (64) and (57)–(60), has been derived and must be solved. Since the solution of this system of equations is performed within a finite element code, we switch from tensor notation to the matrix notation according to Voigt in the following. For this purpose, the stress vectors $\mathbf{s}$ and $\tilde{\mathbf{s}}$, the backstress vector $\mathbf{b}$ and the strain vector $\mathbf{e}$ are introduced:

$$\mathbf{s} = \begin{bmatrix}\sigma_{11} & \sigma_{22} & \sigma_{33} & \sigma_{12} & \sigma_{13} & \sigma_{23}\end{bmatrix}^{\mathrm{T}}, \tag{65}$$

$$\tilde{\mathbf{s}} = \begin{bmatrix}\tilde{\sigma}_{11} & \tilde{\sigma}_{22} & \tilde{\sigma}_{33} & \tilde{\sigma}_{12} & \tilde{\sigma}_{13} & \tilde{\sigma}_{23}\end{bmatrix}^{\mathrm{T}}, \tag{66}$$

$$\mathbf{b} = \begin{bmatrix}\beta_{11} & \beta_{22} & \beta_{33} & \beta_{12} & \beta_{13} & \beta_{23}\end{bmatrix}^{\mathrm{T}}, \tag{67}$$

$$\mathbf{e} = \begin{bmatrix}\varepsilon_{11} & \varepsilon_{22} & \varepsilon_{33} & 2\varepsilon_{12} & 2\varepsilon_{13} & 2\varepsilon_{23}\end{bmatrix}^{\mathrm{T}}. \tag{68}$$

The vectors for the stress deviators, the inelastic or elastic strains, and other incremental entities are formulated and named in an analogous manner. To solve the nonlinear system of equations with the Newton-Raphson method, the equations are reformulated as follows:

$$\mathbf{r}^i_\sigma = \mathbf{0}, \tag{69}$$

$$\mathbf{r}^i_\beta = \mathbf{0}, \tag{70}$$

$$r^i_\Gamma = 0, \tag{71}$$

while introducing the residual quantities $\mathbf{r}^i_\sigma$, $\mathbf{r}^i_\beta$, and r^i_Γ

$$\mathbf{r}^i_\sigma = -\mathbf{e}_{n+1} + \mathbf{e}^{\mathrm{in}}_n + \mathbf{C}^{-1}_{n+1}\mathbf{s}^i_{n+1} + \Delta\mathbf{e}^{\mathrm{in}^i}_{n+1}, \tag{72}$$

$$\mathbf{r}^i_\beta = -\mathbf{b}_n + \mathbf{b}^i_{n+1} - \Delta\mathbf{b}^i_{n+1}, \tag{73}$$

$$r^i_\Gamma = -\Gamma_n + \Gamma^i_{n+1} - \Delta\Gamma^i_{n+1}. \tag{74}$$

Note that $\square^i$ denotes the iteration index. Furthermore, the elasticity stiffness matrix $\mathbf{C}$ and its inverse $\mathbf{C}^{-1}$ in Voigt notation have been introduced. Within the application of the Newton-Raphson method, Eqs. (69)–(71) are linearized, cf. Wriggers (2008):

$$\mathbf{A}^i_{n+1}\Delta\mathbf{p}^{i+1}_{n+1} = -\mathbf{r}^i_{n+1}, \tag{75}$$

whereby the vector $\mathbf{p}^{i+1}_{n+1}$ summarizes the updated values of the primary solution variables, and the vector $\mathbf{r}^i_{n+1}$ comprises the corresponding residual quantities:

$$\mathbf{p}^{i+1}_{n+1} = \begin{bmatrix}\mathbf{s}^{i+1}_{n+1} & \mathbf{b}^{i+1}_{n+1} & \Gamma^{i+1}_{n+1}\end{bmatrix}^{\mathrm{T}}, \tag{76}$$

$$\mathbf{r}^i_{n+1} = \begin{bmatrix}\mathbf{r}^i_\sigma & \mathbf{r}^i_\beta & r^i_\Gamma\end{bmatrix}^{\mathrm{T}}. \tag{77}$$

The solution of Eq. (75) provides the vector of increments $\Delta\mathbf{p}^{i+1}_{n+1}$, which is used to update the stress, the backstress, and the softening variable:

$$\mathbf{p}^{i+1}_{n+1} = \mathbf{p}^i_{n+1} + \Delta\mathbf{p}^{i+1}_{n+1}. \tag{78}$$

The matrix $\mathbf{A}^{i}_{n+1}$ in Eq. (75) contains the derivatives of the residuals with respect to the primary solution variables $\mathbf{s}$, $\mathbf{b}$, Γ, cf. Eisenträger et al. (2018b). The derivatives of the residuals can be calculated based on Eqs. (72)–(74). Since the resulting expressions are lengthy, the equations are not repeated here for the sake of brevity. The interested reader is referred to Eisenträger et al. (2018b), where the derivatives are presented in detail. Next, the system of equations (75) is solved via the Newton-Raphson method. Note that further details on this point can also be found in Eisenträger et al. (2018b); Eisenträger (2018). After solving the system of equations, the primary solution variables are updated based on Eq. (78), such that the current values of the stress $\mathbf{s}_{n+1}$, the backstress $\mathbf{b}_{n+1}$, and the softening variable Γ_{n+1} are known.

3.1.2 Consistent Tangent Operator

Additionally to the update of the primary solution variables, the consistent tangent operator (CTO) must be provided to implement a nonlinear constitutive model into the FEM, cf. Simo and Taylor (1985); Hartmann et al. (1997). As before, if not indicated otherwise, all variables refer to the time step t_{n+1} in the remainder of this section. Let us introduce the matrix $\mathbf{D}$ for the CTO as follows:

$$\mathbf{D} = \left.\frac{\partial \mathbf{s}}{\partial \mathbf{e}}\right|_{n+1}. \tag{79}$$

To determine the derivative of the stresses with respect to the strains, the implicit function theorem is utilized, cf. Ghorpade and Limaye (2010). Consequently, by introducing the implicit function $\mathbf{f}$:

$$\mathbf{f}(\mathbf{s}_{n+1}, \mathbf{b}_{n+1}, \Gamma_{n+1}, \mathbf{e}_{n+1}) = \mathbf{s}_{n+1} - \mathbf{C}_{n+1}\left(\mathbf{e}_{n+1} - \mathbf{e}^{\mathrm{in}}_{n} - \Delta\mathbf{e}^{\mathrm{in}}_{n+1}\right), \tag{80}$$

Eq. (64) is formulated in a matrix notation as follows:

$$\mathbf{f}(\mathbf{s}_{n+1}, \mathbf{b}_{n+1}, \Gamma_{n+1}, \mathbf{e}_{n+1}) = \mathbf{0}. \tag{81}$$

The inelastic strain increment $\Delta\mathbf{e}^{\mathrm{in}}_{n+1}$ in Eq. (80) is obtained while making use of Eqs. (57)–(60). Based on the implicit function theorem, the CTO is computed in the following way:

$$\mathbf{D} = \left.\frac{\partial \mathbf{s}}{\partial \mathbf{e}}\right|_{n+1} = -\left(\frac{\partial \mathbf{f}}{\partial \mathbf{s}_{n+1}}\right)^{-1}\frac{\partial \mathbf{f}}{\partial \mathbf{e}_{n+1}}, \tag{82}$$

whereby the arguments of the implicit function $\mathbf{f}$ are omitted for the sake of brevity. Computing the derivatives based on Eq. (80) results in:

$$\mathbf{D} = \left(\mathbf{A}_1 + \mathbf{C}_{n+1}\frac{\partial \Delta\mathbf{e}^{\mathrm{in}}_{n+1}}{\partial \mathbf{s}_{n+1}}\right)^{-1}\mathbf{C}_{n+1}, \tag{83}$$

while the derivative of the inelastic strain increment with respect to the stress is determined based on Eq. (58):

$$\frac{\partial \Delta\mathbf{e}^{\mathrm{in}}_{n+1}}{\partial \mathbf{s}_{n+1}} = \frac{3}{2}\frac{\Delta t\, f_T(T)}{\tilde{\sigma}_{\mathrm{vM}}}\left[\frac{3}{2}\left(\frac{1}{\tilde{\sigma}_{\mathrm{vM}}}\frac{\partial f_\sigma(\tilde{\sigma}_{\mathrm{vM}})}{\partial \tilde{\sigma}_{\mathrm{vM}}} - \frac{f_\sigma(\tilde{\sigma}_{\mathrm{vM}})}{\tilde{\sigma}^2_{\mathrm{vM}}}\right)\tilde{\mathbf{s}}'\left(\tilde{\mathbf{s}}'\right)^{\mathrm{T}} + f_\sigma(\tilde{\sigma}_{\mathrm{vM}})\left(\mathbf{A}_1 - \frac{1}{3}\mathbf{A}_2\right)\right], \tag{84}$$

with the auxiliary matrices $\mathbf{A}_1$ and $\mathbf{A}_2$:

$$\mathbf{A}_1 = \begin{bmatrix} 1 & 0 & 0 & 0 & 0 & 0 \\ 0 & 1 & 0 & 0 & 0 & 0 \\ 0 & 0 & 1 & 0 & 0 & 0 \\ 0 & 0 & 0 & 1 & 0 & 0 \\ 0 & 0 & 0 & 0 & 1 & 0 \\ 0 & 0 & 0 & 0 & 0 & 1 \end{bmatrix}, \qquad \mathbf{A}_2 = \begin{bmatrix} 1 & 1 & 1 & 0 & 0 & 0 \\ 1 & 1 & 1 & 0 & 0 & 0 \\ 1 & 1 & 1 & 0 & 0 & 0 \\ 0 & 0 & 0 & 0 & 0 & 0 \\ 0 & 0 & 0 & 0 & 0 & 0 \\ 0 & 0 & 0 & 0 & 0 & 0 \end{bmatrix}.$$

Using the commercial FE code ABAQUS, the stress update algorithm, presented in Sect. 3.1.1, and the CTO are implemented into the FEM via a user material (UMAT) subroutine. The accuracy and numerical performance of the implemented constitutive model based on the implicit Euler method have been examined in detail, considering several benchmarks for uniaxial and multiaxial stress and deformation states, cf. Eisenträger et al. (2018b); Eisenträger (2018).

3.2 Explicit Time Integration

3.2.1 Stress Update Algorithm

The current section presents the stress update algorithm of the mixture model based on explicit time integration, i.e. the forward Euler method is applied. In general, the following considerations are in close agreement to the derivations for the implicit Euler method in Sect. 3.1.1. For the time integration of the governing equations based on the explicit Euler method, we apply Eq. (56) to the constitutive equations. If not stated otherwise, all entities refer to the time step t_n in the remainder of this section. As before,

it is assumed that all principal variables are known for the equilibrium state at the time step t_n. Applying the forward Euler method, results in the following system of equations, which is directly formulated in a matrix notation for the sake of brevity:

$$\square_{n+1} = \square_n + \Delta\square_n \qquad \forall \quad \square = \left\{\mathbf{e}, \mathbf{e}^{\text{in}}, T, \mathbf{s}, \mathbf{b}, \Gamma\right\}, \tag{85}$$

$$\Delta\mathbf{e}^{\text{in}}_n = \frac{3}{2}\Delta t\, f_\sigma\left(\tilde{\sigma}_{\text{vM}}\right)\frac{f_T\left(T\right)}{\tilde{\sigma}_{\text{vM}}}\tilde{\mathbf{s}}', \tag{86}$$

$$\Delta\mathbf{b}_n = \frac{1}{G}\frac{\mathrm{d}G}{\mathrm{d}T}\Delta T\mathbf{b} + 2G\frac{\eta_{\text{h}_0}}{1-\eta_{\text{h}_0}}\left(\Delta\mathbf{e}^{\text{in}} - \frac{3}{2}\frac{\Delta\varepsilon^{\text{in}}_{\text{vM}}}{\beta_{\text{vM}_\star}}\mathbf{b}\right), \tag{87}$$

$$\Delta\Gamma_n = C_\Gamma\left[\Gamma_\star\left(\sigma_{\text{vM}}\right) - \Gamma\right]\Delta\varepsilon^{\text{in}}_{\text{vM}}, \tag{88}$$

$$\mathbf{s}_{n+1} = \mathbf{C}_{n+1}\left(\mathbf{e}_n + \Delta\mathbf{e}_n - \mathbf{e}^{\text{in}}_n - \Delta\mathbf{e}^{\text{in}}_n\right). \tag{89}$$

Note that in contrast to the implicit time integration, the application of an explicit method does not result in a nonlinear system of equations. Instead, Eqs. (85)–(89) directly provide the values of the primary solution variables, i.e. $\mathbf{s}_{n+1}$, $\mathbf{b}_{n+1}$, and Γ_{n+1}, with respect to the current time step t_{n+1}.

3.2.2 Consistent Tangent Operator

Despite applying an explicit time integration method, the CTO must be provided as well to implement a nonlinear constitutive model into the FEM. Following an analogous procedure as in Sect. 3.1.2 results in the following expression for the CTO in matrix notation:

$$\mathbf{D} = \left(\mathbf{A}_1 + \mathbf{C}_{n+1}\frac{\partial\Delta\mathbf{e}^{\text{in}}_n}{\partial\mathbf{s}_n}\right)^{-1}\mathbf{C}_{n+1}, \tag{90}$$

In contrast to Eq. (83), the derivative of the inelastic strain increment with respect to the stress is calculated with respect to the time step t_n, such that Eq. (84) is also evaluated with respect to the step t_n. The stress update algorithm in Sect. 3.2.1 and the CTO for explicit time integration are also implemented via the UMAT subroutine into ABAQUS. However, as it has already been discussed at the beginning of Sect. 3, explicit integration methods are only *conditionally* stable, such that if the time increments exceed a certain threshold, the so-called "critical time step size", the solution might become unstable. In order to circumvent this issue, the UMAT subroutine compares the current time increment to a critical time step size Δt_{crit} and provides a warning message if the current time step exceeds the critical value. To estimate the critical time step size for the mixture model, we have adopted the approach presented in Cormeau (1975), where the critical time step size is derived for a related constitutive approach, i.e. a von Mises viscoplasticity model with zero yield stress, suitable for the creep analysis of metals and employing similar stress and temperature response functions as presented in Sect. 2.2. Based on Cormeau (1975), the critical time step size is determined as follows:

$$\Delta t_{\text{crit}} = \frac{2}{3Ga_\sigma m_\sigma f_T(T)}\tilde{\sigma}_{\text{vM}}^{1-m_\sigma} \tag{91}$$

4 Finite Element Analysis of a Steam Turbine Rotor

4.1 Numerical Model: Procedures, Mesh, and Boundary Conditions

The thermo-mechanical behavior of the steam turbine rotor is analyzed within a partly coupled finite element analysis, using the commercial FE code ABAQUS. In a first step, a thermal analysis is conducted in order to obtain the temperature field based on the heat transfer due to the inhomogeneous and instationary steam temperatures. Afterwards, the temperature distribution is utilized as input for the subsequent structural analysis with the binary mixture model, which provides the resulting strain and stress fields. This type of partly coupled thermo-mechanical analysis is frequently applied, particularly to avoid the high computational effort of a fully coupled analysis, cf. e.g. Nayebi et al. (2012); Sun et al. (2013); Benaarbia et al. (2018). To the knowledge of the authors, the results of a fully coupled thermo-mechanical analysis of a turbine rotor have not been presented in literature yet. Furthermore, it is questionable whether the mechanical deformations exert a significant influence on the temperature field assuming moderate inelastic deformations in components in practice. However, also due to the lack of experimental data and measurements under operating conditions, this issue remains an open question. Future research could therefore concentrate on the development of a fully coupled thermo-mechanical model and the comparison of partly and full coupled approaches for the analysis of turbine rotors.
In the present analysis, all computations for the structural analysis are conducted twice, considering explicit and implicit time integration, as described in Sect. 3.1 and 3.2. Both time integration methods are critically examined with respect to the involved computational effort as well as the accuracy in Sect. 4.2. In the following two sections, the employed FE models, i.e. the meshes as well as the boundary conditions, are described both for the thermal and structural analysis.

4.1.1 Thermal Analysis

Figure 2 presents the FE model with the boundary conditions for the thermal analysis of the steam turbine rotor. The top left picture shows the geometry of the rotor, which refers to a real component used in power plants. Note that the geometry data has

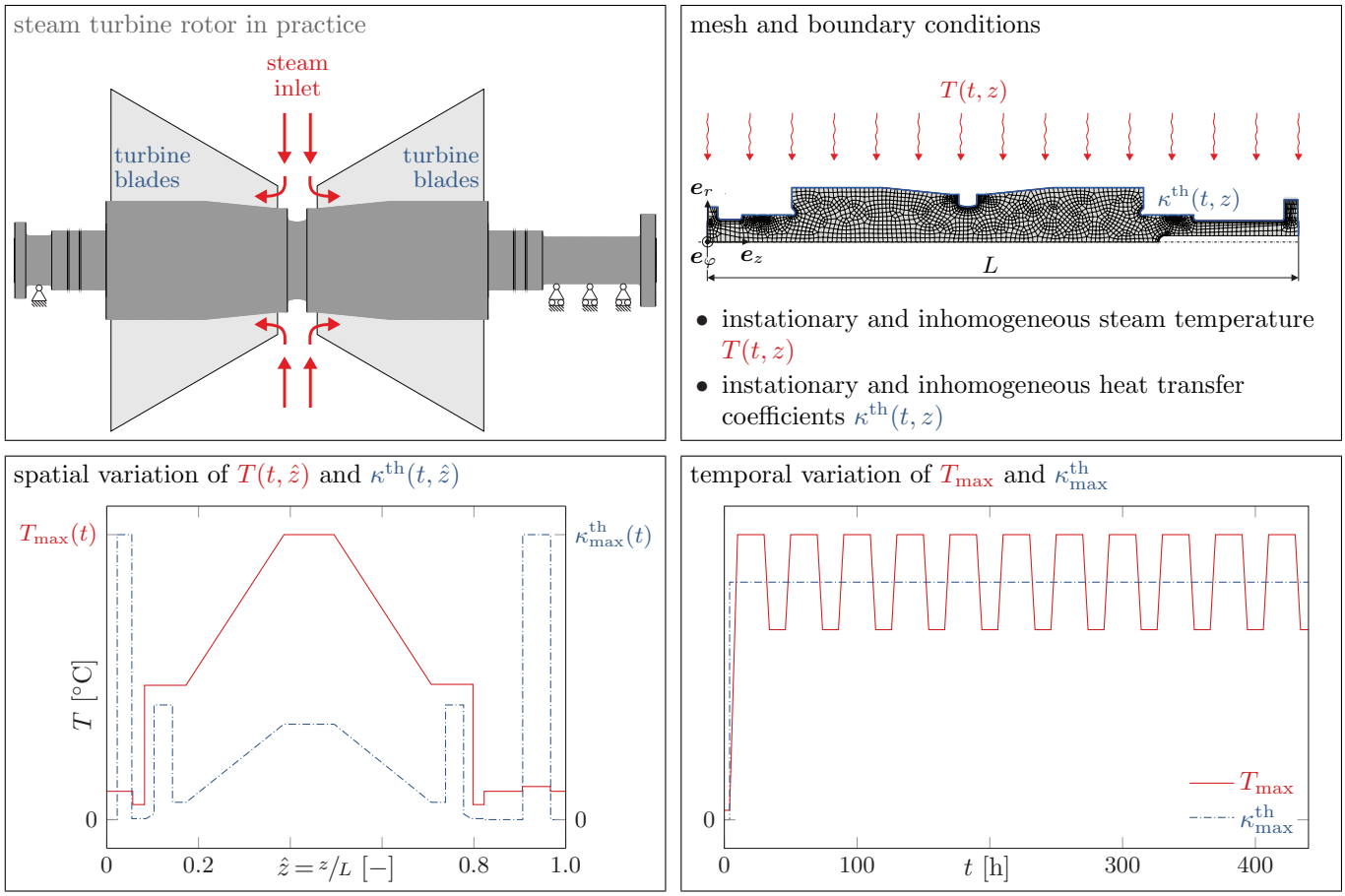

Fig. 2: Finite element model, mesh, and boundary conditions for the thermal analysis.

been provided by Siemens AG, Power and Gas Division, MÃijlheim an der Ruhr, Germany. Furthermore, Siemens AG has also given advice concerning the applied thermo-mechanical boundary conditions in order to account for the operating conditions in power plants. As depicted in the top left picture in Fig. 2, the rotor is mounted at the left and right-hand side. In the center, hot steam is lead in and redirected towards the turbine blades. Note that the blades themselves are not included in the thermal analysis, cf. the top right picture, to reduce the computational effort.

The axisymmetric mesh is shown in the top right picture in Fig. 2. From the ABAQUS element library, the 8-node heat transfer element DCAX8 with quadratic shape functions has been chosen. The depicted mesh comprises 2391 elements and 7636 nodes. In order to simulate the heat transfer based on the prescribed outer steam temperature T over the outer surface of the rotor (marked in blue color in the top right picture) inside the rotor, the ABAQUS user subroutine FILM is utilized. Thereby, we prescribe the steam temperature and the heat transfer coefficient κ^{th}, which both depend on the time and change along the longitudinal coordinate z of the rotor. The dependence of the steam temperature and the heat transfer coefficient on the normalized longitudinal coordinate $\hat{z}$ is illustrated in the bottom left picture. As to be expected, the outer temperature attains its maximum near the steam inlet of the rotor. Note that cooling systems are installed near the mountings such that the temperature decreases and the heat transfer coefficient increases at the left and right-hand side of the rotor.

Finally, the temporal variation of the maximum steam temperature and heat transfer coefficient is shown in the bottom right diagram. As the graph for the maximum temperature shows, a total of 11 thermal cycles is taken into account. The first cycle represents a cold start with a significant increase in temperature. After reaching the maximum temperature, the temperature is held constant over 20 hours (“holding stage”). Afterwards, the temperature decreases to an intermediate level and is again held constant over 12 hours. Finally, the temperature increases again from the intermediate level until the maximum is reached (warm start). Thus, 11 cycles, including one cold start and 10 warm starts, are taken into account, which allows for a comparison of the different starting procedures as well as the analysis of the cyclic behavior. In total, the simulated time span accounts for 446 hours. In contrast to the varying temperature, the maximum heat transfer coefficient $\kappa^{\mathrm{th}}_{\max}$ increases only at the initial start to account for the large differences in temperatures and heat transfer. Afterwards, the maximum heat transfer coefficient is assumed to be constant due to the intermediate temperature differences in the following cycles. Note that the temporal variation of the lower levels of temperature and heat transfer coefficient, cf. the bottom left diagram, is described by scaling the lower levels proportionally depending on the current maximum value.

4.1.2 Structural Analysis

The FE model and the boundary conditions for the structural analysis are explained in Fig. 3. As before, the top left picture displays the steam turbine rotor in practice. The top right picture shows the finite element mesh, whose nodal positions and topology are

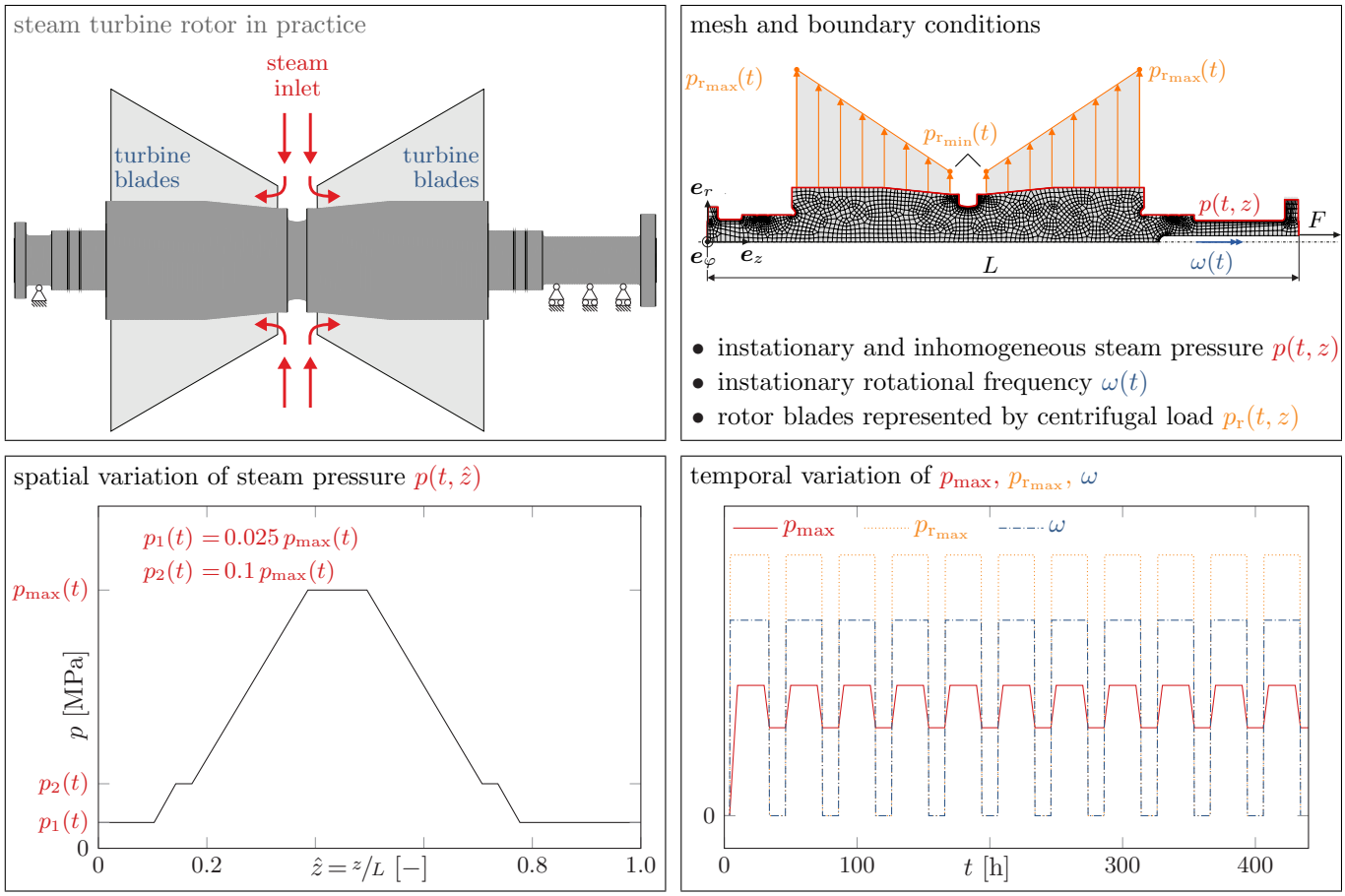

Fig. 3: Finite element model, mesh, and boundary conditions for the structural analysis.

adopted from the thermal analysis, although a different element, suitable for structural analysis, is chosen, i.e. the element CAX8 from ABAQUS' element library. Like the heat transfer element DCAX8, the quadrilateral element CAX8 features 8 nodes and uses quadratic shape functions.

As already pointed out, the temperature field obtained in the preceding thermal analysis is imported as thermal boundary condition in the structural analysis. Furthermore, the instationary and inhomogeneous steam pressure p is prescribed along the outer surface of the rotor marked in red, cf. the top right picture of Fig. 3. Similar to the steam temperature, cf. Fig. 2, the variation of the steam pressure with respect to the normalized longitudinal coordinate $\hat{z}$ of the rotor is given in the bottom left picture of Fig. 3. As one would expect, the spatial variation of the steam pressure is in close agreement with the spatial change of temperature, cf. the bottom left diagram in Fig. 2. Note that the change of the maximum steam pressure p_{max} with respect to time is given in the bottom right diagram in Fig. 3. In analogy to the proportional scaling of the temperature levels, the lower levels of the steam pressure p_1 and p_2 are adapted as well such that the ratios $p_1/p = 0.025$ and $p_2/p = 0.1$ remain constant over time.

In addition, a time-dependent rotational frequency ω is provided to simulate the various starting and shut-down procedures, cf. the pictures in the right-hand side in Fig. 3. In order to reduce the involved computational effort, the rotor blades are not modeled explicitly. Instead, they are represented by the centrifugal load p_r, which varies linearly from the minimum value $p_{r_{min}}$ at the steam inlet to its maximum $p_{r_{max}}$, in order to account for the increasing length of the rotor blades. Note that this representation of the blades by centrifugal loads is a commonly applied procedure, cf. Wang et al. (2016); Zhu et al. (2017); Benaarbia et al. (2018). To complete the overview on the mechanical boundary conditions, the maximum centrifugal load $p_{r_{max}}$ is shown depending on time in the bottom right diagram in Fig. 3.

4.2 Explicit and Implicit Time Integration

Before the obtained temperature, stress, and strain fields in the rotor are presented in detail in Sect. 4.3, we will compare the performance of the explicit and implicit Euler method for time integration. Note that this is rarely done with respect to a complex simulation of a realistic component such as a steam turbine rotor, although reducing the involved computational costs in practical simulations is of crucial importance, particularly if instationary and cyclic loads are taken into account. In order to compare both time integration methods, several structural analyses are conducted using the ABAQUS implementations of the time integration methods presented in Sect. 3. ABAQUS' automatic time stepping algorithm is used, and the maximum time step size Δt_{max} is varied systematically, i.e. $\Delta t_{max} = \{0.10\,\text{h}, 0.05\,\text{h}, 0.01\,\text{h}\}$, both for implicit and explicit time integration, such that a total of six different structural simulations is conducted. All structural simulations are based on the same temperature field, which is obtained in the preceding heat transfer analysis with lowest maximum time step size $\Delta t_{max} = 0.01\,\text{h}$. For all simulations, a Windows 7 (64 bit) desktop computer with Intel Core i7-58205 processor (clock rate 3.30 GHz) and 16 GB RAM is used.

Figure 4 comprises all required data for the comparison of the time integration methods. The top diagram shows the von Mises

stress at the point P_1, which has been chosen due to its particular position at notch root directly under the steam inlet, as indicated in the sketch in the background of Fig. 4. In the diagram, the von Mises stress is displayed depending on the simulated time, which covers all 11 cycles. Furthermore, the von Mises stress is normalized with respect to the maximum equivalent stress $\sigma_{\mathrm{vM}_{\max}}^{\mathrm{P1}}$ at the point P_1. Note that since all FE simulations yield very similar results such that the different curves could not be distinguished with the naked eye, here we only show the result of one representative simulation, i.e. the analysis involving implicit integration with lowest maximum time step size $\Delta t_{\max} = 0.01\,\mathrm{h}$ for the sake of illustration. The curve shows a total of 22 significant local stress maxima, whereby two maxima each refer to one cycle including start-up (first maximum), holding phase, and shut-down (second maximum). The presented curve is extracted for all six structural simulations and serves as basis to define the von Mises stress error Δ_{vM} as follows:

$$\Delta_{\mathrm{vM}} = \frac{\int \left(\sigma_{\mathrm{vM}}^{\mathrm{ref}} - \sigma_{\mathrm{vM}}^{\mathrm{num}}\right)^2 \mathrm{d}t}{\int \left(\sigma_{\mathrm{vM}}^{\mathrm{ref}}\right)^2 \mathrm{d}t}, \tag{92}$$

whereby the variable $\sigma_{\mathrm{vM}}^{\mathrm{num}}$ is replaced by the simulation results for explicit and implicit integration considering the variations in time stepping:

$$\sigma_{\mathrm{vM}}^{\mathrm{num}} = \left\{\sigma_{\mathrm{vM}}^{INT}\left(\Delta t_{\max} = 0.10\,\mathrm{h}\right), \sigma_{\mathrm{vM}}^{INT}\left(\Delta t_{\max} = 0.05\,\mathrm{h}\right), \sigma_{\mathrm{vM}}^{INT}\left(\Delta t_{\max} = 0.01\,\mathrm{h}\right)\right\} \qquad \forall INT = \{\mathrm{exp}, \mathrm{imp}\}\,.$$

In addition, $\sigma_{\mathrm{vM}}^{\mathrm{ref}} = \sigma_{\mathrm{vM}}^{\mathrm{imp}}\left(\Delta t_{\max} = 0.01\,\mathrm{h}\right)$ holds, i.e. the simulation results obtained with implicit time integration and smallest time steps are used as reference solution. The superscripts $\square^{\mathrm{imp}}$ and $\square^{\mathrm{exp}}$ indicate variables obtained via implicit and explicit time integration, respectively. Note that the integrals in Eq. (92) are evaluated numerically using the trapezoidal rule. To ensure equal time steps in the numerical solution $\sigma_{\mathrm{vM}}^{\mathrm{num}}$ and the reference solution $\sigma_{\mathrm{vM}}^{\mathrm{ref}}$ for applying the trapezoidal rule, the values of the numerical solution are interpolated linearly to the time steps provided by the reference solution.

The bottom left diagram in Fig. 4 shows the above defined stress error depending on the total CPU time t_{CPU} both for explicit and implicit time integration. In addition, the corresponding data is given on the right-hand side of Fig. 4 in tabular form. As one would expect, a direct correlation is found between the prescribed maximum time step size $\Delta t_{\max}$ and the required computational time t_{CPU}, i.e. the lower the maximum time step size, the longer the computational time. Furthermore, the tables show that both methods converge, i.e. the stress error decreases with decreasing time step size. Whereas we can only observe a slight reduction in the stress error for implicit integration, the stress error for explicit integration decreases significantly until a similar accuracy as for implicit integration is reached. Note that since the simulation with implicit integration and lowest maximum time step size has been chosen as reference solution, the corresponding stress error is exactly zero. Furthermore, one should point out the overall small size of the stress error, which never exceeds 0.1%.

Interestingly, we cannot observe a significant difference in computational times, especially in case of a coarser time stepping, between the implicit and explicit Euler methods. Although implicit integration requires the solution of a nonlinear system of equations, which increases the computational costs in general, as discussed at the beginning of Sect. 3, this increase in computational time is negligible for the discussed problem, i.e. the thermo-mechanical analysis of a steam turbine rotor. Note that the discussed increase in computational time is only significant for a very fine time stepping ($\Delta t_{\max} = 0.01\,\mathrm{h}$), which is futile for implicit integration due to the negligible increase in accuracy. Overall, we recommend using the implicit Euler method for the considered initial boundary value problem for two main reasons: Firstly, we can obtain a high level of accuracy in results already with a relatively coarse time stepping, which results in a reasonable computational time. Secondly, one should consider the unconditional stability of implicit methods, which is a significant advantage compared to explicit methods, cf. the discussion at the beginning of Sect. 3. On the other hand, the implementation of implicit time integration methods requires more effort compared to the straightforward formulation of explicit methods, compare Sect. 3.1 and 3.2. One should take this into account while choosing the time integration method: if few changes to the constitutive model are to be expected, implicit integration methods should be preferred. However, if more flexibility is required and changes must be implemented quickly, explicit integration methods are the right choice. Last but not least, we would like to point out that the previous considerations hold for the presented analysis of the steam turbine rotor. One should keep this in mind while transferring the previous conclusions to other initial boundary value problems. Furthermore, all statements hold only for the implicit and explicit Euler method.

4.3 Results

In the following, we will discuss various results of the thermo-mechanical finite element analysis of the rotor. Since the previous section has shown that the structural analysis using implicit time integration for the evolution equations in combination with the coarsest time stepping ($\Delta t_{\max} = 0.10\,\mathrm{h}$) yields accurate results while demanding only for a relatively low CPU time, we will focus on this particular analysis in the following.

Figure 5 shows contour plots of the temperature and normalized von Mises stress in the rotor at two particular points in time. The first point in time under consideration ($t = 10\,\mathrm{h}$) refers to the highest temperature difference $|T_{\mathrm{A}} - T_{\mathrm{B}}|$, which occurs after heating-up in the cold start. Note that T_{A} represents the temperature at point A at notch root at the outer surface of the rotor, as indicated in Fig. 5. The variable T_{B} denotes the temperature at point B, which features the same longitudinal position as point A, but is located at the axis of rotation, i.e. inside the rotor. The second point in time ($t = 30\,\mathrm{h}$) marks the end of the holding stage during the first cycle. Moreover, the top picture in Fig. 5 depicts both temperatures depending on time. One can distinguish the 11 cycles clearly. Note that the graph with respect to the temperature T_{B} is slightly shifted in positive direction of the time axis. Furthermore, the highest temperature at point B is lower than the maximum temperature T_{A}. Both observations can be explained

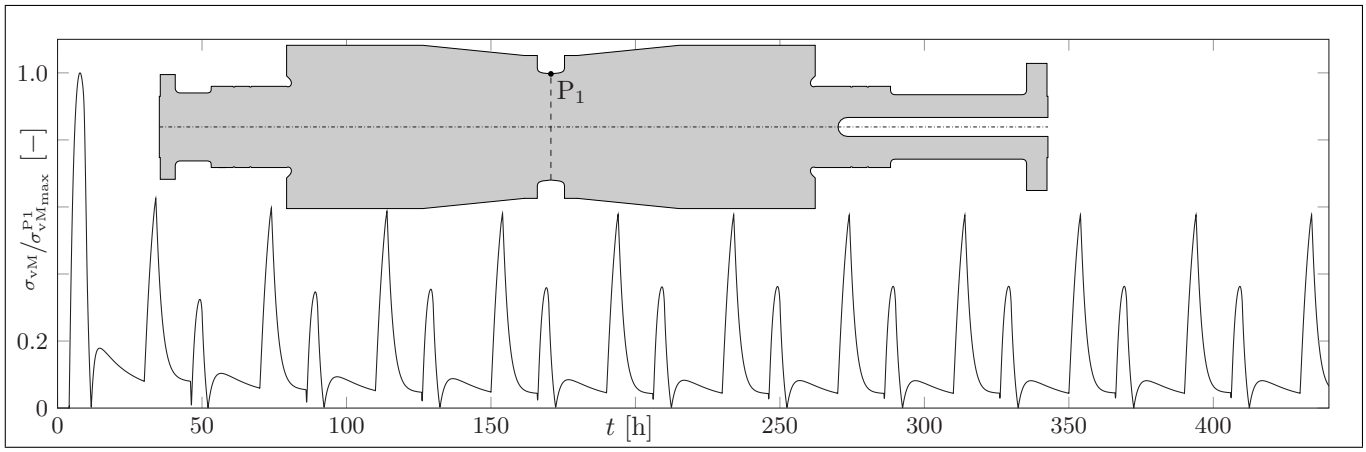

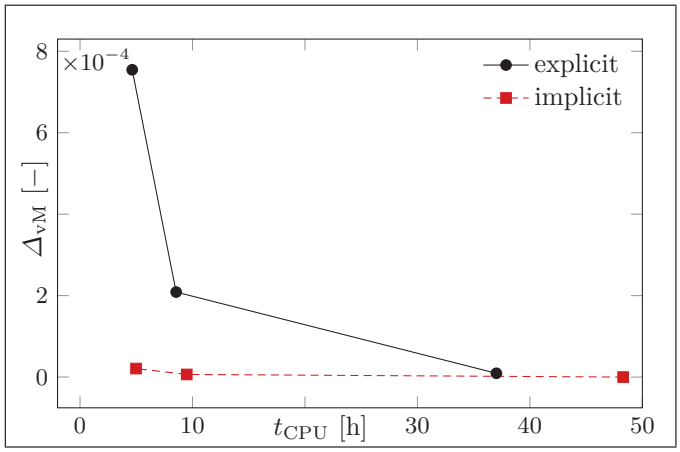

performance of explicit time integration

#	$\Delta t_{\max}$ [h]	t_{CPU} [h]	Δ_{vM} [%]
1	0.10	4.637	0.07545
2	0.05	8.546	0.02087
3	0.01	37.019	0.00093

performance of implicit time integration

#	$\Delta t_{\max}$ [h]	t_{CPU} [h]	Δ_{vM} [%]
1	0.10	4.979	0.00209
2	0.05	9.488	0.00065
3	0.01	48.291	0.00000

Fig. 4: Comparison of explicit and implicit time integration methods. Top: Normalized von Mises stress at point P_1 vs. time. Bottom left: von Mises stress error vs. CPU time. Bottom right: CPU times and von Mises stress error as tabular data.

by the interior position of point B and the relatively slow heat transfer over the outer surface into the rotor. In addition, the chosen points in time are indicated by the red ($t = 10\,\mathrm{h}$) and blue ($t = 30\,\mathrm{h}$) vertical lines in the top picture in Fig. 5.

After 10 h, i.e. at the end of the heating-up and before the beginning of the holding stage, the highest absolute temperature difference between points A and B is attained (217 K). The two contour plots below the top picture refer to this point in time. It is worth noting that the two different starting procedures influence the temperature and stress fields significantly. Whereas the maximum temperature difference during the cold start accounts for 217 K, the highest temperature difference during the subsequent warm starts is significantly lower (112 K at $t = 50\,\mathrm{h}$, for example). In addition, one observes that during heating-up (and cooling-down) the temperature gradient is mainly effective in radial direction. Contrarily, in holding stage temperatures change primarily in longitudinal direction, as can be seen in the fourth picture from the top. Moreover, the large temperature differences during the cold start induce very high stresses in the rotor, cf. the third picture in Fig. 5. As one can observe, high stresses affect the rotor blade area, i.e. the part of the upper surface of the rotor, where the rotor blades are mounted, cf. Fig. 3. This is an issue of high importance since steam turbine rotors usually have several notches in this area to mount the rotor blades. Due to the stress concentration at the notches, the actual stresses in this area could exceed the results presented in this paper. These findings are also confirmed by Wang et al. (2016), where it is demonstrated that the total damage in the rotor concentrates near the blade grooves as well as the steam inlet notch zone. Last but not least, the bottom picture in Fig. 5 shows the contour plot of the normalized von Mises stress at the end of the holding stage in the first cycle ($t = 30\,\mathrm{h}$). Since the temperature difference accounts for only 13 K, the stresses in holding stage are significantly reduced compared to the stresses in the rotor after the cold start.

Based on the obtained contour plots of the von Mises stress in Fig. 5, the three critical points P_1, P_2, and P_3 have been chosen, cf. also the sketch in Fig. 6. While the first two points are located in the central notch at the steam inlet of the rotor, the third point is at the outer surface in the rotor blade area. Figure 6 shows the normalized von Mises stress in these points over time. It becomes obvious that the absolute highest stresses occur during the heating-up in cold start ($4\,\mathrm{h} \leq t \leq 10\,\mathrm{h}$). During the subsequent cycles, i.e. the warm starts, the stresses in cooling-down stage are significantly higher than the corresponding stresses while heating-up, which is due to the relatively fast cooling-down of the steam turbine rotor. Furthermore, we can observe a continuous decrease in the stress maximum in all three specific points throughout the cycles. This behavior is attributed to softening, which is taken into account by the employed mixture model. After all, the point P_2 is most critical because the highest stresses occur at this location. Therefore, the subsequent considerations will focus on this point.

Next, stress and strain components are analyzed at the point P_2. While Fig. 7 displays the normalized stresses and strains at this point over time during the first two cycles only, Fig. 8 provides information on the same variables over the entire computed time, i.e. 11 cycles. The tangential, the circumferential, and the normal components are given with respect to the displayed coordinate

system in the sketch in the top diagram of Fig. 7. Note that these components also represent the principal stresses and strains at the point P_2. Figure 7 provides a detailed view of the first two cycles. We can observe that the absolute highest stresses and strains occur during the heating-up in the cold start (4 . . . 10 h). Whereas the rotor is compressed during the cold and warm starts, stresses and strains are in tensile regime during cooling-down, e.g. at $t \approx 35$ h and $t \approx 75$ h. As has also been stated before, starting with the second cycle (the first warm start), the stresses during cooling-down ($t \approx 75$ h) exceed the corresponding stresses during heating-up ($t \approx 50$ h). Moreover, the stresses decrease constantly during the holding stage (15 . . . 30 h), while the strains increase simultaneously. This indicates creep and relaxation, which are to be expected due to the constant operating conditions during holding stage.

Figure 8 displays the same variables over all 11 cycles. The top diagram clearly shows a slight, but continuous decrease in the maximum values of the circumferential and tangential stresses throughout all cycles. Once more, this decrease in the stress amplitude reveals the occurrence of softening in the material. In addition, the lower diagram provides information on the dependence of the normalized mechanical strains on time. Analogously to the stress components, we can observe a continuous

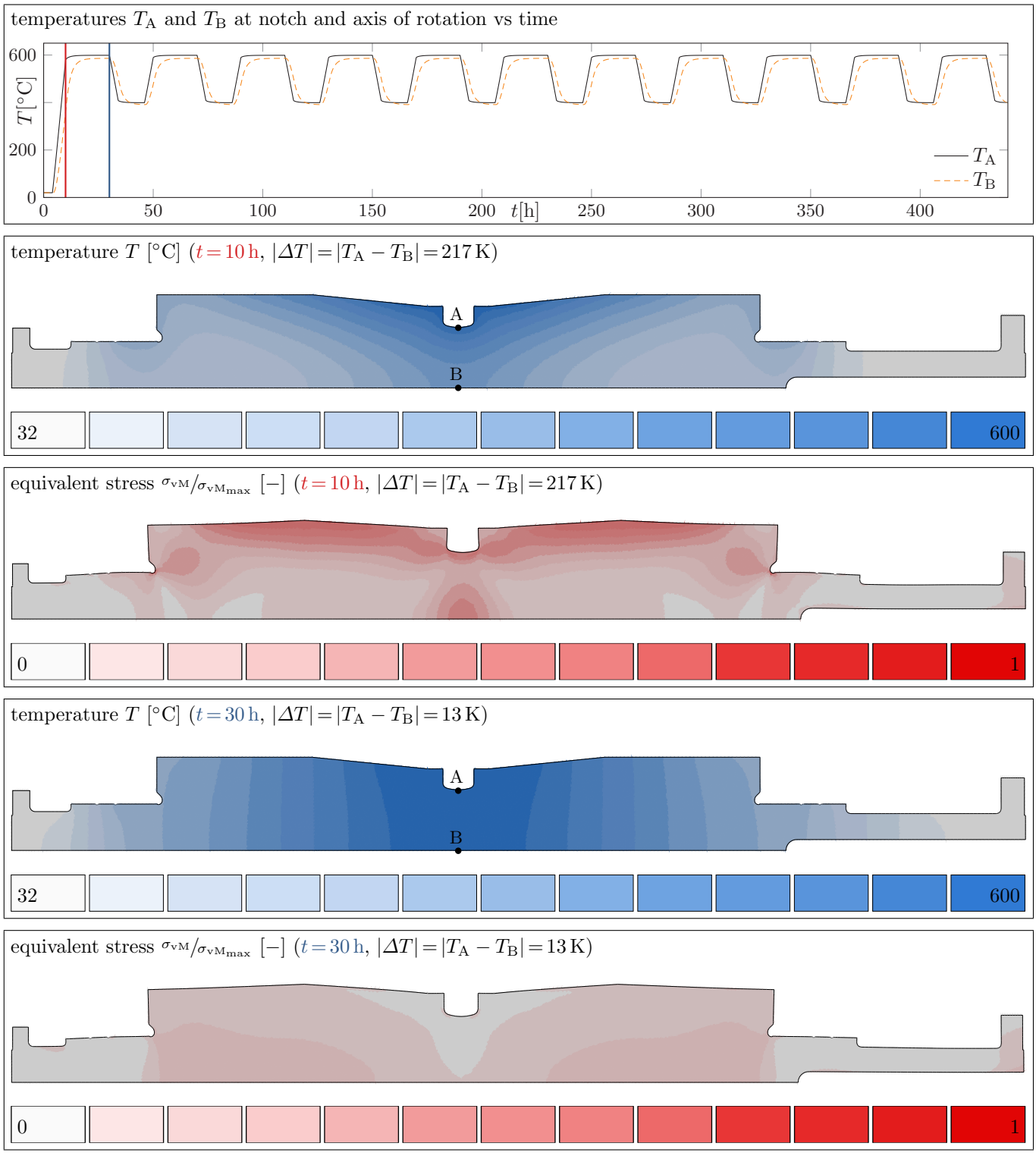

Fig. 5: Contour plots of temperature and normalized von Mises stress in the rotor after 10 h (cold start) and 30 h (holding stage).

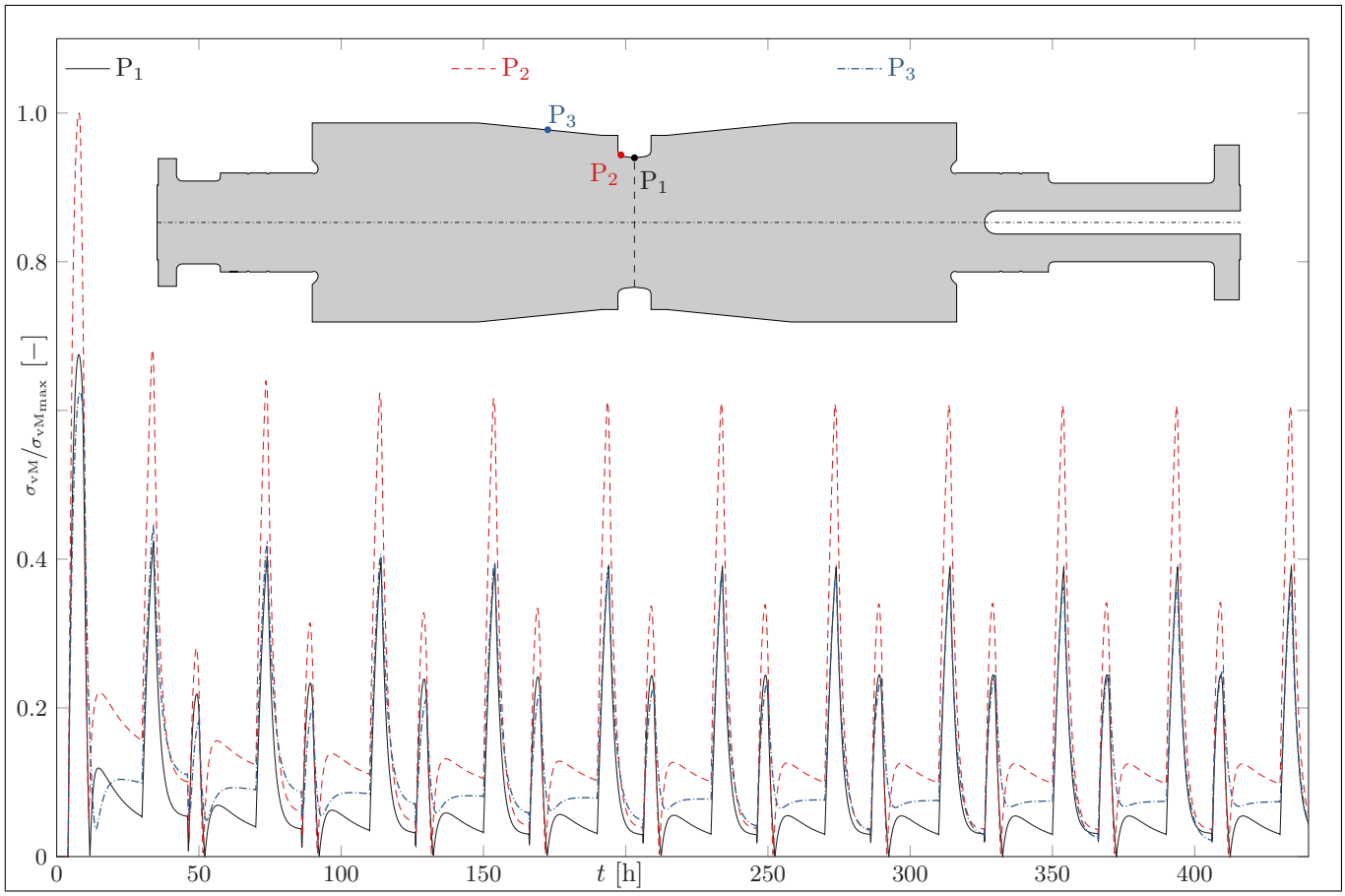

Fig. 6: Normalized von Mises stress in the rotor at three specific points on the steam turbine rotor over time.

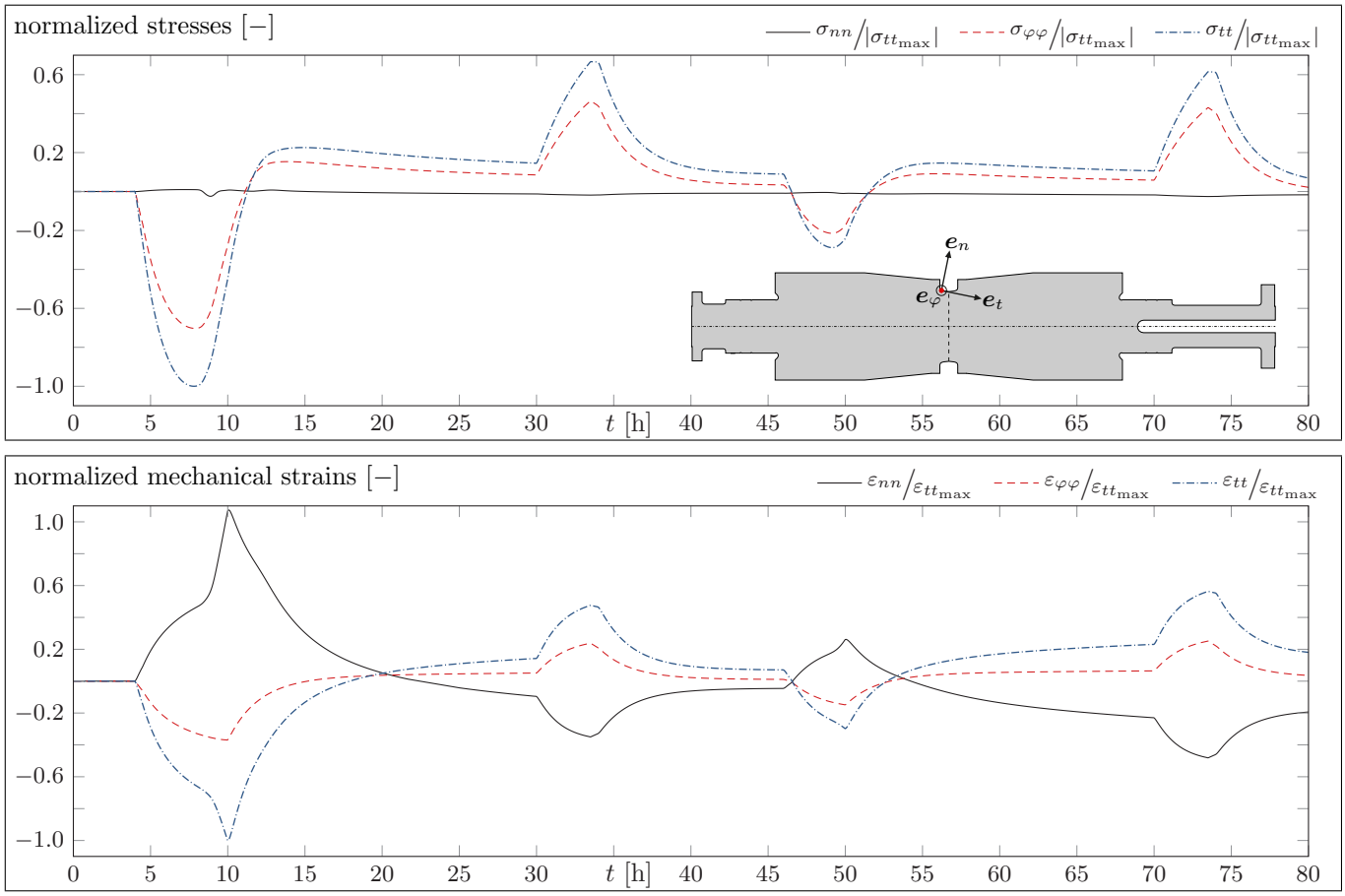

Fig. 7: Normalized stresses and strains at the Point P_2 over time during the first two cycles.

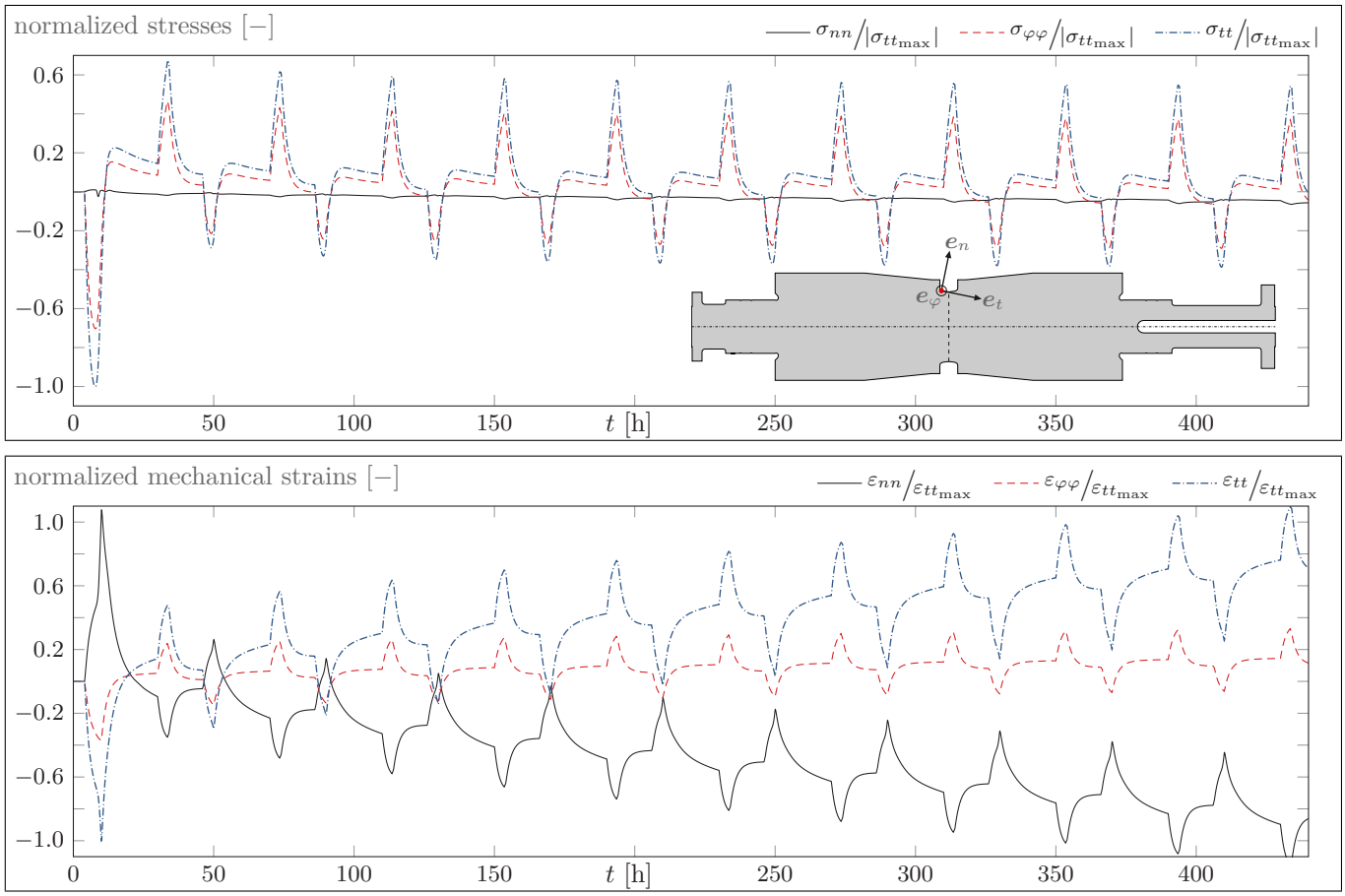

Fig. 8: Normalized stresses and strains at the Point P_2 over time during all 11 cycles.

increase in the maximum tangential and circumferential strains as well as a steady decrease in the minimum values of the normal strain. Thus, the absolute strain values increase during the cycles, and the steam turbine rotor is affected by ratcheting due to the cyclic loads. Note that qualitatively similar simulation results with respect to the stresses and strains have been obtained in Naumenko et al. (2011b); Eisenträger (2018), while analyzing a rotor with idealized geometry.

5 Summary and Outlook

The contribution at hand has presented results of a thermo-mechanical analysis of a steam turbine rotor using a mixture model. The mixture model has been chosen because it provides a robust description of the complex mechanical behavior of high-chromium heat-resistant steels, including rate-dependent inelasticity, (kinematic) hardening, and softening. Furthermore, the model offers three advantages to other approaches: a small number of parameters, the calibration based on simple macroscopic material tests, and its applicability to wide ranges of stress and temperature. Note that the mixture model results in a coupled system of three evolution equations with respect to the inelastic strain, a backstress, and a softening variable. In order to solve this system numerically while implementing the mixture model in the FE code ABAQUS, the current paper applied both the implicit and explicit Euler method and provided detailed information on the derivations of the corresponding stress update algorithms and the consistent tangent operators. This revealed one major advantage of explicit integration methods compared to implicit approaches, i.e. the straightforward implementation of explicit integration methods, which requires significantly less effort in transforming the governing equations compared to implicit approaches.

Next, the paper demonstrated the applicability of the mixture model to a complex thermo-mechanical problem by analyzing a steam turbine rotor with complicated geometry in step with actual practice. Special emphasis was put on the accurate description and close-to-practice implementation of the boundary conditions. Within the preceding thermal analysis with ABAQUS, the temperature field in the rotor was obtained based on the prescribed instationary steam temperatures and heat transfer coefficients. The temperature distribution served as input for the subsequent structural analysis with the mixture model. Furthermore, the simulation covered 11 thermo-mechanical cycles to account for the creep-fatigue loads in real power plant components.

Afterwards, the numerical performance of the explicit and implicit Euler method has been examined in detail by varying the time step sizes systematically. Especially for coarser time stepping, a significant difference in computational times could not be observed. Furthermore, it has been found that both methods result in small stress errors. For the considered boundary value problem, we recommended the implicit Euler method due to two reasons: a high level of accuracy in results, while requiring an acceptable amount of computational time, and the unconditional stability of implicit integration. However, one should keep in mind that the application of implicit methods requires significantly more effort in deriving the equations such that explicit integration schemes should be preferred in cases of frequent changes in the constitutive model.

Finally, we focused on the simulation referring to the largest time step (0.10 h) based on implicit time integration and discussed the corresponding results in detail, with special emphasis on the influence of the different starting procedures (warm and cold starts). It was found that the highest temperature gradients in the rotor occurred in radial direction directly after the cold start. Furthermore, the maximum temperature gradient during the cold start significantly exceeded the highest temperature difference during the subsequent warm starts (217 K in comparison to 112 K, respectively). Consequently, the large temperature differences during the cold start induce significantly higher stresses in the rotor, compared to the stress state during the warm starts. Furthermore, it has been found that particularly in the rotor blade area high stresses occurred, which should be taken into account in a lifetime assessment of a steam turbine rotor. Throughout the thermo-mechanical cycling, the steam turbine rotor is affected both by softening and ratcheting, which is accounted for by the binary mixture model.
Thus, the presented constitutive model provides a robust description of the mechanical behavior of steam turbine rotors. The obtained stress and strain fields could serve as a basis for a subsequent damage analysis to assess the lifetime of power plant components under realistic boundary conditions. Since it is possible to extend the binary mixture model by a damage variable, cf. Naumenko et al. (2011a), this will be the subject of a forthcoming paper. Additionally, one should consider the application of extrapolation techniques to the presented analysis of the steam turbine rotor such that one could predict the long-term mechanical behavior based on the simulation of only a few initial thermo-mechanical cycles. Due to the involved computational costs, this represents an issue of high importance, and the accuracy of proposed extrapolation techniques should be examined carefully.

Acknowledgment

The authors would like to thank Dr. Yevgen Kostenko (Siemens AG, Power and Gas Division, MÃijlheim an der Ruhr, Germany) for providing all required data concerning the geometry as well as the boundary conditions and loads of the steam turbine rotor. Furthermore, the authors are grateful for the continuous advice and helpful discussions with Dr. Kostenko.

References

R. Agamennone, W. Blum, C. Gupta, and J. K. Chakravartty. Evolution of microstructure and deformation resistance in creep of tempered martensitic 9–12%Cr–2%W–5%Co steels. *Acta Materialia*, 54(11):3003–3014, 2006. doi: 10.1016/j.actamat.2006.02.038.

S. Alsagabi, T. Shrestha, and I. Charit. High temperature tensile deformation behavior of Grade 92 steel. *Journal of Nuclear Materials*, 453(1-3):151–157, 2014. doi: 10.1016/j.jnucmat.2014.06.033.

P. J. Armstrong and C. O. Frederick. A Mathematical Representation of the Multiaxial Bauschinger Effect. Technical report, Berkeley Nuclear Laboratories, 1966.

R. J. Atkin and R. E. Craine. Continuum theories of mixtures: basic theory and historical development. *The Quarterly Journal of Mechanics and Applied Mathematics*, 29(2):209–244, 1976. doi: 10.1093/qjmam/29.2.209.

T. Barkar and J. Ågren. Creep simulation of 9–12% Cr steels using the composite model with thermodynamically calculated input. *Materials Science and Engineering: A*, 395(1–2):110–115, 2005. doi: 10.1016/j.msea.2004.12.004.

R. A. Barrett, P. E. O'Donoghue, and S. B. Leen. An improved unified viscoplastic constitutive model for strain-rate sensitivity in high temperature fatigue. *International Journal of Fatigue*, 48:192–204, 2013. doi: 10.1016/j.ijfatigue.2012.11.001.

T. Belytschko, W. K. Liu, and B. Moran. *Nonlinear Finite Elements for Continua and Structures*. John Wiley & Sons, 2000.

A. Benaarbia, Y. Rae, and W. Sun. Unified viscoplasticity modelling and its application to fatigue-creep behaviour of gas turbine rotor. *International Journal of Mechanical Sciences*, 136:36–49, 2018. doi: 10.1016/j.ijmecsci.2017.12.008.

H. Berns and W. Theisen. *Eisenwerkstoffe - Stahl und Gusseisen*. Springer Berlin Heidelberg, 2008. doi: 10.1007/978-3-540-79957-3.

J. L. Chaboche. Constitutive equations for cyclic plasticity and cyclic viscoplasticity. *International Journal of Plasticity*, 5(3): 247–302, 1989. doi: 10.1016/0749-6419(89)90015-6.

J. L. Chaboche and G. Rousselier. On the Plastic and Viscoplastic Constitutive Equations: Part II: Application of Internal Variable Concepts to the 316 Stainless Steel. *Journal of Pressure Vessel Technology*, 105(2):159–164, 1983. doi: 10.1115/1.3264258.

H. Chilukuru, K. Durst, S. Wadekar, M. Schwienheer, A. Scholz, C. Berger, K. H. Mayer, and W. Blum. Coarsening of precipitates and degradation of creep resistance in tempered martensite steels. *Materials Science and Engineering: A*, 510-511:81–87, 2009. doi: 10.1016/j.msea.2008.04.088.

I. Cormeau. Numerical stability in quasi-static elasto/visco-plasticity. *International Journal for Numerical Methods in Engineering*, 9(1):109–127, 1975. doi: 10.1002/nme.1620090110.

J. Eisenträger. *A Framework for Modeling The Mechanical Behavior of Tempered Martensitic Steels at High Temperatures*. PhD thesis, Otto von Guericke University Magdeburg, 2018.

J. Eisenträger, K. Naumenko, H. Altenbach, and E. Gariboldi. Analysis of Temperature and Strain Rate Dependencies of Softening Regime for Tempered Martensitic Steel. *The Journal of Strain Analysis for Engineering Design*, 52:226–238, 2017. doi: 10.1177/0309324717699746.

J. Eisenträger, K. Naumenko, and H. Altenbach. Calibration of a Phase Mixture Model for Hardening and Softening Regimes in Tempered Martensitic Steel Over Wide Stress and Temperature Ranges. *The Journal of Strain Analysis for Engineering Design*, 53:156–177, 2018a. doi: 10.1177/0309324718755956.

J. Eisenträger, K. Naumenko, and H. Altenbach. Numerical implementation of a phase mixture model for rate-dependent inelasticity of tempered martensitic steels. *Acta Mechanica*, 229:3051–3068, 2018b. doi: 10.1007/s00707-018-2151-1.

B. Fournier, M. Sauzay, M. Mottot, H. Brillet, I. Monnet, and A. Pineau. Experimentally Based Modelling of Cyclically Induced Softening in a Martensitic Steel at High Temperature. In I. A. Shibli, S. R. Holdsworth, and G. Merckling, editors, *ECCC Creep Conference*, pages 649–661. DES tech publications, 2005.

B. Fournier, M. Sauzay, F. Barcelo, E. Rauch, A. Renault, T. Cozzika, L. Dupuy, and A. Pineau. Creep-Fatigue Interactions in a 9 Pct Cr-1 Pct Mo Martensitic Steel: Part II. Microstructural Evolutions. *Metallurgical and Materials Transactions A*, 40(2): 330–341, 2009a. doi: 10.1007/s11661-008-9687-y.

B. Fournier, M. Sauzay, A. Renault, F. Barcelo, and A. Pineau. Microstructural evolutions and cyclic softening of 9%Cr martensitic steels. *Journal of Nuclear Materials*, 386-388:71–74, 2009b. doi: 10.1016/j.jnucmat.2008.12.061.

B. Fournier, M. Salvi, F. Dalle, Y. de Carlan, C. Caës, M. Sauzay, and A. Pineau. Lifetime prediction of 9–12%Cr martensitic steels subjected to creep–fatigue at high temperature. *International Journal of Fatigue*, 32(6):971–978, 2010. doi: 10.1016/j.ijfatigue.2009.10.017.

B. Fournier, F. Dalle, M. Sauzay, J. Longour, M. Salvi, C. Caës, I. Tournié, P.-F. Giroux, and S.-H. Kim. Comparison of various 9–12%Cr steels under fatigue and creep-fatigue loadings at high temperature. *Materials Science and Engineering: A*, 528 (22-23):6934–6945, 2011a. doi: 10.1016/j.msea.2011.05.046.

B. Fournier, M. Sauzay, and A. Pineau. Micromechanical model of the high temperature cyclic behavior of 9–12%Cr martensitic steels. *International Journal of Plasticity*, 27(11):1803–1816, 2011b. doi: 10.1016/j.ijplas.2011.05.007.

S. R. Ghorpade and B. V. Limaye. *A Course in Multivariable Calculus and Analysis*. Springer New York, 2010. doi: 10.1007/978-1-4419-1621-1.

P. F. Giroux, F. Dalle, M. Sauzay, J. Malaplate, B. Fournier, and A. F. Gourgues-Lorenzon. Mechanical and microstructural stability of P92 steel under uniaxial tension at high temperature. *Materials Science and Engineering: A*, 527(16-17):3984–3993, 2010. doi: 10.1016/j.msea.2010.03.001.

G. Götz. *Langzeitentwicklung der Mikrostruktur neuer 9-12% Chromstähle für den Einsatz in Kraftwerken*. PhD thesis, Universität Erlangen-Nürnberg, Erlangen-Nürnberg, 2004.

S. Hartmann and P. Haupt. Stress computation and consistent tangent operator using non-linear kinematic hardening models. *International Journal for Numerical Methods in Engineering*, 36(22):3801–3814, 1993. doi: 10.1002/nme.1620362204.

S. Hartmann, G. Lührs, and P. Haupt. An efficient stress algorithm with applications in viscoplasticity and plasticity. *International Journal for Numerical Methods in Engineering*, 40(6):991–1013, 1997. doi: 10.1002/(SICI)1097-0207(19970330)40:6<991::AID-NME98ater3.0.CO;2-H.

C. Hu and H. Liu. Implicit and explicit integration schemes in the anisotropic bounding surface plasticity model for cyclic behaviours of saturated clay. *Computers and Geotechnics*, 55:27–41, 2014. doi: 10.1016/j.compgeo.2013.07.012.

M. Itskov. *Tensor Algebra and Tensor Analysis for Engineers: With Applications to Continuum Mechanics*. Springer International Publishing, 2019. doi: 10.1007/978-3-319-98806-1.

J. P. Jing, Y. Sun, S. B. Xia, and G. T. Feng. A continuum damage mechanics model on low cycle fatigue life assessment of steam turbine rotor. *International Journal of Pressure Vessels and Piping*, 78(1):59–64, 2001. doi: 10.1016/s0308-0161(01)00005-9.

J. P. Jing, G. Meng, Y. Sun, and S. B. Xia. An effective continuum damage mechanics model for creep-fatigue life assessment of a steam turbine rotor. *International Journal of Pressure Vessels and Piping*, 80(6):389–396, 2003. doi: 10.1016/s0308-0161(03)00070-x.

M. Kobayashi, M. Mukai, H. Takahashi, N. Ohno, T. Kawakami, and T. Ishikawa. Implicit integration and consistent tangent modulus of a time-dependent non-unified constitutive model. *International Journal for Numerical Methods in Engineering*, 58(10):1523–1543, 2003. doi: 10.1002/nme.825.

Y. Kostenko, H. Almstedt, K. Naumenko, S. Linn, and A. Scholz. Robust Methods for Creep Fatigue Analysis of Power Plant Components Under Cyclic Transient Thermal Loading. In *ASME Turbo Expo 2013: Turbine Technical Conference and Exposition*, volume Volume 5B: Oil and Gas Applications; Steam Turbines. Siemens Energy, Inc., 2013. doi: 10.1115/GT2013-95680.

L. X. Luccioni, J. M. Pestana, and R. L. Taylor. Finite element implementation of non-linear elastoplastic constitutive laws using local and global explicit algorithms with automatic error control. *International Journal for Numerical Methods in Engineering*, 50(5):1191–1212, 2001. doi: 10.1002/1097-0207(20010220)50:5<1191::AID-NME73>3.0.CO;2-T.

M. T. Manzari and R. Prachathananukit. On integration of a cyclic soil plasticity model. *International Journal for Numerical and Analytical Methods in Geomechanics*, 25(6):525–549, 2001. doi: 10.1002/nag.140.

K. Naumenko and H. Altenbach. *Modeling High Temperature Materials Behavior for Structural Analysis: Part I: Continuum Mechanics Foundations and Constitutive Models*. Advanced Structured Materials. Springer International Publishing, 2016. doi: 10.1007/978-3-319-31629-1.

K. Naumenko, H. Altenbach, and A. Kutschke. A Combined Model for Hardening, Softening, and Damage Processes in Advanced Heat Resistant Steels at Elevated Temperature. *International Journal of Damage Mechanics*, 20(4):578–597, 2011a. doi: 10.1177/1056789510386851.

K. Naumenko, A. Kutschke, Y. Kostenko, and T. Rudolf. Multi-axial thermo-mechanical analysis of power plant components from 9–12% Cr steels at high temperature. *Engineering Fracture Mechanics*, 78(8):1657–1668, 2011b. doi: 10.1016/j.engfracmech.2010.12.002.

A. Nayebi, H. Ranjbar, and H. Rokhgireh. Analysis of unified continuum damage mechanics model of gas turbine rotor steel: Life assessment. *Proceedings of the Institution of Mechanical Engineers, Part L: Journal of Materials: Design and Applications*, 227(3):216–225, 2012. doi: 10.1177/1464420712456513.

A. Orlová, J. Buršík, K. Kuchřoavá, and V. Sklenička. Microstructural development during high temperature creep of 9% Cr steel. *Materials Science and Engineering A*, 245:39–48, 1998. doi: 10.1016/S0921-5093(97)00708-9.

C. Pétry and G. Lindet. Modelling creep behaviour and failure of 9Cr–0.5Mo–1.8W–VNb steel. *International Journal of Pressure Vessels and Piping*, 86(8):486–494, 2009. doi: 10.1016/j.ijpvp.2009.03.006.

P. Polcik. *Modellierung des Verformungsverhaltens der warmfesten 9-12% Chromstähle im Temperaturbereich von 550-650°C*. PhD thesis, Friedrich-Alexander-Universität, Erlangen-Nürnberg, 1998.

S. V. Raj, I. S. Iskovitz, and A. D. Freed. Modeling the Role of Dislocation Substructure during Class M and Exponential Creep. In A. S. Krausz and K. Krausz, editors, *Unified Constitutive Laws of Plastic Deformation*, pages 343–439. Academic Press, Inc., 1996.

D. R. Röttger. *Untersuchungen zum Wechselverformungs- und Zeitstandverhalten der Stähle X20CrMoV121 und X10CrMoVNb91*. PhD thesis, Universität GH, Essen, 1997.

A. A. Saad. *Cyclic plasticity and creep of power plant materials*. PhD thesis, University of Nottingham, Nottingham, 2012. URL http://eprints.nottingham.ac.uk/id/eprint/12538.

A. V. Shutov and R. Kreißig. Finite strain viscoplasticity with nonlinear kinematic hardening: Phenomenological modeling and time integration. *Computer Methods in Applied Mechanics and Engineering*, 197(21-24):2015–2029, 2008. doi: 10.1016/j.cma.2007.12.017.

C. B. Silbermann, A. V. Shutov, and J. Ihlemann. Modeling the evolution of dislocation populations under non-proportional loading. *International Journal of Plasticity*, 55:58–79, 2014. doi: 10.1016/j.ijplas.2013.09.007.

J. C. Simo and T. J. R. Hughes. *Computational Inelasticity*. Springer, 1998. doi: 10.1007/b98904.

J. C. Simo and R. L. Taylor. Consistent tangent operators for rate-independent elastoplasticity. *Computer Methods in Applied Mechanics and Engineering*, 48(1):101–118, 1985. doi: 10.1016/0045-7825(85)90070-2.

S. Straub. *Verformungsverhalten und Mikrostruktur warmfester martensitischer 12%-Chromstähle*. PhD thesis, Friedrich-Alexander-Universität, Erlangen-Nürnberg, 1995.

Y.-J. Sun, X.-Q. Liu, L.-S. Hu, and X.-Y. Tang. Online life estimation for steam turbine rotor. *Journal of Loss Prevention in the Process Industries*, 26(1):272–279, 2013. doi: 10.1016/j.jlp.2012.11.008.

V. Velay, G. Bernhart, and L. Penazzi. Cyclic behavior modeling of a tempered martensitic hot work tool steel. *International Journal of Plasticity*, 22(3):459–496, 2006. doi: 10.1016/j.ijplas.2005.03.007.

J. Wang, P. Steinmann, J. Rudolph, and A. Willuweit. Simulation of creep and cyclic viscoplastic strains in high-Cr steel components based on a modified Becker–Hackenberg model. *International Journal of Pressure Vessels and Piping*, 128: 36–47, 2015. doi: 10.1016/j.ijpvp.2015.02.003.

L. Wang, M. Li, and J. Almer. In situ characterization of Grade 92 steel during tensile deformation using concurrent high energy X-ray diffraction and small angle X-ray scattering. *Journal of Nuclear Materials*, 440(1-3):81–90, 2013. doi: 10.1016/j.jnucmat.2013.04.063.

W. Z. Wang and Y. Z. Liu. Continuum damage mechanics-based analysis of creep-fatigue interaction behavior in a turbine rotor. *International Journal of Damage Mechanics*, 2018. doi: 10.1177/1056789518775174.

W. Z. Wang, P. Buhl, A. Klenk, and Y. Z. Liu. The effect of in-service steam temperature transients on the damage behavior of a steam turbine rotor. *International Journal of Fatigue*, 87:471–483, 2016. doi: 10.1016/j.ijfatigue.2016.02.040.

P. Wriggers. *Nonlinear Finite Element Methods*. Springer Berlin Heidelberg, 2008. doi: 10.1007/978-3-540-71001-1.

S.-L. Zhang and F.-Z. Xuan. Interaction of cyclic softening and stress relaxation of 9–12% Cr steel under strain-controlled fatigue-creep condition: Experimental and modeling. *International Journal of Plasticity*, 98:45–64, 2017. doi: 10.1016/j.ijplas.2017.06.007.

X. Zhu, H. Chen, F. Xuan, and X. Chen. Cyclic plasticity behaviors of steam turbine rotor subjected to cyclic thermal and mechanical loads. *European Journal of Mechanics A/Solids*, 66:243–255, 2017. doi: 10.1016/j.euromechsol.2017.07.012.

Y. Zhu, G. Kang, Q. Kan, and O. T. Bruhns. Logarithmic stress rate based constitutive model for cyclic loading in finite plasticity. *International Journal of Plasticity*, 54:34–55, 2014. doi: 10.1016/j.ijplas.2013.08.004.

O. C. Zienkiewicz and R. L. Taylor. *The finite element method for solid and structural mechanics*. Elsevier Butterworth-Heinemann, Amsterdam and Boston, 2005.

TECHNISCHE MECHANIK
an open access journal

journal homepage: www.ovgu.de/techmech

Tech. Mech., Vol. 39, Is. 3, (2019), 282–297

Received: 26.08.2019
Accepted: 26.09.2019
Available online: 01.10.2019

Simulating and Evaluating Synchronized Vibrations in Macroscopic Tribological Contacts

J. H. Merlis[1] and G.-P. Ostermeyer[1]*

[1] TU Braunschweig, Institute of Dynamics and Vibrations, Schleinitzstraße 20, 38106 Braunschweig, Germany

Abstract: High-frequency synchronized vibrations in the friction contact constitute one known triggering mechanism of certain types of NVH phenomena in automotive brakes. Towards an improved understanding of the associated physical processes, vibrations of contact patches in the tribological boundary layer are computed using the Abstract Cellular Automaton simulation program. Various studies are presented, each illustrating unique types of local phenomena and observable global behaviors. For example, simulations are carried out on multiple timescales, enabling investigations into the emergence of global patch coverage states and the resulting vibrational behavior in the tribological contact. Relevant means for analyzing and interpreting these results are introduced, including a qualitative visual representation scheme, frequency analyses of the global coefficient of friction, and a new method for quantifying the synchronization of multiple oscillating bodies.

Keywords: cellular automaton, simulation, boundary layer dynamics, patch dynamics, synchronized vibrations, brake squeal

1 Introduction

Friction-induced vibrations are prevalent in many fields, and are often linked to unwanted noise, vibration and harshness (NVH) events Leine et al. (1998). One widely researched example is the NVH behavior of automotive braking systems, e.g. high-frequency squeal Hamabe et al. (1999); Van de Vrande et al. (1999); Hoffmann et al. (2002); Popp (2005); Ostermeyer (2008, 2010); Wernitz and Hoffmann (2012). Of the many phenomena related to brake squeal, synchronized vibrations in the friction contact have been identified as one potential triggering mechanism Ostermeyer (2010).

Measurement-based investigations can offer insights into such synchronized vibrations. They reveal isolated information regarding the behavior of a particular complete test system under specific conditions, sometimes leading to new insights into trends within limited parameter ranges. In order to better understand the fundamental tribological phenomena within the contact area, approaches combining theory and simulations are often employed.

The *Abstract Cellular Automaton* (ACA) simulation program is used to simulate the entire tribological contact between a brake pad and disc Ostermeyer and Merlis (2018). Based on patch theory Ostermeyer (2001), the ACA simulates the development, destruction, and further dynamics of contact structures in the boundary layer. This enables an efficient, targeted analysis of the elements of the brake system that predominantly influence the global tribological behavior, while also allocating appropriate computational resources to further system components Ostermeyer and Merlis (2018).

The current work presents studies performed using the ACA towards analyzing the high-frequency (HF, on the order of 1 kHz and above) vibration states that occur in the friction contact of automotive brakes, as discussed for example in Wernitz and Hoffmann (2012); Ostermeyer (2010); Otto and Ostermeyer (2018). To this end, the vibrations of the contact patches are modeled and simulated using this tool.

A particular focus is set on the synchronized stick-slip-like motion of these contact areas along the direction of friction. While synchronization has already been the subject of research in various contexts Lachaux et al. (1999); Sinkkonen et al. (1995); Palva et al. (2005); Slagter et al. (2009); Stefański et al. (2007); Perlikowski et al. (2008), this work aims to analyze synchronized friction-induced vibrations with the complexity of an entire pad-disc contact. The authors presuppose that appreciable synchronized vibrations of the patches can occur in the tribological boundary layer, and that the resulting HF oscillatory character of the global coefficient of friction can trigger undesired NVH events in automotive brake systems, as supported by Ostermeyer (2008); Lee and Gesch (2009). For example, synchronously oscillating patches may excite vibrations in the brake disc, which can then generate audible pressure fluctuations. Under these assumptions, such synchronization states are detected and characterized in this work. The stability of these phenomena is not considered within the scope of this work.

First, the simulation program and the associated models used in these investigations are presented and explained. A full pad-disc contact is simulated on multiple time scales, modeling both the development and HF vibrations of contact structures. A friction model is chosen which induces relevant vibrations, enabling a simple numerical investigation of emergent synchronization states. A new means of quantifying the synchronization of many oscillating bodies is then introduced. Results of the simulative studies and analyses are then presented. Finally, the work is summarized and potential steps for further advancements are suggested.

* E-mail address: gp.ostermeyer@tu-braunschweig.de
doi: 10.24352/UB.OVGU-2019-025

2 Materials and Methods

2.1 Simulating Vibrations in Tribological Contacts

2.1.1 Simulation Program

The ACA efficiently simulates the tribological processes in brake contacts by concentrating the computational effort on the patches, and minimizing calculations of the surrounding surfaces Ostermeyer and Merlis (2015, 2018). By assigning each patch to an entry on a linked list, the ACA is capable of rapidly simulating the tribological behavior of the contact between a brake disc and an entire brake pad.
The fundamental functionality of the ACA on the long timescale (LF: $\Delta t = 0.01$ s) has been validated in previous works Ostermeyer and Merlis (2015, 2018). The ACA simulation program is capable of producing results comparable to those attained using classical, grid-based cellular automata Ostermeyer and Merlis (2015). It has also been shown that the ACA generates complex macroscopic friction behaviors with simple local friction assumptions. For example, thermoelastic instabilities have been successfully simulated with Coulomb friction implemented at all contact surfaces Ostermeyer and Merlis (2015, 2018), with good correspondence to documented measurement results Lee and Barber (1994); Severin and Dörsch (2001). The ACA enables explicit comparisons of the unique interactions between the dynamics of the effective friction radius, the coefficient of friction, the global braking torque, and the patches in the tribological interface Ostermeyer and Merlis (2018).
This work focuses on specialized investigations of patch vibration dynamics in the tribological contact. This is a known phenomenon, measured for example in Wernitz and Hoffmann (2012); Otto and Ostermeyer (2018). The ACA simulations will provide an aid towards investigating relevant synchronization states in detail. Within the scope of this work, this will be carried out on a strictly theoretical level for developing analysis methods. Physical measurements for motivating and verifying the specifics of the processes and phenomena will be the subject of future research.

2.1.2 Simulation Model

The simulations of friction-induced vibrations in the tribological boundary layer presented in this paper are based on the fundamental model of brake friction introduced in Ostermeyer (2001). The theory that contact plateaus, or "patches," are primarily responsible for the global friction behavior of brake systems has been the basis of several cellular automaton-based simulations of the associated boundary layer Ostermeyer and Müller (2008); Wahlström (2014). These programs focused on simulating the life cycles of several patches, and the resulting effects on the tribological system. Furthermore, in order to simulate friction-induced vibrations in brake systems, simplified lumped-mass models representing the contact plateaus (or micro contacts) and the associated elastic couplings have been implemented Ostermeyer (2008, 2010). These simulations typically assume a given patch coverage state in the boundary layer, and compute the vibrations within an area that is much smaller than that of a full-scale brake pad. The ACA is capable of combining these two approaches: the development of a patch coverage state is simulated for the entire contact between a brake pad and disc, and the resulting friction-induced vibrations are then computed.
As shown in Figure 1, a lumped element model based on the one presented in Ostermeyer (2010) is implemented, enabling analyses of the patches' vibrational behavior Ostermeyer and Merlis (2018).

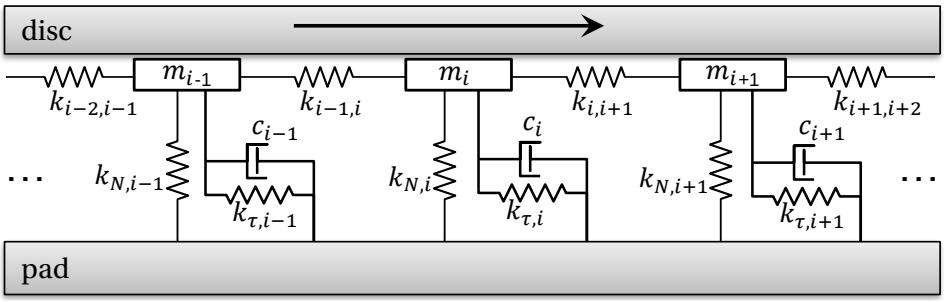

Fig. 1: Simplified Schematic Diagram of the Elastic Coupling Model for Patches P_{i-1}, P_i, and P_{i+1} (Potential Coupling between P_{i-1} and P_{i+1} not shown, reprinted from Ostermeyer and Merlis (2018))

The effective mass m_i of a given oscillating body encompasses the masses of the corresponding patch P_i and a small volume of the surrounding pad matrix material. This mass is approximated as proportional to the patch volume, typically within 0.75–3.0 mg. The effective spring stiffnesses in the normal (N) and tangential (T) directions are calculated as functions of the patch contact area A according to Eq. 1, Eq. 2, and Eq. 3

$$k_{i,N} = K_N \sqrt{A_i} \tag{1}$$

$$k_{i,T} = K_T \sqrt{A_i} \tag{2}$$

$$k_{i,j} = K_C \frac{\sqrt{A_i \cdot A_j}}{D_{0,ij}}, \tag{3}$$

with $K_N = 2.39 \cdot 10^9\,\mathrm{N\,m^{-2}}$, $K_T = 1.87 \cdot 10^9\,\mathrm{N\,m^{-2}}$, and $K_C = 7.96 \cdot 10^8\,\mathrm{N\,m^{-2}}$ based on the results of finite element method (FEM) parameter studies. The elastic coupling between two patches is neglected if the unloaded distance between them $D_{0,ij}$ exceeds 5 mm Ostermeyer and Merlis (2018).

This spring stiffness model reflects the assumption that the patches are cylindrical in form. This is consistent with the overarching modeling approach of the ACA, in which the shape of the patches is not taken into account. This approximation is considered adequate as a first approach. In the future, a more detailed spring stiffness model may be implemented, e.g. based on the Boussinesq-Cerruti solution Love (1892); Peng and Zhou (2012).

In the ACA, patches are elastically coupled to all neighboring patches within the aforementioned unloaded distance. Therefore, a spring $k_{i-1,i+1}$ could also be in effect, directly coupling patch P_{i-1} with P_{i+1} (not shown in Figure 1). This elastic coupling is implemented based on the proximity of neighboring patches along the two-dimensional boundary layer. The forces and displacements in the radial direction, perpendicular to the local relative motion of the disc, are neglected. Thus, the complete three-dimensional system is used towards establishing the conditions of the elastic coupling between patches, and the dynamic vibration analysis is implemented based on the two-dimensional system shown in Figure 1, neglecting vibrational effects and explicit couplings between patches in the normal direction Ostermeyer and Merlis (2018). For a simple consideration of a slightly damped system, the damping constants c are selected such that the damping ratio of each patch is equal to 10^{-6}. Patches are assumed to be small relative to the brake disc; the disc's rotation effectively results in a translational excitation on the patches' surfaces.

In physical systems, vibrations in the contact can be induced via various phenomena, for example mode coupling and stick-slip. It is supposed that patches exhibit micro stick-slip behavior as a result of a constant static friction coefficient which is greater than that of kinetic friction. This "true" stick-slip behavior is numerically challenging to implement on the scale of a full pad with hundreds or thousands of patches. To simulate this in a numerically sound and computationally achievable way, friction between the patches and disc is approximated with a falling friction curve over sliding speed, as shown in Eq. 4 and Figure 2. The macroscopic friction behavior of brake systems can exhibit both positive and negative gradients with respect to sliding speed, depending on the pad. A negative friction gradient is not the cause of the NVH behavior currently associated with mode coupling phenomena. The friction rule used here (Figure 2) has been selected as a simple means for inducing vibrations in the contact, aiding in the current investigations of local synchronization states in the boundary layer.

$$\mu_p = \left| \frac{M}{\pi} \cdot \arctan\left(200 \cdot v_p\right) \cdot \left(\frac{1}{0.25 \cdot |v_p| + 1} + 1 \right) \right| \tag{4}$$

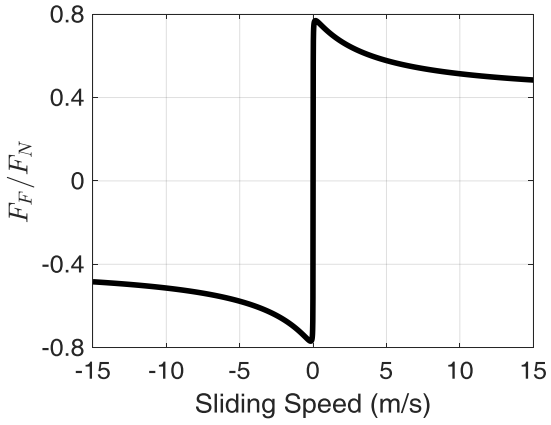

Fig. 2: Friction Rule Implemented at Patch-Disc Contacts (evaluated at $M = 0.8$)

This friction rule is designed such that the ratio F_F/F_N is differentiable at all sliding speeds, preventing numerical difficulties as the relative velocity passes zero, as implemented in Ostermeyer (2008). It is chosen in order to impose a friction curve that slowly decreases with increasing sliding speeds within the range of the average relative velocity between pad and disc for a given simulation. This condition is used for convenience, ensuring that the system is capable of exhibiting local stick-slip-like friction-induced vibrations of the contact plateaus. Thus the goal of characterizing synchronization states can be approached. This may ultimately be applied to various types of synchronized vibrations, regardless of the driving mechanism or friction assumptions.

For simplicity, Coulomb friction is implemented at points of contact between the disc and the brake pad *matrix material*, encompassing all parts of the pad's surface where patches are not present. For these pad-disc contacts, $\mu_{pad} = 0.3$ is implemented. For $M = 0.8$, the friction rule implemented for the patches asymptotically approaches $\mu_p = 0.4$ at its extrema, ensuring a nonzero difference between the friction coefficients of the pad-disc and patch-disc interfaces.

The global friction coefficient is computed as the ratio between the total sum of all local friction forces and the total sum of all local normal forces, as described in Ostermeyer and Merlis (2018). When there is no contact between the pad and disc, e.g. during pauses between brake applications, the convention $\mu = 0$ is established for the output data. In this work, the effective friction

radius is defined as the radial component of the centroid of the friction forces, and the friction torque is computed as the sum of all local friction moments about the disc's center.

2.1.3 The Multi-Timescale Problem

The time constants of the tribological processes simulated in the ACA span several orders of magnitude. To account for this, the ACA functionality is carried out on two distinct timescales. On the slower "low-frequency" (LF) timescale, processes such as patch dynamics, thermal effects, wear, and normal force distribution are computed with a time step $\Delta t = 0.01$ s. As high-frequency (HF) patch vibrations cannot be resolved on this timescale, they are computed on the HF timescale, with adaptive time steps on the order of $\Delta t \sim 10^{-9}$ s. During HF simulations, all LF processes are neglected and the associated simulation parameters are held constant. In *multi-timescale* simulations, the state of the ACA is saved at one or several instants during an LF simulation, and then processed on the HF timescale. Such simulations enable investigations e.g. into the effects of load history on friction-induced vibrations and synchronization. *Stand-alone* HF simulations can also be carried out, in which a pre-defined patch coverage state is assumed. This is useful for investigating specialized patch distribution cases.

The LF effects of patch dynamics on the global tribological behavior have often been discussed in the literature (e.g. Ostermeyer (2001)), and the corresponding interdependencies within the ACA are presented in Ostermeyer and Merlis (2018). The analogous HF interdependencies are summarized in Figure 3.

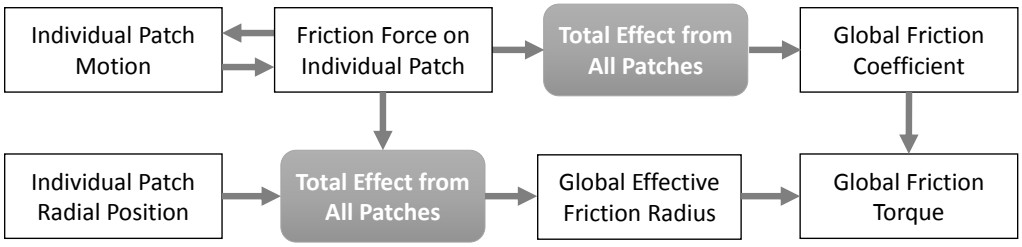

Fig. 3: General HF Interdependencies of Crucial Dynamics in the Tribological Boundary Layer

2.2 Quantifying the Synchronous Vibrations of Patches

In recent history, techniques for detecting and quantifying synchronized signals have been developed and widely employed in the fields of neuroscience. Tools such as phase-locking statistics Lachaux et al. (1999) and the phase-locking factor Sinkkonen et al. (1995); Palva et al. (2005); Slagter et al. (2009) primarily seek to determine the phase similarities of short, pulse-like oscillatory signals. By detecting the synchronicity of all signals relative to one another, these tools have provided the means for much progress in the associated fields.

The synchronization patterns of patches, however, are not necessarily uniform throughout the tribological interface. It is possible for multiple groups, or "islands," of patches to exhibit local synchronization behaviors. Depending on the sizes and distributions of these groups, relevant NVH events may still be excited by such synchronization states. This may be the case even if the synchronization islands have varying phase shifts and degrees of synchronicity in relation to one another. Some low-frequency global stick-slip behaviors may also be related to these HF synchronization islands. In order to adequately detect and quantify HF synchronization states of patches, an appropriate analysis tool is needed which is sensitive to such scenarios. Therefore, the aforementioned phase-locking techniques are not appropriate for the current work. While work has also been carried out towards analyzing nonuniform synchronization states, these are often developed for highly specified systems with a limited number of oscillators Stefański et al. (2007); Perlikowski et al. (2008).

The *Synchronization Index* $S(f)$ is introduced as a scalar value that seeks to quantify the synchronization state in the global contact area of an entire brake pad, encompassing many oscillating bodies. To this end, the motions of all patches are analyzed in the frequency domain via a Fourier analysis. The Synchronization Index for a given frequency is computed based an ABC Analysis Chu and Chu (1987); Partovi and Burton (1993) (also, Selective Inventory Control) of the phase angles of all patches vibrating at that frequency. It is developed based on the hypothesis that one or multiple highly prevalent phase angles can be indicative of synchronization. This is mathematically elucidated in the following description, in which a single arbitrary frequency is considered. In practice, the analysis is carried out over a wide band of discrete frequency bins.

The number of patches with an oscillation component at the given frequency are represented by Φ. The Synchronization Index is undefined for all frequencies at which fewer than two patches oscillate ($\Phi < 2$). A set of 180 evenly spaced phase bins are defined within the range $[-\pi, \pi)$. Each bin is assigned a value G equal to the number of patches whose phase shift is within the bin's range. A pseudo continuous consideration of similar phase shifts is achieved through applying a weighted moving average filter to the phase bins, using a Gaussian weighting function with a standard deviation of $2\pi/180$ rad and a window size of 3 bins. The processed bin data is then arranged in descending order, such that $G_1 \geq G_2 \geq G_3 \geq \cdots \geq G_{180}$.

The A group is separated from the B group at bin n_{AB}, defined as the minimum value satisfying

$$\sum_{i=1}^{n_{AB}} G_i \geq \tau_{AB} \cdot \Phi \,, \tag{5}$$

with the threshold value τ_{AB}. This is implemented with element precision rather than bin precision, i.e. n_{AB} is not necessarily integer value. The corresponding contribution S_{AB} to the Synchronization Index is computed as

$$S_{AB} = \frac{n_{AB,max} - n_{AB}}{n_{AB,max} - n_{AB,min}} \,. \tag{6}$$

Here, $n_{AB,max}$ is the theoretical maximum value of n_{AB} (worst case) for a given value of τ_{AB}, and $n_{AB,min}$ is the theoretical minimum value of n_{AB} (best case) for a given τ_{AB}, taking into account the effects of the weighted moving average filter.
An analogous computation is carried out for distinguishing the B and C groups:

$$\sum_{i=1}^{n_{BC}} G_i \geq \tau_{BC} \cdot \Phi \,, \tag{7}$$

$$S_{BC} = \frac{n_{BC,max} - n_{BC}}{n_{BC,max} - n_{BC,min}} \,. \tag{8}$$

The resulting Synchronization Index is computed as

$$S = S_{AB} \cdot w + S_{BC} \cdot (1 - w) \,, \tag{9}$$

with the weighting factor w. The result is a frequency dependent quantity which varies between 0 and 1, with lesser values resulting from more stochastic distributions of phase shifts, indicating poor synchronization, and greater values resulting from nearly identical phase shifts, indicating substantial synchronization. The functionality of the Synchronization Index is illustrated through theoretical minimal examples in the Appendix. For the preliminary analyses shown in this work, the parameter values $\tau_{AB} = 0.5$, $\tau_{BC} = 0.55$, and $w = 0.9$ are chosen.
The Synchronization Index is developed as a practical tool for the comparison of HF synchronization states. It is not intended to perfectly encapsulate all synchronization phenomena. It was designed to detect characteristic synchronization "islands" which often come about in relevant HF vibration scenarios. While there are certainly limit cases for which the Synchronization Index yields counterintuitive results (perhaps in the case of LF Schallamach waves), it is considered a useful tool to aid the interpretation of the results relevant to the current work.

3 Results

As described in Section 2.1.3, the ACA can be used to implement various types of studies towards analyzing friction-induced vibrations in tribological contacts. The results presented in this section are selected to exemplify various characteristic effects which are observable under particular simulation (or braking) conditions. These studies are aimed towards studying synchronized HF vibrations. Certain characteristic behaviors are investigated and identified towards inferring whether an NVH event may potentially be triggered, as discussed in Lee and Gesch (2009); Ostermeyer (2010). No statement is made towards the longevity of such behaviors based on these simulation results. To make such a claim would require HF simulations to be carried out over many simulation seconds, simultaneously accounting for all relevant LF phenomena. The results presented here emphasize the qualitative phenomena and dynamics rather than exact quantitative values.

3.1 Stand-Alone HF Simulations with Constant Parameters

First, stand-alone HF simulation results are presented in which predefined patch coverage states were implemented. The primary purpose of these initial studies is to demonstrate that established behaviors observed in scaled-down systems (as presented in Ostermeyer (2008, 2010)) can also be found in simulations of a full-scale brake pad. A parameter study was carried out over patch area and the friction model, as summarized in Table 1. In each study HF_{1-4}, 1758 patches were simulated in the contact

	$A_{p,mean} \approx 0.05$ mm^2	$A_{p,mean} \approx 1.25$ mm^2
$M = 0.8$	HF_1	HF_2
$M = 0.4$	HF_3	HF_4

Tab. 1: Stand-Alone HF Parameter Study Names

and the average sliding speed 10 m s^{-1} was implemented (corresponding to a vehicle speed of about 84 km h^{-1}). The patch areas were pseudorandomly selected from uniform distributions. For the simulations with smaller average patch sizes ($HF_{1,3}$), the areas were selected within $0.02 \leq A_p \leq 0.08$ mm^2. The simulations with larger patches ($HF_{2,4}$) employed areas based on $0.50 \leq A_p \leq 2.00$ mm^2. To heighten the effects of the patches' motion, the normal load was selected such that all patches were in contact with the disc, with the contact between the pad matrix and the disc minimized. This resulted in a surface pressure of about 44 kPa (brake line pressure about 1.32 bar, $F_N = 487.2$ N) for $HF_{1,3}$, and for $HF_{2,4}$ a surface pressure of about 1108 kPa (brake line pressure about 33.2 bar, $F_N = 12.37$ kN).
The time domain results from studies HF_1 and HF_2 are presented in Figures 4–5 and 6–7, respectively. In Figures 4 and 6 (top), the synchronization behavior of the patches is clearly observable. As the patches vibrate along the arc of the disc's rotation, the

instantaneous direction of the patches' motion is indicated through a color coding scheme. Red patches are moving with the local motion of the disc, and blue patches are moving opposite to the disc's motion.

It can be observed that macroscopic groups of patches move together in the same direction as their neighbors. These synchronized islands exhibit periodic behaviors that correspond well to the global friction dynamics. Figures 5 and 7 show how the friction coefficient's dynamics relate to further global system dynamics. The effect of patch vibrations on the global friction torque is expected to be more pronounced in the case of radially imbalanced synchronization patterns. Such cases should also be reflected through the effective friction radius. In these figures, an impression of the patches' motions is given through the sum of all patch velocities. Here, the total of all absolute velocities in reference to the stationary brake pad is used, not the total sliding speeds.

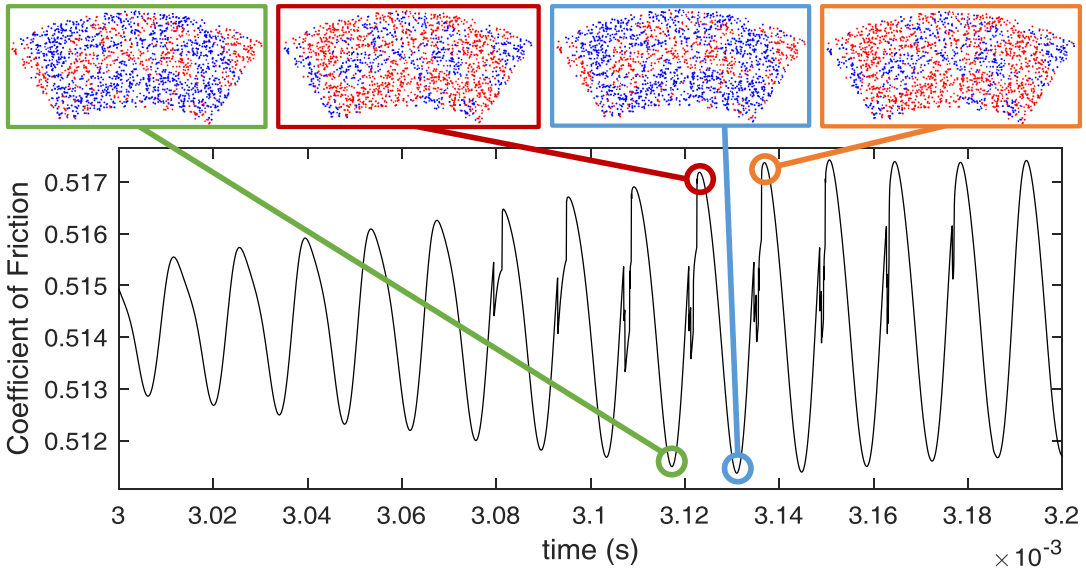

Fig. 4: HF_1: Influence of Patch Motion on Global Friction Behavior. (red) patches are moving with the local motion of the disc, (blue) patches are moving opposite **to** the disc's motion.

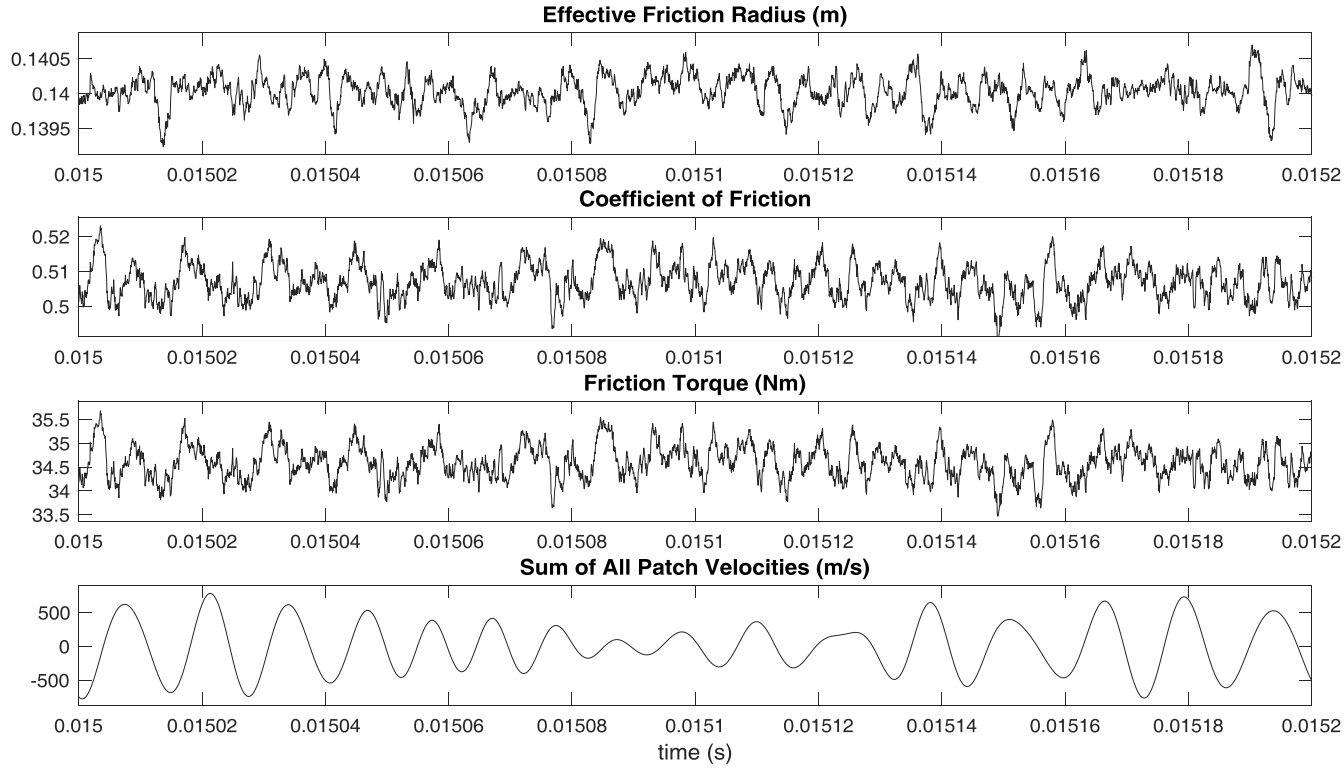

Fig. 5: HF_1: Global Tribological Data

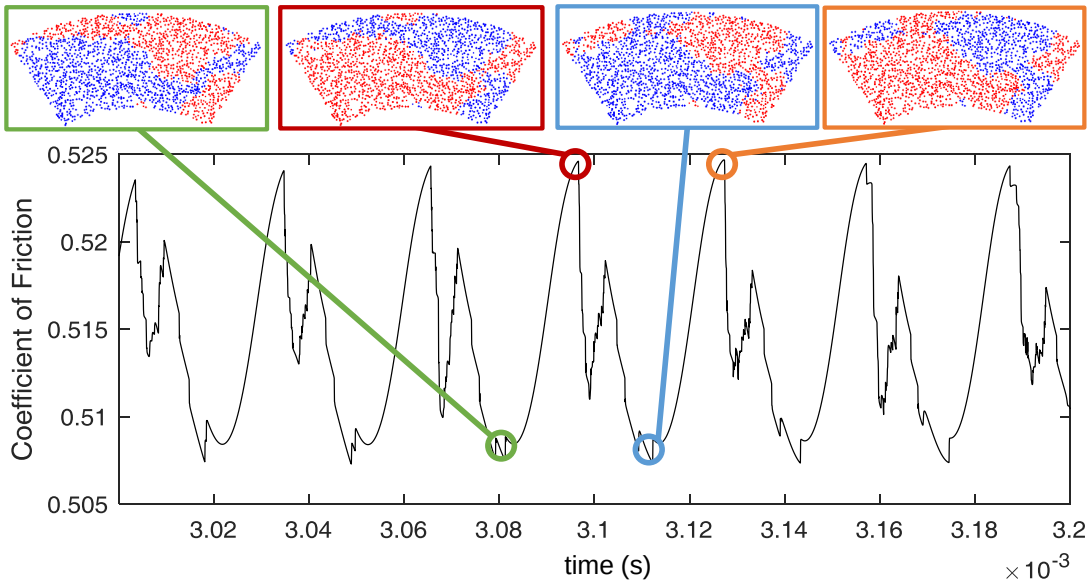

Fig. 6: HF_2: Influence of Patch Motion on Global Friction Behavior. (red) patches are moving with the local motion of the disc, (blue) patches are moving opposite to the disc's motion.

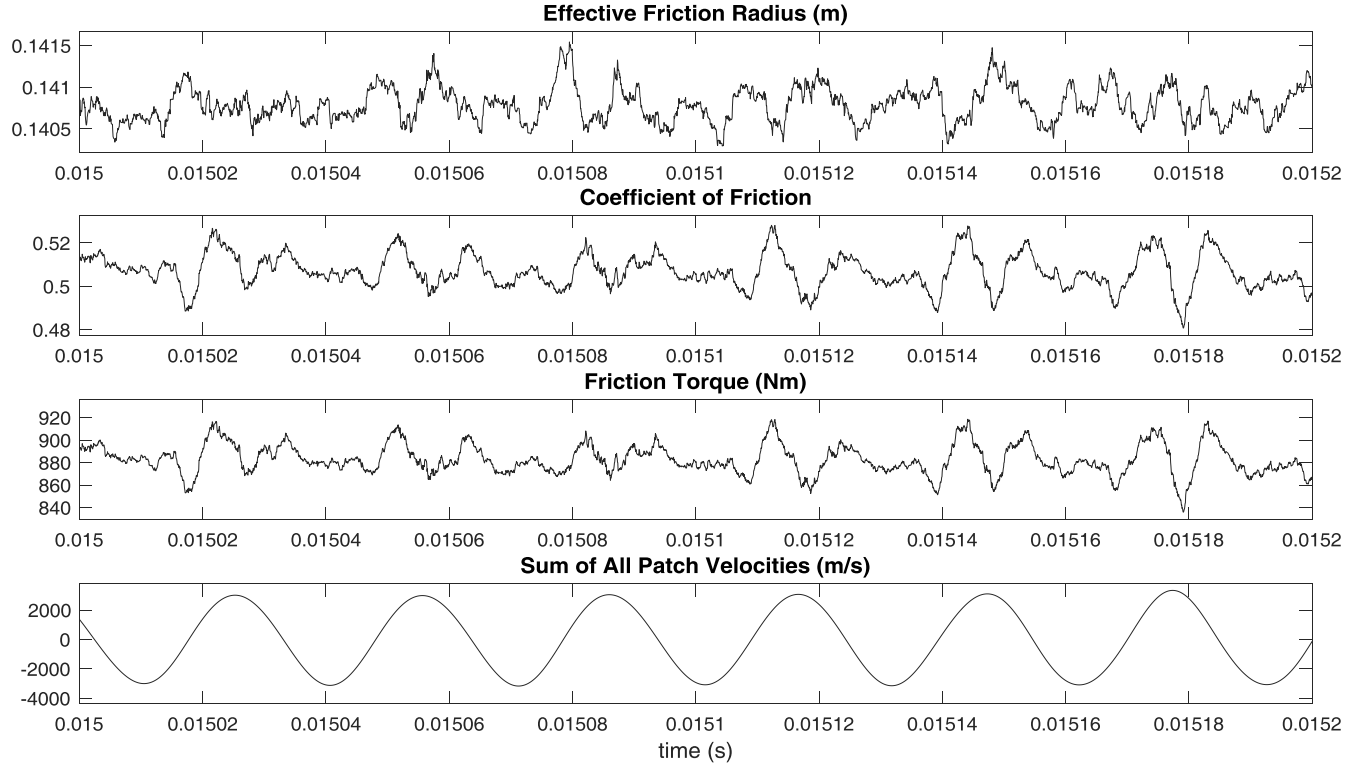

Fig. 7: HF_2: Global Tribological Data

As reflected in Eq. 3, the increase in patch area from HF_1 to HF_2 causes a stiffening of the coupling springs, yielding larger and better-defined synchronization patterns.

The frequency spectra of these global tribological results are shown in Figure 8 for all studies HF_{1-4}. Each amplitude spectrum is presented as a dimensionless quantity through normalization with respect to the time signal's DC offset. All Fourier analyses shown in this work were preprocessed with a Hann window. The corresponding Synchronization Index results are shown in Figure 9. At each relevant frequency bin, the *quality* of synchronization is represented through the Synchronization Index value, and the *prevalence* of the synchronization corresponds to the number of patches with substantial oscillation amplitudes (Φ from Section 2.2).

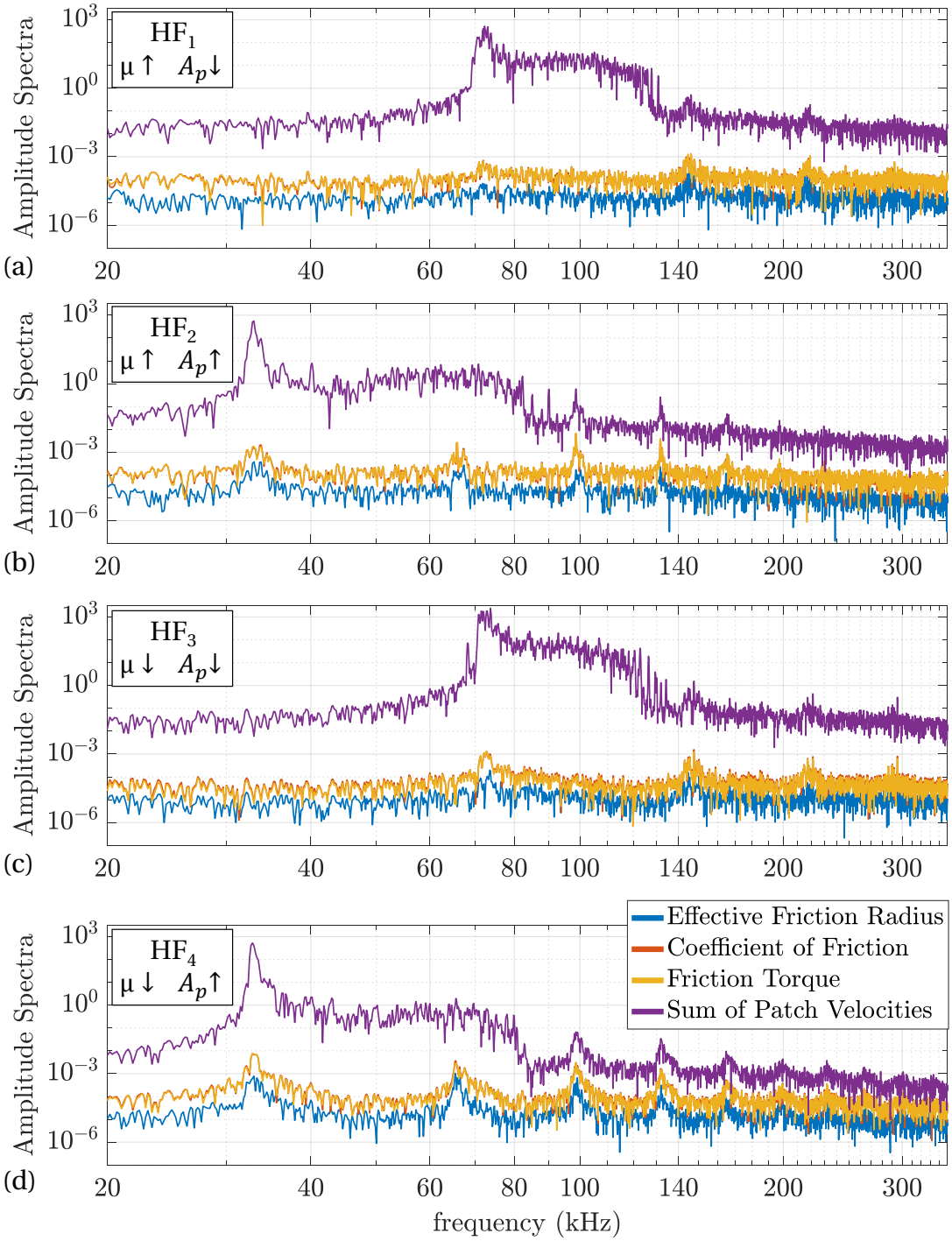

Fig. 8: Frequency Spectra of Stand-Alone Simulations. All results normalized to the mean value of the raw data. Note that the coefficient of friction and the friction torque exhibit very similar normalized behaviors; the corresponding curves are nearly completely overlapping.

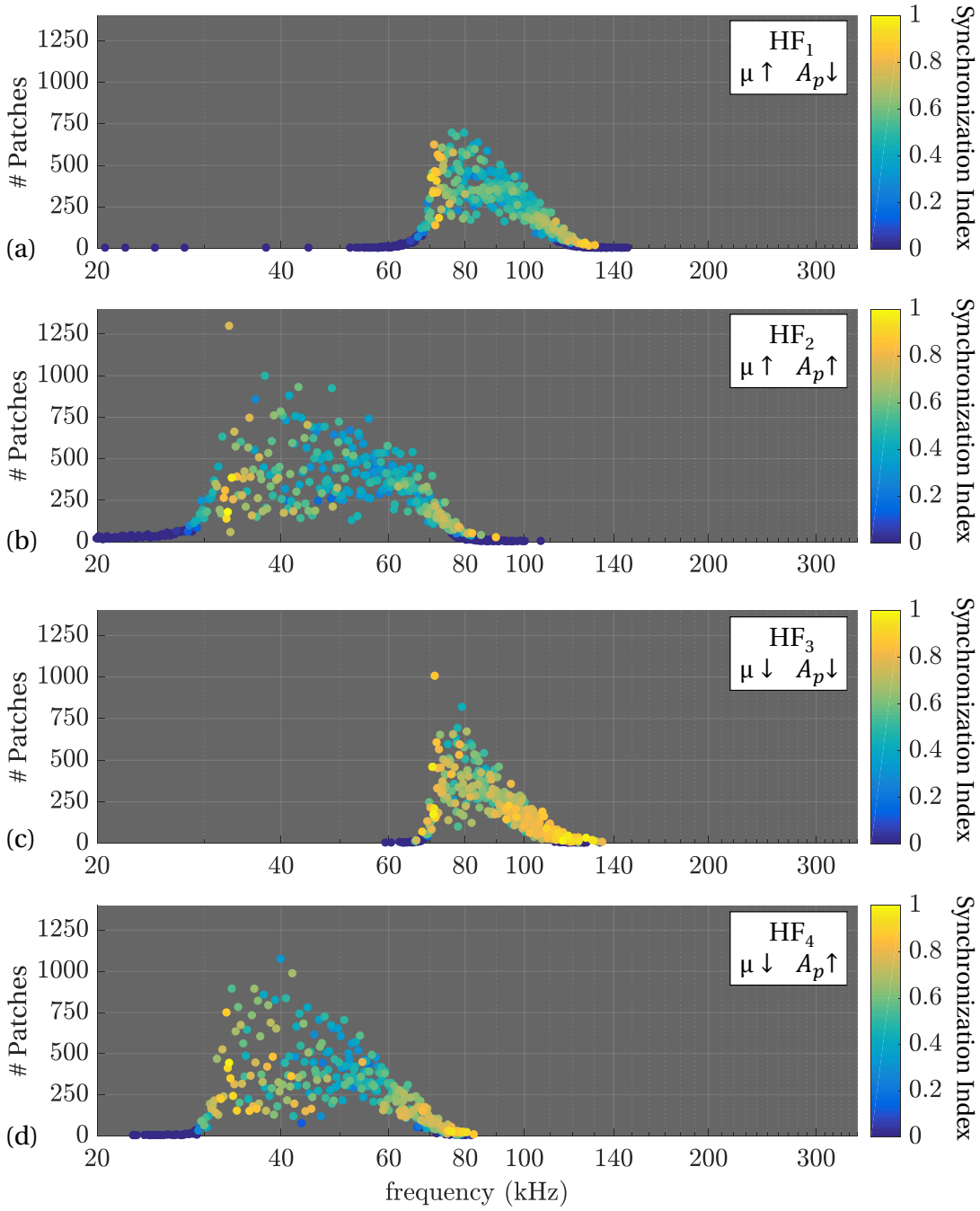

Fig. 9: Synchronization Index Results of Stand-Alone Simulations

In Figure 8, similar characteristic peaks of the global friction coefficient, friction torque, and effective friction radius are revealed, most of which are also present in the velocity spectra. The first peak of each velocity spectrum (around 73 kHz for HF_1 and HF_3, and around 32.8 kHz for HF_2 and HF_4) is significantly more pronounced than the other output quantities. In all four studies, these frequency peaks are followed by broad-band plateaus that are not observed in the other global outputs. These initial peaks and plateaus correspond well to the Synchronization Index results. It can be inferred that the corresponding friction peaks are caused by significant patch synchronization.

There are many peaks at higher frequencies in Figure 8 that do not correspond to any Synchronization Index results. These peaks are likely caused by the motions of individual, highly influential patches, and may partially be artifacts of the numerical Fourier transform.

Considering the effects of increased patch areas, the peaks of the HF_2 and HF_4 spectra have increased amplitudes, are narrower, and occur at lower frequencies than those from HF_1 and HF_3, respectively. Based on the implemented spring stiffness models, the approximate relationship between an isolated patch's natural frequency and its area $f_p \propto A_p^{-\frac{1}{4}}$ is expected. This is in good agreement with the frequency shifts observed in the spectral results and the Synchronization Indices.

The increase in patch area leads to more "spread out" Synchronization Index results, generally exhibiting increased prevalence values. Comparing HF_1 and HF_2, this size increase does not appear to significantly affect the synchronization quality. The synchronization quality increased significantly as a result of decreasing the friction coefficient for smaller patches. This effect is not as substantial, however, for the larger patches. It is a reasonable result that lower friction coefficients yield higher valued Synchronization Indices, as the friction forces are decreased relative to the forces of the coupling springs. As the patch areas

influence both the coupling forces and the normal forces, the effect of patch area on the patch synchronization is nontrivial and may be highly sensitive to certain relevant parameters.

Of these four studies, HF_4 exhibits the best agreement between the Synchronization Index results and the friction frequency spectrum. This may suggest an increased propensity for the triggering of an NVH event.

First interpretations of the combined effects of patch size and local friction values can also be made. Taking HF_1 as a reference, the HF_4 results can be interpreted as a combination of the changes observed in HF_2 and HF_3. For example, the Synchronization Index results of HF_4 are more spread out than HF_1 (influence of increased patch size), and are greater in value, especially at higher frequencies (influence of decreased friction coefficient).

3.2 Stand-Alone HF Simulation with Varying Patch Area

To gain further insights into the effects of patch area on the global friction response, a specialized study was carried out with nonconstant patch sizes. A patch coverage state comparable to that of HF_1 was generated at the start of the simulation. The patch areas were then gradually increased throughout the simulation once every 202 time steps, as indicated in Eq. 10

$$A_{p,t+\Delta t_{202}} = A_{p,t} + 10^{-6} \cdot \sqrt{A_{p,t}} \; . \tag{10}$$

This growth procedure was selected such that the final patch area distribution approximates that of HF_2 for a simulation about as long as HF_1. The simulation parameters were identical to HF_1, with the exception of normal pressure. The normal load from HF_2 was implemented to ensure that all patches maintain contact with the disc through the end of the simulation.

This is a theoretical investigation towards gaining preliminary insights into the system's transient response under varying conditions. It is not intended to reflect realistic patch growth rates.

Due to the chosen loading and patch area conditions, contacts between the pad matrix and the disc have a dominating influence on the global friction behavior at the start of this simulation. As the patches grow their effective spring stiffnesses increase, causing the patches to carry an increasing portion of the normal load. By the end of the simulation, the friction behavior is completely dominated by patch-disc contacts. This results in the development of the friction coefficient shown in Figures 10 and 11. The time domain global friction coefficient is shown alongside a corresponding short-time Fourier transform (STFT) in Figure 10. In Figure 11 a continuous wavelet transform (CWT) of the same signal is shown, offering a continuous impression of the development of the friction coefficient's frequency signature. Here, the decreasing frequencies of the characteristic peaks resulting from the increasing patch sizes are clearer to observe.

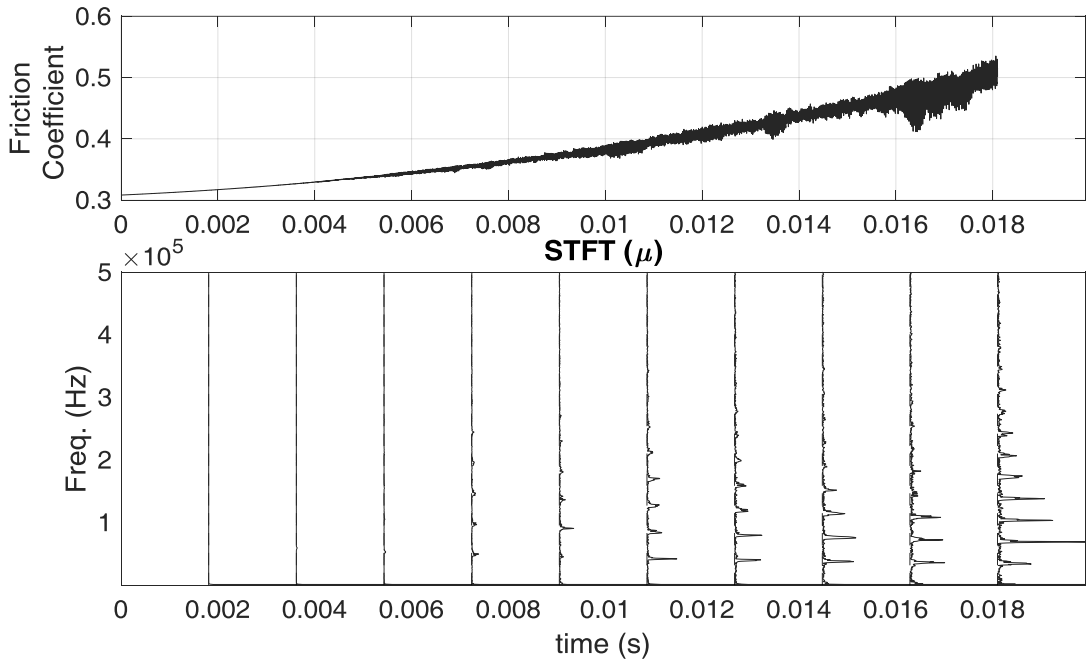

Fig. 10: (top) Time Domain Signal of the Global Friction Coefficient, (bottom) STFT Development of Dominant Peaks in the Frequency Signature of the Coefficient of Friction. STFT results are truncated below 10 Hz and then normalized to the maximum amplitde of about 0.004 (corresponding to the largest peak around 69.1 kHz)

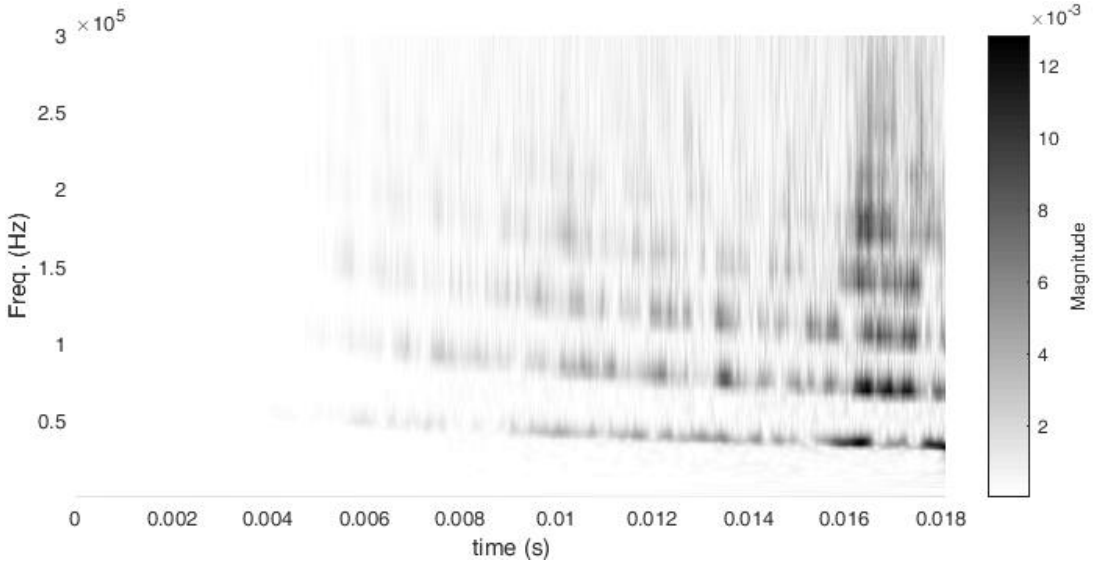

Fig. 11: CWT of the Global Friction Coefficient Resulting from Friction-Induced Vibrations and Patch Growth

As observed in the time domain results (Figure 10, top), the DC offset and the slow increase of the friction coefficient each have significantly greater magnitudes than the signal's HF oscillations. To aid in the interpretation of the HF results, the results at frequencies less than 10 Hz are omitted from all frequency domain output plots.

In both the STFT and CWT results, the emergence of individual dominant frequencies can be observed. The development of frequency signatures from stochastic (low-amplitude oscillations over a wide frequency range) to periodic (one or multiple dominant frequencies) is a documented triggering mechanism of NVH in brake systems Ostermeyer (2010). It is also relevant to note that friction peaks at a given frequency may also contribute to the onset of perceivable NVH events at differing frequencies Nishiwaki and Yamamoto (2018). It can be inferred that in physical brake systems, the transition from a pad-disc dominated state to a patch-disc dominated state could be related to the triggering of squeal. The development of synchronization states in this type of study will be investigated in a future publication.

3.3 Multi-Timescale Study

A multi-timescale study was carried out to investigate realistic braking scenarios that can potentially lead to relevant synchronized vibrations. The normal load variation shown in Figure 12 was implemented on the LF timescale. Each application had a duration of 10 seconds, separated by 5 second long pauses. The constant sliding speed $v = 10$ m s^{-1} and the friction model's multiplicative factor $M = 0.8$ were implemented throughout this study. HF analyses were carried out using the system states at the start and end of each application. During the HF simulations the patches' areas were held constant.

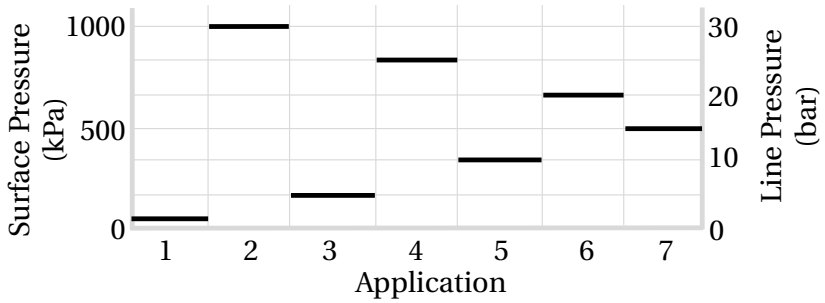

Fig. 12: Vibration Study Procedure, Based on the SAE 2521J Brake Squeal Module SAE International (2006)

The patch coverage states, global friction frequency spectra, and Synchronization Indices from a selection of the HF analysis results are presented in Figure 13.

Each point in the patch coverage state diagrams on left side of this figure represents a single patch. Based on a single simulation time step, the color coding of the instantaneous direction of motion of these patches offers a qualitative impression of the emergent synchronization patterns. While these patterns are not as clearly defined as those from the previous examples, a degree of local clustering can be observed. The results from the end of Application 3 (fourth row) indicate a correlation between this local clustering and the number of patches detected in the Synchronization Index analysis.

The friction coefficient oscillates with the greatest amplitudes during Application 3, in which a relatively low normal pressure was applied. The maximum amplitudes occurred at the beginning of this application, immediately following a high-load brake application. Here, the surface topography generated through Application 2 remains predominantly present, and is acted upon by the loading conditions of Application 3. Therefore, the friction-induced vibrations in the contact come about based on a patch coverage state similar to the one present at the end of Application 2, with excitation forces determined by the braking parameters

of Application 3. The increased oscillation amplitudes and individual high-valued Synchronization Index results (represented by yellow points) at the start of Application 3 may be of particular interest towards investigating brake squeal triggering mechanisms. At the end of Application 3, several medium to high valued Synchronization Index data points are present with increased prevalence (with regard to the number of associated patches). Some of these synchronization points are associated with amplitude peaks of the friction coefficient.

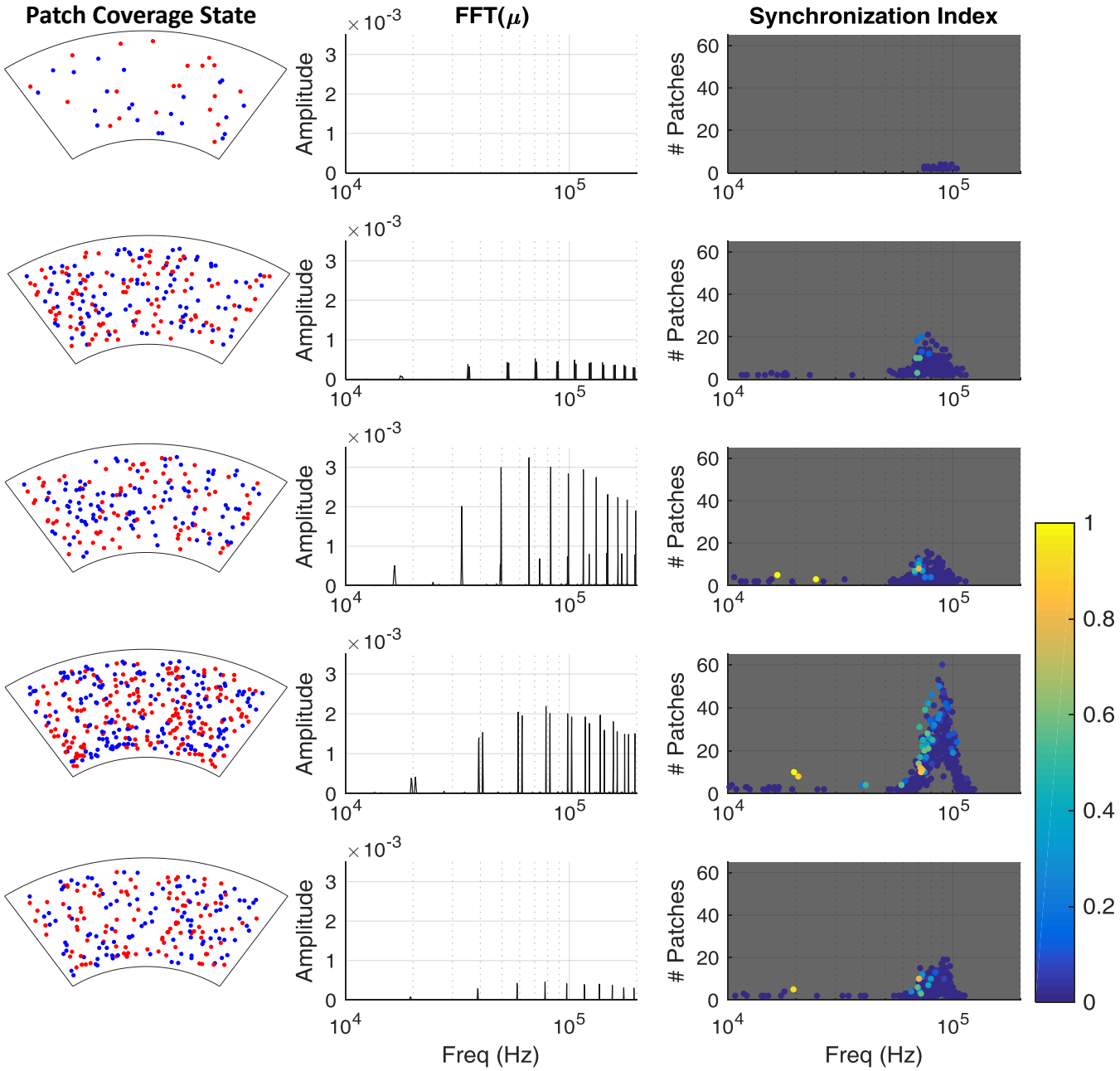

Fig. 13: Development of Multi-Timescale Results, **Top Row:** Beginning of Application 2, **Second Row:** End of Application 2, **Third Row:** Beginning of Application 3, **Fourth Row:** End of Application 3, **Bottom Row:** Beginning of Application 4. **Patch Coverage State:** (red) patches are moving with the local motion of the disc, (blue) patches are moving opposite **to** the disc's motion.

In general, significant interactions between the current braking parameters, load history, patch coverage state, synchronized vibrations, and global friction coefficient can be inferred. Distinct peaks in the friction coefficient's amplitude spectra occur at frequencies corresponding to both high-valued and highly prevalent Synchronization Indices. The friction spectral peaks that do not correspond to the Synchronization Index results are likely caused by the motion of individual, highly influential patches or numerical artifacts of the Fourier transform.

4 Discussion

Significant friction oscillations associated with low normal pressures can be the result of patch-disc contacts dominating the interactions. This was evidenced by the stand-alone HF simulation with varying patch area, and supported by the multi-timescale study. This may have implications for the triggering of brake squeal with low normal loads, particularly when there are many

patches present in the contact. This can come about if the low-load application causes the generation of many patches, or if a low-load brake application immediately follows an application in which several patches were generated. This is one example of the complex interactions between braking history and current braking parameters.

In general, the HF behavior at the beginning of a brake application is heavily influenced by the patch coverage state generated in the previous application by the previous set of braking parameters. This patch state is then excited with a new set of braking parameters. This new set of parameters may lead to an entirely different type of patch coverage state. In such a case, a variety of potential HF vibrational behaviors may come about as the new set of braking parameters excites a continuously developing patch state.

The exact influence of the Synchronization Index value, prevalence, and friction oscillation amplitudes on the triggering of NVH are unclear, although it is suspected that all three of these have some effect. For improved understanding of these issues, the sizes and spatial distributions of synchronization groups should be examined in the frequency domain, and the associated results should be applied to FEM simulations of the bulk pad and disc components to determine the associated excited vibrational modes.

Verification measurements should also be carried out. The characteristic friction and synchronization behavior simulated within the range 20–80 kHz is in good agreement with the measurements presented in Otto and Ostermeyer (2018).

5 Conclusions

Synchronized high-frequency patch vibrations are assumed to trigger squealing in automotive braking systems. Towards an improved understanding of the influences on squealing, these synchronized vibrations have been investigated using the ACA with the complexity of an entire pad-disc contact. Through a simplified model, it has been demonstrated how the onset of such synchronized vibrations can plausibly come about as a result of the braking history and the current braking conditions. It was also shown that the transition from a friction state dominated by pad-disc contacts to one dominated by patch-disc contacts can cause spectral peaks of the friction coefficient, a known NVH triggering mechanism.

Various means of analyzing simulation results have been presented, including the Synchronization Index which quantifies the synchronization of multiple oscillating patches. First results suggest that both the value and prevalence of the Synchronization Index are related to peaks in the frequency spectrum of the global friction coefficient. The Synchronization Index is not sensitive, however, to the spatial distribution of these bodies. Future works will introduce a new tool towards imaging the vibrations of many bodies with a focus on emphasizing local synchronization groups. The Synchronization Index will be integrated into this visualization scheme for a more robust interpretation of synchronization states. In this work, a preliminary set of Synchronization Index analysis parameters was chosen. Future investigations should be carried out towards the optimization of these values.

The scope of the simulations shown in the present work was to establish that the ACA is capable of depicting high-frequency synchronized vibrations. The Synchronization Index was introduced as a tool towards evaluating the associated phenomena and testing hypotheses. As a first step, the potential of these tools was illustrated. In future investigations, the ACA and Synchronization Index results should be validated with measurements.

Many aspects of the link between NVH and the high-frequency vibrations shown here are still not understood, although measurements indicate a close connection. In this work, a tool has been developed that is intended to aid in the determination of these correlations. Future investigations will consider realistic, spatially-resolved normal stresses on the pad. Further mesoscopic time scales will be implemented, which can also describe the temporal stability of the synchronization states. The latter is certainly necessary for detecting the triggering of low-frequency NVH oscillations. Additionally, this tool will be used towards identifying macroscopically measurable dynamics of the coefficient of friction in connection with the “elementary” friction processes on the individual patches. Thus, the local friction curve can be any arbitrary function of the velocity, if the vibrations of the patches are generated via mode coupling effects.

Further works will focus on the implementation of the ACA towards studying the vibrational effects associated with start and stop braking events. There, the transition between static and kinetic friction will come into the focus on both global and local spatial scales.

Acknowledgement

This research did not receive any specific grant from funding agencies in the public, commercial, or not-for-profit sectors.

Appendix

The functionality of the Synchronization Index is illustrated here using minimal examples. Here, only one isolated frequency bin is considered. To aid the presentation of these examples, only 10 phase bins are used rather than the 180 which are implemented for the simulation results shown in this work. The effects of the weighted moving average filter are neglected here. The analysis parameters are selected as follows: $\Phi = 100$, $\tau_{AB} = 0.50$, $\tau_{BC} = 0.55$, $w = 0.9$.

The following four theoretical cases are presented:

1. *Complete synchronization*: All patches are perfectly synchronous with one another.
2. One highly synchronous group is present, comprised of 75 patches. The remaining 25 patches do not belong to this synchronization island.
3. Multiple (3) synchronization islands are present, containing a total of 75 patches. The remaining patches do not belong to any of these islands.

4. *Perfectly asynchronous*: The patches' vibrations yield a uniform distribution of phase shifts.

The phase angle distributions associated with these cases are presented in Table A.1 and Figure A.1.

Tab. A.1: Phase bin values for four theoretical synchronization scenarios. Bins are arranged in order of descending value.

Bin:	G_1	G_2	G_3	G_4	G_5	G_6	G_7	G_8	G_9	G_{10}
Case 1:	100	0	0	0	0	0	0	0	0	0
Case 2:	75	3	3	3	3	3	3	3	2	2
Case 3:	27	25	23	4	4	4	4	3	3	3
Case 4:	10	10	10	10	10	10	10	10	10	10

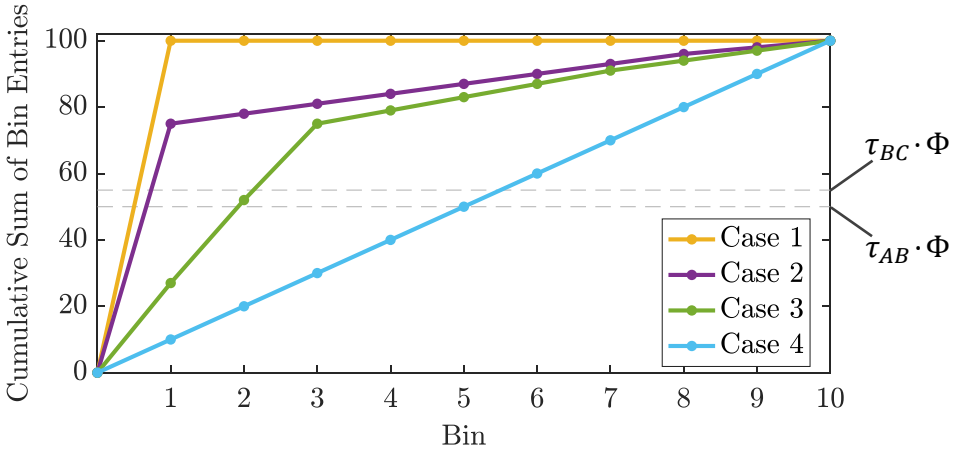

Fig. A.1: Phase bin values for four theoretical synchronization scenarios. The horizontal axis components of the intersection points between the cumulative sum curves and the dashed lines correspond to the respective values of n_{AB} and n_{BC}

Based on Eq. 5–Eq. 9, the corresponding Synchronization Analysis results are shown in Table A.2.

Tab. A.2: Synchronization Index results for the theoretical synchronization scenarios

Results:	n_{AB}	$n_{AB,max}$	$n_{AB,min}$	n_{BC}	$n_{BC,max}$	$n_{BC,min}$	S_{AB}	S_{BC}	S
Case 1:	0.500	5.000	0.500	0.550	5.500	0.550	1.000	1.000	1.000
Case 2:	0.667	5.000	0.500	0.733	5.500	0.550	0.963	0.963	0.963
Case 3:	1.920	5.000	0.500	2.130	5.500	0.550	0.684	0.681	0.684
Case 4:	5.000	5.000	0.500	5.500	5.500	0.550	0.000	0.000	0.00

These results illustrate the dependence of the Synchronization Index S on the synchronization state based on the associated phase angle distributions.

Nomenclature

Latin Symbols

A	Area (Surface, Contact, Cross Sectional)	(m^2)
c	Damping Coefficient	$(\mathrm{N\ s\ m}^{-1})$
D	Distance	(m)
f	Frequency	(Hz)
F	Force	(N)
G	Bin Value	(1)
k	Spring Stiffness	$(\mathrm{N\ m}^{-1})$
K	Constant Spring Stiffness Parameter	$(\mathrm{N\ m}^{-2})$
m	Mass	(kg)
M	Constant Factor of the Friction Model	(1)
n	Characteristic Result of ABC Analysis	(bins)
P	Patch	(1)
S	Synchronization Index	(1)
t	Time	(s)
v	Relative (Sliding) Velocity	$(\mathrm{m\ s}^{-1})$
w	Weighting Factor	(1)

Greek Symbols

Δt	Time Step	(s)
μ	Coefficient of Friction	(1)
Φ	Total Number of Patches	(Patches)
τ	Threshold Parameter	(1)

Symbols, Abbreviations, and Acronyms

$\propto$	Proportional to
$\sim$	On the order of
ACA	Abstract Cellular Automaton
CWT	Continuous Wavelet Transform
FEM	Finite Element Method
HF	High-Frequency
LF	Low-Frequency
NVH	Noise, Vibration, and Harshness
STFT	Short-Time Fourier Transform

Subscripts

AB	Distinguishing Group A from Group B
BC	Distinguishing Group B from Group C
C	Coupling
F	Friction
i, j	Arbitrary Index
max	Maximum Value
$mean$	Mean (Average) Value
min	Minimum Value
N	Normal
p	Patch
pad	Brake Pad Bulk Matrix Material
T	Tangential
0	Resting, Unloaded

Image Credits

Figure 1: Reprinted from Ostermeyer and Merlis (2018) (https://doi.org/10.3390/lubricants6020044) under the terms and conditions of the Creative Commons Attribution 4.0 International license (CC BY 4.0, http://creativecommons.org/licenses/by/4.0/)

References

Chao-Hsien Chu and Ying-Chan Chu. Computerized abc analysis: The basis for inventory management. *Computers & Industrial Engineering*, 13(1-4):66–70, 1987.

Tsutomu Hamabe, Ichiro Yamazaki, Kouji Yamada, Hiromichi Matsui, Shuuichi Nakagawa, and M Kawamura. Study of a method for reducing drum brake squeal. Technical report, SAE Technical Paper, 1999.

Norbert Hoffmann, Michael Fischer, Ralph Allgaier, and Lothar Gaul. A minimal model for studying properties of the mode-coupling type instability in friction induced oscillations. *Mechanics Research Communications*, 29(4):197–205, 2002.

Jean-Philippe Lachaux, Eugenio Rodriguez, Jacques Martinerie, and Francisco J Varela. Measuring phase synchrony in brain signals. *Human brain mapping*, 8(4):194–208, 1999.

Kwangjin Lee and JR Barber. An experimental investigation of frictionally-excited thermoelastic instability in automotive disk brakes under a drag brake application. *Journal of Tribology*, 116(3):409–414, 1994.

Li Lee and Earl Gesch. Discussions on squeal triggering mechanisms – a look beyond structural stability. In *SAE Technical Paper Series*. SAE International, 10 2009. doi: 10.4271/2009-01-3012. URL http://dx.doi.org/10.4271/2009-01-3012.

RI Leine, DH Van Campen, A De Kraker, and L Van Den Steen. Stick-slip vibrations induced by alternate friction models. *Nonlinear dynamics*, 16(1):41–54, 1998.

Augustus Edward Hough Love. *A Treatise on the Mathematical Theory of Elasticity*, volume 1. Cambridge University Press, 1892.

Masaaki Nishiwaki and Yukio Yamamoto. A study on trigger of small friction noise in disc brake squeal. Technical report, SAE Technical Paper, 2018.

G-P Ostermeyer. Friction and wear of brake systems. *Forschung im Ingenieurwesen*, 66:267–272, 2001.

G-P Ostermeyer. On tangential friction induced vibrations in brake systems. In *SAE International*, pages 101–111. 2008.

G-P Ostermeyer. Dynamic friction laws and their impact on friction induced vibrations. Technical report, SAE Technical Paper, 2010.

G-P Ostermeyer and Joshua Merlis. Effective simulation of the boundary layer of an entire brake pad. Number 2015-01-2664 in SAE Technical Paper, 2015. doi: 10.4271/2015-01-2664.

G-P Ostermeyer and M. Müller. New insights into the tribology of brake systems. *Proceedings of the Institution of Mechanical Engineers, Part D: Journal of Automobile Engineering*, 222(7):1167–1200, 2008. ISSN 0954-4070. doi: 10.1243/09544070JAUTO595.

Georg-Peter Ostermeyer and Joshua H. Merlis. Modeling the friction boundary layer of an entire brake pad with an abstract cellular automaton. *Lubricants*, 6(2), 2018. ISSN 2075-4442. doi: 10.3390/lubricants6020044. URL http://www.mdpi.com/2075-4442/6/2/44.

Johannes Otto and G-P Ostermeyer. Hochfrequente schwingungen in der reibgrenzschicht von bremssystemen. 15. Vibrometer Anwenderkonferenz. Polytec GmbH, 2018. (Publication Pending).

Satu Palva, Klaus Linkenkaer-Hansen, Risto Näätänen, and J Matias Palva. Early neural correlates of conscious somatosensory perception. *Journal of Neuroscience*, 25(21):5248–5258, 2005.

Fariborz Y Partovi and Jonathan Burton. Using the analytic hierarchy process for abc analysis. *International Journal of Operations & Production Management*, 13(9):29–44, 1993.

Yun Peng and Debao Zhou. Stress distributions due to a concentrated force on viscoelastic half-space. *Journal of Computations & Modelling*, 2(4):51–74, 2012.

Przemysław Perlikowski, Andrzej Stefański, and Tomasz Kapitaniak. 1:1 mode locking and generalized synchronization in mechanical oscillators. *Journal of Sound and Vibration*, 318(1-2):329–340, 2008.

K. Popp. Modelling and control of friction-induced vibrations. *Mathematical and Computer Modelling of Dynamical Systems*, 11(3):345–369, 09 2005. doi: 10.1080/13873950500076131. URL http://dx.doi.org/10.1080/13873950500076131.

SAE International. *SAE J2521-2006: Disc and drum brake dynamometer squeal noise matrix.*, 2006.

D Severin and S Dörsch. Friction mechanism in industrial brakes. *Wear*, 249(9):771–779, 2001.

J Sinkkonen, H Tiitinen, and R Näätänen. Gabor filters: an informative way for analysing event-related brain activity. *Journal of neuroscience methods*, 56(1):99–104, 1995.

Heleen A Slagter, Antoine Lutz, Lawrence L Greischar, Sander Nieuwenhuis, and Richard J Davidson. Theta phase synchrony and conscious target perception: impact of intensive mental training. *Journal of Cognitive Neuroscience*, 21(8):1536–1549, 2009.

Andrzej Stefański, Przemyslaw Perlikowski, and Tomasz Kapitaniak. Ragged synchronizability of coupled oscillators. *Physical Review E*, 75-1(016210):1–7, 2007.

B.L. Van de Vrande, D.H. Van Campen, and A. De Kraker. An approximate analysis of dry-friction-induced stick-slip vibrations by a smoothing procedure. *Nonlinear Dynamics*, 19(2):159–171, 1999.

Jens Wahlström. Towards a cellular automaton to simulate friction, wear, and particle emission of disc brakes. *Wear*, 313(1-2):75–82, 2014. ISSN 00431648. doi: 10.1016/j.wear.2014.02.014.

BA Wernitz and NP Hoffmann. Recurrence analysis and phase space reconstruction of irregular vibration in friction brakes: Signatures of chaos in steady sliding. *Journal of Sound and Vibration*, 331(16):3887–3896, 2012.

TECHNISCHE MECHANIK

Scientific Journal for Fundamentals and Applications of Engineering Mechanics
Wissenschaftliche Zeitschrift für Grundlagen und Anwendungen der Technischen Mechanik

Instructions for Authors

TECHNISCHE MECHANIK publishes articles in all fields of mechanics, theoretical as well as applied, including related disciplines, and in particular also articles demonstrating practical applications. The journal publishes full length papers, as well as discussions on papers which have appeared in the journal.
TECHNISCHE MECHANIK is a non-profit (open-access) journal, founded by the Otto-von-Guericke-University. It can be freely downloaded from the website.

Manuscripts have to be written with LaTeX. The most important features of the style guidelines are implemented in the files contained in **tm-article.zip** (download from http://www.ovgu.de/techmech/).

Each submitted paper runs through a standard peer review process. Please suggest three international well known reviewers for your paper when you submit it.

Please submit your paper in electronic form by email.

Hinweise für Autoren

Die Zeitschrift TECHNISCHE MECHANIK veröffentlicht Forschungsarbeiten aus dem Gesamtgebiet der Mechanik, d. h. allen Zweigen der theoretischen und angewandten Mechanik einschließlich angrenzender Fachgebiete sowie Diskussionsbeiträge zu in dieser Zeitschrift erschienenen Arbeiten. Die Zeitschrift ist ein open-access Journal das 1980 von der Otto-von-Guericke-Universität gegründet wurde. Alle Artikel können kostenfrei von unserer Webseite herunter geladen werden.

Artikel werden ausschließlich in englischer Sprache veröffentlicht.

Die Manuskripte müssen in LaTeX geschrieben werden. Die wichtigsten Stil-Richtlinien sind in den Dateien umgesetzt, die in **tm-article.zip** (bereit gestellt unter http://www.ovgu.de/techmech/) enthalten sind.

Jeder eingereichte Beitrag durchläuft einen standardmäßigen Begutachtungsprozess. Bitte schlagen Sie bei Einreichung des Artikels drei mögliche, international renommierte Gutachter vor.

Bitte reichen Sie Ihren Beitrag elektronisch per E-Mail ein.

Internetadresse / website	http://www.ovgu.de/techmech
E-Mail / email	Technische.Mechanik@ovgu.de

Address of the editor:
Institut für Mechanik
Otto-von-Guericke-Universität
Postfach 4120

D-39016 Magdeburg

Tel.: +49-391-67-52459
Sekretariat -58608
Fax: +49-391-67-12439
-12863
e-mail: Technische.Mechanik@ovgu.de
http://www.ovgu.de/techmech/

Inhalt / Contents

ISSN 0232-3869 (print)
ISSN 2199-9244 (online)